

**Development of a
Breast Tissue Diffraction Analysis System
using
Energy Dispersive X-ray Diffraction**

Sangeeta Maini Kumari Maini

University College London

2012

Submitted for the degree of Doctor of Philosophy

University College London

I, Sangeeta Maini Kumari Maini, confirm that the work presented in this thesis is my own. Further, I confirm that reference has been provided for information that has been derived from other sources.

Signature

Acknowledgement

The work that I have presented here is my Ph.D. research work, an outcome of excellent supervision, advice and support by Prof. Robert Speller and Dr. Gary Royle, my supervisors, for which I am very thankful to them. I would like to thank Prof. Andrew Todd Pokropek for his support throughout my Ph.D. I am very grateful to my colleagues, Dr. Jennifer Griffiths and Dr. Emily Cook for their inputs and help with diffraction systems. I am also thankful to my colleagues, Francisco, Sarah, Tasos, Walid, Mohammad, Caroline, Joe and the members of Radiation Physics group, UCL for their encouragement and support.

I am grateful to the British Council for awarding me the funding for my Ph.D. research through their UKIERI Doctoral Scholarship.

Big thanks go to my husband, Dr. Kadalmani Krishnan for his great support, advice, patience and co-operation. Further, I thank all my friends at Cambridge for all their support. Finally, I would like to thank my lovely parents for bringing me to this lovely world and to a level where I am proud to be a part of world's prestigious university, the UCL.

Abstract

Thesis title: Development of a breast tissue diffraction analysis system using EDXRD.

Research groups have shown that diffraction techniques could be applied for characterising materials. In particular, Energy Dispersive X-ray Diffraction (EDXRD) technique has been successfully used in characterising materials such as plastics, drugs and biological tissues. The size of breast tissues used for characterisation so far has been small, in the range of mm. In order to exploit the fullness of the EDXRD technique in characterising breast tissues and hence enable early and precise breast tumour detection, the presented research work takes the existing research work a step forward by developing a breast tissue diffraction analysis system wherein breast-sized tissue-equivalent materials have been studied for tumour detection and an optimised EDXRD system for breast tissue analysis has been presented.

For the development of this breast tissue analysis diffraction system, a ray-tracing model of the EDXRD system has been developed. The model has been used to predict diffraction spectra. These model predictions have been further used to optimize system parameters for an EDXRD system so it could be used for breast-sized samples. Materials like plastics, pharmaceutical drugs and tissues have been characterised on this optimized system. The diffraction spectra collected have been used to build a diffraction spectrum database which has been further used to generate diffraction images for detection of tumour of size as small as 0.5 cm.

Following this abstract, in the thesis, Chapter 1 introduces how X-rays interact with matter and what research groups have achieved so far in breast tissue diffraction. Ray-tracing model of EDXRD system forms Chapter 2 wherein the system parameters along with the corrections used in the model and model predictions have been presented. The characterisation of materials using optimized EDXRD system has been detailed in Chapter 3. Chapter 4 elaborates the generation of diffraction images. Chapter 5 presents the conclusions and suggests future work.

The thesis ends with a list of references.

Contents

Declaration	i
Acknowledgement	ii
Abstract	iii
Chapter 1 – Introduction	1
1.1 Breast Cancer	2
1.1.1 Understanding Breast Cancer	3
1.1.2 Anatomy of Breast	3
1.1.3 Breast Morphology	4
1.1.4 Classification of Breast Cancer.....	6
1.1.5 Stages of Breast Cancer	9
1.1.6 Recognizing Breast Cancer	9
1.1.6.1 Risk Factors	9
1.1.6.2 Women at Risk of Breast Cancer	11
1.2 Diagnosis of Breast Cancer	13
1.2.1 Mammography	16
1.2.1.1 Issues with Mammography	19
1.2.2 Magnetic Resonance Imaging (MRI)	21
1.2.3 Positron Emission Tomography (PET)	21
1.2.4 Ultrasonography	22
1.2.5 Multimodality Imaging	22
1.2.6 Other Breast Cancer Screening Methods	23
1.2.6.1 X-ray Diffraction Study using Hair	23
1.2.7 Biopsy	24

1.3	X-ray diffraction and Coherent Scatter	25
1.3.1	Attenuation of X-rays by Materials	25
1.3.2	Photon-matter Interaction	26
1.3.3	X-ray Scattering	27
1.3.4	Atomic Form Factor	29
1.3.5	Bragg's Diffraction Law	30
1.3.6	EDXRD and ADXRD Systems	32
1.4	X-ray diffraction and Biological tissues	34
1.4.1	Breast tissue characterization	34
1.4.2	Focus of the project	37
 Chapter 2 – Ray-tracing model of EDXRD System		39
2.1	Introduction	40
2.1.1	System Resolution	40
2.2	EDXRD diffraction system model based on ray tracing of photons.....	43
2.3	Development of EDXRD system model.....	46
2.4	Model inputs for spectrum prediction.....	52
2.4.1	Corrections to profile.....	55
2.4.2	Parameter set.....	56
2.5	Model Predictions.....	64
2.6	Spectral analysis.....	70
2.7	Optimisation of system geometry.....	76
2.7.1	Multivariate analysis.....	79
2.7.2	PCA analysis output – scores plot.....	80

Chapter 3 – Material Characterisation using Optimised EDXRD System	88
3.1 EDXRD system design	89
3.1.1 X-ray Source	90
3.1.2 Detector and MCA	92
3.1.3 Detector output.....	93
3.1.4 Setting up the scatter angle.....	93
3.2 Characterisation of materials – samples	94
3.2.1 Plastics and Pharmaceutical drugs.....	95
3.2.2 Breast-equivalent tissues – cuboid breast phantoms.....	96
3.2.3 Breast-equivalent tissues – triangular breast phantoms	98
3.3 Diffraction spectra.....	100
3.3.1 Spectra for plastics and pharmaceutical drugs.....	100
3.3.2 Spectra for large samples – breast-equivalent tissues.....	107
3.3.3 Spectra for tissues – triangular phantoms.....	111
3.4 Tissue diffraction spectrum database.....	112
 Chapter 4 – Breast Tissue Diffraction Analysis System	 116
4.1 Breast tissue diffraction data analysis.....	116
4.2 Representation of breast.....	121
4.3 Diffraction images for breast tissue characterization.....	122
 Chapter 5 – Conclusions and Future Work	 133
5.1 Conclusion	133
5.2 Future Work	136
 References	 137

List of figures

1.1	Anatomy of human breast	5
1.2	Mass attenuation coefficient against Photon energy plot for PMMA and Tungsten showing photon-matter interactions	27
1.3	A schematic diagram explaining Bragg's diffraction law	31
1.4	A schematic diagram of energy dispersive X-ray diffraction system	33
2.1	A schematic diagram of X-ray diffraction system	41
2.2	A schematic diagram showing EDXRD system set up	44
2.3	Schematic diagram representing the EDXRD system model development based on photon path tracing	45
2.4 a-e	Ray tracing of photons along focal spot-source collimator path	47-49
2.5	Ray tracing of photons along sample-detector collimator path	50
2.6	Block diagram representing the EDXRD system model	52
2.7	X-ray spectrum for Tungsten 70kVp	64
2.8	Photon intensity profile at the sample	65
2.9	Model prediction against measured diffraction spectra for Paracetamol	66
2.10	Model prediction against measured diffraction data for PTFE.....	67
2.11	Model prediction against measured diffraction data for PE.....	68
2.12	Model prediction against measured diffraction data for Paracetamol (input set 2).....	70
2.13 a-h	Scores plot for samples	82-86
3.1	A schematic diagram showing EDXRD system set up.....	89
3.2	X-ray beam image.....	90
3.3	X-ray beam with cross-wires.....	90

3.4	Source collimator alignment with X-ray beam.....	92
3.5	Detector collimator alignment with X-ray beam.....	92
3.6	Breast phantom preparation – Cuboid.....	97
3.7	Breast phantom – Triangular.....	98
3.8 a-d	Breast phantoms – Triangular – different tissue composition	99
3.9 a-h	Diffraction spectra of samples collected at set 1 for 60s and 400s	101-104
3.10	Diffraction spectra of samples at set 2 and set 3.....	106
3.11	Diffraction spectra of tissues at set 1 for 60s, 100s and 400s.....	108
3.12	Diffraction spectra of tissues at set 2 and set 3 for 60s, 100s and 400s	109
3.13	Profile of counts against energy (keV) for the breast phantoms with different tissue compositions for set 1.....	111
4.1	Diffraction spectra for breast phantoms and PTFE.....	117
4.2 a-c	Integrated counts over the full spectrum plotted against tissue width for breast tissues for different tissue composition: set 1, set 2 and set 3.....	118-119
4.3	Breast representation and photon path length	121
4.4 a-h	Plot of integrated counts over the full spectrum against sample width for samples for the three sets of system geometry predicted by the model set 1, set 2 and set 3.....	123-127
4.5 a	Diffraction images for tissue characterization for PMMA for sets 1,2 and 3: Sample positions 1, 2 and 3; Number of pixels 1,2 and 4.	129
4.5 b	Diffraction images for tissue characterization for Paracetamol for sets 1, 2 and 3: Sample positions 1, 2 and 3; Number of pixels 1,2 and 4.	130

List of tables

1.1	Comparison of medical imaging modalities	15
2.1	Angular resolution and momentum transfer range provided by different combinations of collimator sets.....	57-60
2.2	Angular resolution of the selected 13 collimator sets in increasing order of angular resolution values	61
2.3	Sample set used for the model	63
2.4	Spectral analysis for model predicted spectra	71
2.5	Spectral analysis for model predicted spectra for all collimator sets – number of peaks.....	73
2.6	Spectral analysis for model predicted spectra for all collimator sets – peak shift	73
2.7	Spectral analysis for model predicted spectra for all collimator sets – peak width	74
2.8	Sample set used for system optimisation	77
2.9	Parameter sets for system geometry optimisation	78
2.10	System Geometry Optimisation based on Model Predictions	87
2.11	Revised - System Geometry Optimisation based on Model Predictions	87
3.1	Sets - System Geometry Optimisation based on Model Predictions.....	89
3.2	Sample set.....	95
3.3	Tissue diffraction spectrum database.....	113-115

Chapter 1

Introduction

According to World Health Organisation (WHO) statistics [2008], cancer is one of the top ten leading causes of death across the globe (world population of 6.7 billion). It is estimated that 7.4 million people died of cancer in 2004 and, at the current rates, 83.2 million more will have died by 2015. Among women, breast cancer is the most common cause of cancer mortality, accounting for 16% of cancer deaths in adult women. Less than 1% breast cancers occur in men. At present, breast cancer, along with cervical, colorectal and possibly oral cancers, is among the few types for which early screening has been shown to reduce mortality from the disease. Evidence shows that early detection through mammography screening among women aged 50–69 years and adequate follow-up of women with a positive result could reduce mortality from breast cancer by 15–25% [Roncker et al., 2005]. In 2008, WHO conducted a survey for the percentage of world women aged 50–69 years who have been screened by mammography during 2000–2003. The data from the WHO survey indicates that screening is almost universal in Finland, Luxemburg, the Netherlands and Sweden, with 85% or more women aged 50–69 years having had mammography in the previous three years. The observation is consistent with recent findings on cancer screening in the region [Coleman et al., 2008]. By contrast, screening prevalence is extremely low in most low-income countries, being less than 5% in 2000–2003. Overall, in the

66 countries (comprising two thirds of the world's population) surveyed, only 22% of women aged 50–69 years had had a mammogram in the previous three years. The current form of X-ray mammography is only 90% sensitive. The increase in the incidence of breast cancer and the lack of breast screening facilities, demand for a 100% sensitive imaging modality, that could be used worldwide for early detection of breast cancer.

1.1 Breast Cancer: Breast cancer is the cancer that develops in the breast.

In this condition, the breast cells grow uncontrollably either at a site or invade other parts of the body in a similar fashion. It is the second most common malignancy affecting women throughout the world. Mutations in high penetrant genes such as BRCA1 and BRCA2 constitute the hereditary breast cancer. The non-hereditary forms of breast cancer are the 'sporadic' cases. This is due to mutations in a large number of low penetrant variants. Addiction to smoking or alcohol, intake of high-fat diet [Key et al., 2001] and exposure to radiation could trigger such mutations.

A strong family history, early puberty and late menopause are the major risk factors for breast cancer in women. Self and clinical breast examination, mammography and biopsy are the current techniques used to diagnose breast cancer. Breast cancer is treated by local therapy including surgery or radiation therapy and systemic therapy such as chemotherapy, biological therapy and hormone therapy. There is an emerging therapeutic approach called cancer gene therapy that corrects the defects at the gene level.

1.1.1 Understanding Breast Cancer: In human body, under normal conditions, cells divide for various reasons such as replacement of aging tissues and increased metabolic activities. However, when cell division is unchecked, it becomes uncontrollable and the result is disastrous, leading to the development of cancer. Cancer may thus be defined as an abnormal proliferation of cells, which results from uncontrolled cell division. The general mechanisms by which cells attain this unhealthy state of cancer are

- Failure in DNA-repair response and mechanism
- Transformation of a normal gene into an oncogene - gene mutation
- Loss of function of tumour suppressor gene

One of the above processes is mainly responsible for triggering cancer.

1.1.2 Anatomy of Breast: The breast refers to the upper ventral region of an animal's torso, usually that of mammals including human beings. Breasts are parts of a female mammal's body, which contain the organs that secrete milk and is used to feed infants. Human breast is an organ that, in its normal state varies in size, shape, composition and structure from person to person depending on gender, age, hormonal changes and other factors. Male breasts and female breasts in human beings develop from the same embryological tissues. Childhood breast growth is isometric and many of the structures that are seen in an adult female breast do not appear until puberty. At puberty (due to sex hormones, estrogen (mainly) and progesterone), the first stage of secondary (postnatal) breast development called thelarche occurs in females and the growth of breast becomes allometric along with growth of body. The adult male humans also have breasts (although usually less prominent, closely

resembling pre-pubertal female breasts) and are born with the main milk ducts intact. While the mammary glands that produce milk are present in the male, they normally remain undeveloped. In some situations male breast development does occur, a condition called gynecomastia. Milk production can also occur in both men and women as a rare adverse effect of some medicinal drugs such as some antipsychotic medication. Both sexes have a large concentration of blood vessels and nerves in their nipples.

1.1.3 Breast Morphology: The human breast is made up of glandular, fatty, and fibrous tissues positioned over the pectoral muscles of the chest wall. The breast is attached to the chest wall by fibrous strands called Cooper's ligaments. A layer of fatty tissue surrounds the breast glands and extends throughout the breast. The fatty tissue gives the breast a soft consistency. The glandular tissues of the breast house the lobules (milk producing glands at the ends of the lobes) and the ducts (milk passages). Toward the nipple, each duct widens to form a sac (ampulla). During lactation, the bulbs on the ends of the lobules produce milk (Figure 1.1) and once milk is produced, it is transferred through the ducts to the nipple.

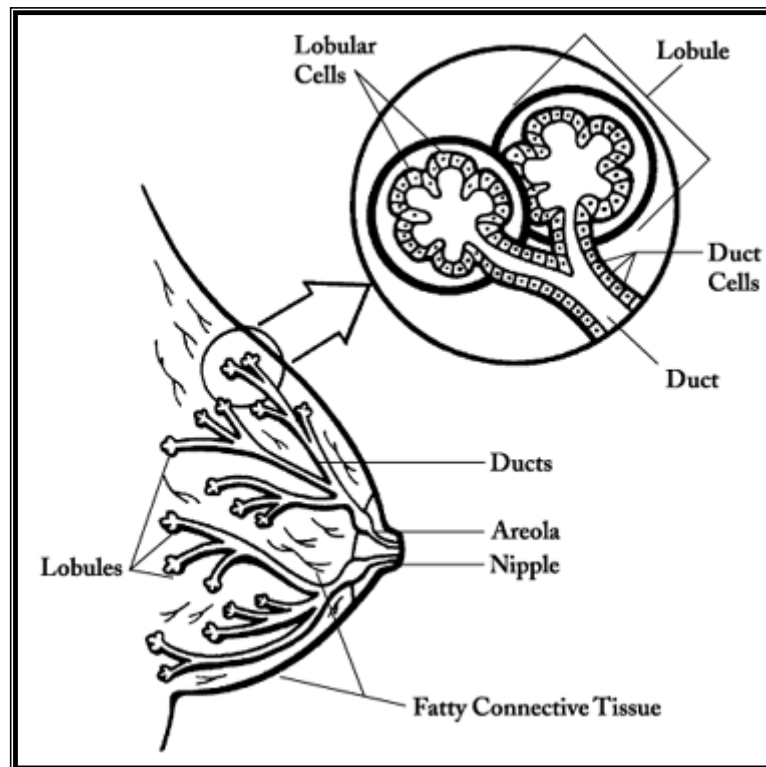


Figure 1.1: Anatomy of human breast [Source: *American Cancer Society*]

Thus the breast machinery is run by:

- Lobules, the milk glands that produce milk
- Nipple
- Areola, pink or brown pigmented region surrounding the nipple
- Ducts that transport milk from the milk glands (lobules) to the nipple
- Connective (fibrous) tissue that surrounds the lobules and ducts
- Glandular tissues
- Fat

Arteries carry pure or oxygen-rich blood from the heart to the chest wall and the breasts while veins carry the de-oxygenated blood back to the heart. The axillary artery runs from the armpit (axilla) and supplies blood to the outer

part of the breast. The internal mammary artery goes down the neck and supplies blood to interior regions of the breast.

1.1.4 Classification of Breast Cancer: Breast cancer affects both the sexes but women are at a higher risk of developing it due to the estrogen hormone, which plays a very important role in cell differentiation of breast tissue. Breast cancer can be classified in the following ways:

(1) General classification of the disease of the breast: benign, malignant or pre-cancerous. It is the malignant lesions that are unchecked growth of cells and may metastasize. The carcinoma derived from the epithelial tissues and the sarcomas (occurring in the connective stroma of the breast) are malignant. The lymphatic drainage system of the breast is thought to play a significant role in the metastasis of breast carcinoma [Carter et al., 1989]. So, mastectomy procedures always include an examination of the lymph nodes to check for any metastasizing cancers [Spratt et al., 1979]. Benign lesions also need medical attention as some of them may be precursor lesions of malignancy and also because they may clinically, pathologically or radiographically mimic carcinoma. Calcifications are small particles of Calcium Hydroxyapatite, or less commonly, crystalline structured Calcium Oxalate (weddelite) [Frappart et al., 1987] and presence of calcifications within epithelium or stroma may be a sufficient cause for radiologists to proceed with the diagnosis of the disease. Calcifications have been seen to be associated with ductal carcinoma in situ (DCIS) but are much less common in invasive tumours. Benign lesions like cysts, fibrosis, duct ectasia, adenosis have shown no increase in risk of

developing carcinoma in the future unlike pre-cancerous lesions like pseudo-infiltrative, fibroadenoma, intraduct papilloma and phyllodes tumour, that all have a statistical association with cancer. These precancerous lesions may sometimes be truly precancerous or may just remain benign lesions, resembling carcinomas. With an exception of phyllodes tumour, all precancerous lesions have shown no metastasizing features.

(2) Depending on spread of tumour: *In situ* or Invasive carcinoma. In the case of *In situ* (meaning 'in place') carcinoma, the tumor cells stay within the breast tissue and do not spread whereas invasive carcinoma results in metastasis (the spread of the tumour). When cancer cells metastasize, they either enter the blood stream or the lymphatic channel. Invasive carcinoma is the most dreadful form of carcinoma as it not only affects the primary organ, but the cancerous cells also target and travel to other vital organs of the body.

(3)

(a) Depending on site of carcinoma: Ductal or Lobular. For example for the Invasive carcinoma in the duct or lobule, it is termed as Invasive Ductal carcinoma or Invasive Lobular carcinoma respectively. Ductal carcinoma (both *In situ* and Invasive) is the common type of cancer seen among breast cancer patients.

(b) The types of known site-dependent cancers, though not so common, are

- Medullary Carcinoma - an Invasive carcinoma with distinguishing features like large cancer cells and immune cells at the border of the tumour tissue; accounting for 5% of all cancers; has a better prognosis than Invasive Lobular and Ductal cancer.
- Colloid Carcinoma - also known as Mucinous carcinoma, produced by mucous, in which cancer cells are seen floating in a lake of mucous; has a better prognosis than other types of Invasive cancer.
- Adenoid Cystic Carcinoma - a very rare type of cancer arising from salivary glands.
- Tubular Carcinoma - a type of Invasive Ductal carcinoma; distinguishing feature is the visual appearance of the cells under a microscope; cancer cells resemble tiny tubes that are well differentiated, meaning the cells are more like normal cells than poorly-defined ones; accounts for no more than 2% of all breast cancer diagnoses; cancer less likely to metastasize.
- Paget's disease of the breast (nipple) – the disease starts with scaly rashes in the nipple or areola; the red scaly cells under microscope appear as arising from intra epithelial extension of underlying Invasive or *In situ* Ductal carcinoma; cause is unknown; often confused with other skin diseases like eczema, psoriasis and dermatitis.

1.1.5 Stages of Breast Cancer: Depending on the size of the tumour, status of the lymph node and metastasis, the American Joint Committee on Cancer (AJCC) [AJCC, 2003] categorizes the breast cancer into four stages, as follows:

Stage 1 – Tumour less than 2 cm in size; with no involvement of lymph nodes.

Stage 2 – Tumour size up to 5 cm with or without the involvement of lymph nodes.

Stage 3 – Tumour cells spread to axillary lymph nodes but not to other parts.

Stage 4 – The cancer cells spread to other parts of the body.

The staging of breast cancer aids the kind of diagnosis, prognosis and treatment to be used for the cancer. Normally, prognosis of patients in stages 1 and 2 is better than that of in stage 4.

1.1.6 Recognizing Breast Cancer:

1.1.6.1 Risk Factors: Statistics show that if breast cancer in women be detected at an early stage, then the patient's life could be saved in up to 95% of the breast cancer cases. The breast cancer survival rates in England during the period 2005-2009 show that 95.8 % of women survive their disease for at least one year after the diagnosis, falling to 85.1 % surviving five years or more. Ten year survival rates have been predicted to be 77 % for patients diagnosed in 2007 [ONS, 2011; Coleman et al., 2010]. Broadly similar breast cancer survival rates have been reported for Wales, Scotland and Northern Ireland [WCISU 2010; ISD 2011; NICR 2011].

The breast cancer survival rates as reported by American Cancer Society [ACS, 2012] for patients diagnosed between 2001 and 2007 are 89 % for five years, 82 % for ten years and 77 % for fifteen years after diagnosis. The high mortality rate of breast cancer is mainly due to the delayed diagnosis (detection) of the disease. Breast cancer like any other disease has risk factors associated with it. In general, early breast cancer usually is not accompanied by any pain and when breast cancer first develops, it shows no symptoms at all. However, as the cancer grows, it causes several anatomical changes in the breast that women should watch out while self-breast examining. Following are the changes seen during development of breast cancer in women [Kelsey 1979; Key et al., 2001]:

- A palpable lump or thickening in or near the breast or in the underarm area
- Change in the shape of the breast
- Nipple discharge or tenderness
- Unexplained pain in the breast
- Nipple retraction (inverted) into the breast
- Change in the way the skin of the breast, areola, or nipple looks or feels (for example, warm, swollen, red, or scaly)

Even men show similar symptoms if they develop breast cancer. Here are some facts about male breast cancer [Reis et al., 2011]:

- Male breast cancer accounts for less than 1% of all cancer in men
- The mean age of diagnosis is from 50 - 60 years
- The risk factors which predispose men to breast cancer are radiation exposure, hyperestrogenism and Klinefelter syndrome
- History of BRCA2 mutation in the family
- Invasive ductal carcinoma is the common type of cancer
- The predominant symptom is a painless mass in the breast.
- Diagnosis is usually confirmed by Fine Needle Aspiration Cytology biopsy
- The primary standard treatment is modified radical mastectomy with axillary node dissection

1.1.6.2 Women at Risk of Breast Cancer: Age is one of the major risk factors in developing breast cancer - the risk increases with age. Women falling in any of the following categories are at an increased risk of developing breast cancer [Kelsey 1979; Smith-Warner et al., 1998; Key et al., 2001]:

- A strong family history of breast cancer at a young age
- Early puberty
- Late menopause
- Child bearing after the age of 30 years
- Nulliparous women
- History of benign breast disease (atypical hyperplasia)
- Exposure to radiation
- High fat diet
- Treatment for hormone replacement therapy

- Obesity (especially after menopause)
- Alcohol intake
- Increased density of breast tissue

However, it is worth noting that women who do have one or more of these risk factors do not always develop breast cancer and also that many women who do develop breast cancer do not have any risk factors. The sex hormone level (estrogen) has a key role in developing breast cancer as it is this hormone that is responsible for the major risk factors, early puberty or late menopause. Sadly, the role of estrogens in breast cancer risk during pre-menopausal periods is largely unknown. However, the risk can be gauged by the number of estrogen receptors, which are thought to play an important role in breast cancer - an excessive increase in the number of receptors can cause uncontrolled cell proliferation. Hence, the prognosis for breast cancer cases where estrogen receptors are implicated is better than those with normal estrogen receptor count and the latter could be due to other reasons. The following are other factors that aid in the breast cancer risk assessment and are usually considered while studying a case:

- the number of affected relatives
- age at diagnosis
- the degree of closeness between relatives of family members
- Presence of bilateral or multi-focal breast cancer
- Presence of other cancers such as ovarian cancer
- Involvement of male breast cancer

Research groups [Friedenreich, 2001, Gunnell et al., 2001] have confirmed that taller women have a slightly increased risk of being diagnosed with breast cancer. So, height may be associated with breast cancer risk in post-menopausal women. The research study has shown that risk of breast cancer increased by 7% for every 5 cm increase in height in post-menopausal women. Scientists at the National Cancer Institute, USA [Fox 2000] have developed a breast cancer risk assessment tool to estimate a woman's risk of developing breast cancer over a period of five years and over the life time. Groups have also developed models to assess the risk associated with breast cancer - the Claus model discusses the risk level based on family history of breast cancer [Claus et al., 1994] while the Gail model focuses on the non-genetic risk factors with limited information on family history [Gail et al., 1989]. A statistical model called BRCAPRO is also available, which is based on personal and family history characteristics and identifies the presence of any germline mutation (BRCA1 or BRCA2).

1.2 Diagnosis of Breast Cancer: The foremost and most recommended way of detection of breast tumour is by physical touch i.e. by breast self-examination (BSE) on the grounds that anatomical changes in the breast that could become malignant could be felt by women. According to Merck et al. [2003], more than 80% of breast cancer cases are discovered when the woman feels a lump in her breast. A clinical breast examination (CBE) is commonly practiced either as a part of routine examination or on concerns from BSE. CBE is a physical examination of the breast done by a health professional. Any changes in the breast or development of lump in the breast during the

examination can give, to some extent, clues about the size of the tumour, its texture, and details such as whether it is likely to metastasize. CBE is used along with other diagnostic measures to check women for breast cancer. CBE also helps identify other breast problems. However, there is little scientific evidence on effectiveness of BSE and CBE ways of examination in reducing the number of deaths due to breast cancer [George, 2000]. Hence, screening for breast cancer demanded for an effective way of examining the breasts and also further diagnosing the breast cancer. Imaging of breasts, in conjunction with BSE and CBE, and followed by a biopsy, has proved to be a great success in reducing breast cancer mortality rate [Varghese et al., 2006; Hackshaw et al., 2003].

The period between late 19th and the 20th century witnessed the greatest breakthrough of science and technology when development of imaging techniques, based on radiation, radionuclide, magnetic resonance and ultrasonic began. This gave a boost to the field of medical imaging and since Roentgen's first X-ray scan of a hand more than a century ago, the field has progressed immensely. Today, medical imaging modalities like mammography, computed tomography (CT), positron emission tomography (PET), magnetic resonance imaging (MRI), ultrasonography, single photon emission computed tomography (SPECT) and scintimammography are used in hospitals and medical centres. An imaging modality is either used as a preliminary technique for detection of breast cancer or as an adjunctive technique for further diagnosis. The use of an imaging modality depends on the level of diagnostically useful image (information) it produces (provides).

An ideal imaging system to detect breast cancer *in vivo* i.e. live in a patient's breast, would have a 100 % sensitivity (should be able to detect cancers all of the time) and a 100 % specificity (should be able to reject all the patients who do not have a cancer).

Modality	Sensitivity (%)	Specificity (%)	Current Status
<i>X-ray mammography</i> [Banks et. al., 2004]	86.6	96.8	Used in regular breast screening
<i>Scintimammography</i> [Libermann, 2003]	85.2	86.6	Some clinical trials in progress
<i>Magnetic Resonance Imaging (MRI)</i> [Hendrick, 2005]	> 90	37 – 90	Adjuvant imaging due to cost
<i>Ultrasonography</i> [Houssami, 2002]	81.7	88	Adjuvant imaging for suspicious lesions in young women
	Women attending symptomatic clinic		
<i>Infra-red (IR)/Optical Spectroscopy</i> [Cheng et. al., 2003]	92	67	Still at early stage
	X-ray mammographically positive patients		
<i>Electrical Impedance Tomography (EIT)</i> [Malich et. al., 2003]	80.5	64.7	Still at early stage
	Ultrasound & X-ray previously shown suspicious findings		

Table 1.1: Comparison of medical imaging modalities [Source: Griffiths, 2005]

A patient's discomfort, availability of the system and the radiation dose received by the patient are other factors that affect the choice of the imaging system. Table 1.1 compares the percentage of sensitivity and specificity that has been achieved by the imaging modalities that are in use today, along with the current status of each of these with regards to the level of diagnostically useful images they produce.

Among the modalities listed, mammography is essentially the widely used imaging modality for breast screening in combination with self-breast examination and clinical breast examination. This was not true until 1966, when Compagne Générale de Radiologie (CGR, France) developed the first mammography unit in collaboration with French radiologist Charles Gros. The unit featured a molybdenum anode with a 0.7 mm focal spot. Since then, several system manufacturers have developed dedicated mammography units which are widespread available. Although, other modalities are also able to produce diagnostically useful images, they have a better use as adjunct imaging modalities. In future, these adjunct modalities may get to the front, in conjunction with mammography or may become more common if they can provide better diagnostically useful contrast in the images of soft tissues. The issues associated with the listed imaging modalities include the resolution and contrast of the image while modalities involving use of radiation have issues related to dose too. Research and development is ongoing to improve these techniques further. A brief description of state-of-the-art imaging modalities follows here:

1.2.1 Mammography: Mammography technique involves use of ionizing radiation, X-rays and is therefore also known by the name, X-ray mammography. The technique, mammography images the breast with an X-ray (usually Molybdenum target, characteristic photons 17.4 keV and 19.6 keV, and Molybdenum filter) transmission to detect mass of tumour or calcifications in the breast. The technique is performed by compressing (in the range 10 to 30 Newtons) the breast [Poulos et al., 2003] firmly between a

plastic plate and an X-ray cassette containing the X-ray film (traditionally). Films are taken in two projections (Medio-Lateral Oblique, MLO - looking at the breast from the opposite shoulder and Cranio-Caudal, CC - looking vertically down on the breast) so as to eliminate any superposition of normal breast structures. The technique produces mammograms, which are images of the breast produced when X-rays passing through the breast, get attenuated differently by the normal and carcinoma tissues of the breast. The normal and neo-plastic (carcinoma) tissues appear as black and grey areas, respectively, on the mammograms, which are studied by radiologist for further diagnosis. Mammography can detect cancer at an early and curable stage. It can even identify breast cancers that are too small to be palpated by physical examination and calcifications in the breast. It can also detect the presence of lumps if it is localised (Ductal Carcinoma *In situ*). Observational studies have found that the positive predictive value of mammography increases with age and is highest among older women and among women with a family history of breast cancer. Currently, X-ray mammography is used as the preliminary examination, after SBE and CBE, under the national asymptomatic breast screening programmes of most of the developed nations and is gaining rapid popularity among other nations too.

The state-of-the-art X-ray mammography is witnessing a transition to digital from screen-film mammography and will continue to do so in the years to come. Digital mammography uses a single or multiple detector assembly to capture an electronic image of the X-rays transmitted through the breast. The advantage that digital mammography facilitates is that the images captured can

be displayed, stored and communicated electronically. Using standard software processing, the images can be manipulated for contrast-enhancement or for highlighting other important features. Clinical trials comparing digital mammography with screen-film mammography in a screening population demonstrate equivalency for cancer detection [Lewin et al., 2002, Pisano et al., 2005, Skaane et al., 2007], and digital mammography performed significantly better for pre- and peri-menopausal women younger than 50 years with dense breasts [Pisano et al., 2008]. Also, improvements in detector technology and transition to higher kV_p techniques will help reduce the radiation dose. The recent advances and ongoing research also indicate towards use of a large-area photon counting energy-resolving detector.

Digital mammography with stereoscopic display system has provided for significant improvement in detection of masses and microcalcification. In stereoscopic digital mammography (SDM), two projection images spaced a few degrees apart are recorded with a digital mammography system [Getty et al., 2007, 2008]. A depth discrimination of 0.2 mm can be achieved using projection pair images acquired at an angular separation of ± 6 degrees and with geometric magnification. A clinical screening trial with high-risk women suggest that SDM reduced false positive lesion detections by 46% and significantly increased true positive lesion detections by 23% compared to digital mammography and hence showed an improved sensitivity and specificity [Getty et al., 2008].

1.2.1.1 Issues with Mammography: The X-ray Mammography has shown to reduce mortality due to breast cancer and is therefore the most widely used breast imaging modality [Shapiro et al., 1971; Tabar et al., 2001]. Despite this fact, X-ray mammography has certain disadvantages and issues associated with it and can be summarised as follows:

- The physical compression of breast does offer advantages in terms of adequate tissue separation, X-ray scatter and radiation dose for producing good quality mammograms but places a time constraint to obtain the image, which is of high significance when a line-scan digital imaging is used.
- Other disadvantage arises from use of anti-scatter grids as they suffer from incomplete suppression of scattered radiation, reduction in primary radiation reaching the detector, and artifacts [Chakraborty, 1999].
- X-ray mammography, in general, reports 10% of false-negative (or false-positive) cases [Huynh et al., 1998]. The normal breast tissues appear black/grey on a mammogram while a tumour appears as a white spot or patch. A false-positive reporting occurs when radiologists interpret normal areas on mammograms as tumours and the reverse happens in the case of false-negativities. This happens not due to radiologists' inefficiency in studying and inferring from mammograms, although for individuals this might be so albeit reduced by high standards of training, but perhaps more due to the breast imaging results that appear on mammograms. Following are the factors that lead to false reports:

- Calcifications, that are calcium deposits in breast, too appear as white spots on a mammogram. This makes it difficult for radiologists to assess (based on the shape, size and pattern) whether the white spots are calcifications or tumour. Usually, micro-calcifications are not due to cancer. However, in a small number of cases, a group of micro-calcifications seen in one area (a cluster), may be a sign of pre-cancerous changes in the breast, or of an early breast cancer [Leborgne, 1951; Thomas et al., 1993].
- Other observation on mammogram that counts towards the false-screening is the breast density. The overlapping of (or masking by) dense breast tissues could obscure tumours on a mammogram. This has usually been seen among younger women. Literature [Buist et al., 2006] has shown link between breast density and the period about menstruation. However, not much has been done in this direction and high breast density is still one of the challenges in X-ray mammography. A strong association has been established [Norman et al., 2007] between extensive mammographic density and risk of breast cancer (increase by a factor of 17 up to a period of 12 months after screening examination). It has also been shown that annual screening in women with high breast density are not likely to increase the rate of detection of cancers and hence, attention has been drawn towards developing and evaluating alternative imaging techniques for women with dense breasts.

1.2.2 Magnetic Resonance Imaging (MRI): MRI is a non-invasive imaging technique which uses a strong magnet and radiofrequency waves to produce images of internal organs. The clinical role of MRI [Warner et al., 2008] in breast cancer imaging includes:

- Determining the true edges of the tumour prior to surgery
- To differentiate a palpable mass from breast scar or a dense tissue
- Assessing palpable masses following surgery or radiation therapy
- Detecting mammographically and sonographically occult breast cancer in patients with axillary nodal metastasis
- Assessing recurrence in silicone breast implants

Though MRI has potential applications, it is not routinely used in breast cancer due to the high expense involved in it and the noise associated with it but is used as an adjunct to mammography and ultrasonography.

1.2.3 Positron Emission Tomography (PET): PET technique involves the use of radioactive material in the diagnosis of breast cancer. In this technique, the patient is injected with a radioactive substance (like glucose-8-fluorodeoxyglucose-FDG), a compound taken up by metabolically active tissues [Adler et al., 1993]. As cancer cells are more metabolically active than normal tissues, the tumour tissue takes up relatively more radiolabelled substance. The patient is placed in a scanner to detect the radiation. This test may be particularly useful to determine the spread of cancer to other sites in the body. The main advantage of PET is that it can diagnose diseases even before the structural changes are visible. Since, it utilizes isotopes of basic biological elements like Carbon, Oxygen, and

Nitrogen it reveals the disease status at a more cellular level than other types of imaging techniques.

1.2.4 Ultrasonography: The technique of ultrasonography works on use of ultrasonics i.e. high frequency acoustic waves (for example 2 – 6 MHz). Imaging is done by directing ultrasonic waves into an object to detect the reflections that occur at interfaces between materials with differing acoustic properties within the object. Ultrasonography offers a spatial resolution of the order of millimetres in parallel to some depth information. In recent years, breast ultrasonography has become an essential modality in breast imaging. It plays an important role in distinguishing cysts from solid masses, evaluation of palpable masses, and for needle core biopsy of masses [Burns et al., 1982]. Kolb et al., [2002] have shown in their publication an improved sensitivity (97% against 74%) when adjunctively used with mammography compared to physical examination with mammography. An improvement in sensitivity for dense breasts with ultrasound compared to mammography was also shown by the same group.

1.2.5 Multimodality Imaging: As seen in the sections above, there is no single imaging modality that can provide information on all aspects of structure and function of the underlying tissues and each imaging modality is characterized by differing spatial and temporal resolutions and a different sensitivity. An obvious approach is to interrogate a subject using multiple imaging modalities [Cherry et al., 2006]. Combinations of imaging modalities integrate the strengths of two modalities and at the same time eliminate one or

more weaknesses of an individual modality. Recent developments have been seen in the semi-automated scanning ultrasound device integrated with a digital breast tomosynthesis (DBT) system and in an ultrasound computed tomography system [Karellas et al., 2008]. Pramanik et al. [2008] have designed and evaluated a novel breast cancer detection system combining both thermoacoustic (TA) and photoacoustic (PA) tomography. PET/CT and SPECT/CT have become the most widely adopted multimodality systems [Bockisch et al., 2009]. In the years to come, there is a possibility of using ultrasound as an adjunct to mammography for heterogeneous breasts. The multimodality imaging thus, offers the prospect of improved diagnostics.

1.2.6 Other Breast Cancer Screening Methods: Other screening methods of breast cancer include: X-ray diffraction study of hair, Electrical Impedance Tomography, Infra-red/Optical spectroscopy, Immunoassay (to detect tumour markers and other antibodies), Ductal lavage and Flow cytometry (to detect cancer cell division rate).

1.2.6.1 X-ray Diffraction Study using Hair: James et al, Birki et al and more recently, Corino et al [James et al., 1999, Birki et al., 1999, Corino et al., 2008] have shown that X-ray diffraction patterns (with synchrotron radiation) of hair of breast cancer patients are different, with respect to the intermolecular structure of hair, from that of a healthy person. The findings of James remained in controversy as groups independent of James could not replicate the outcome [Evans et al., 2001; Sutton et al., 2003; Rogers et al., 2006; James, 2006]. Corino et al. [2008] have pointed out reasons (for

instance, handling and mounting the hairs) that could have affected the reproducibility of James findings and have provided a methodology that would help other groups replicate James' work or obtain diffraction patterns. Corino et al [2007] showed the appearance of a ring with a molecular spacing of around 4.76 nm and claimed X-ray diffraction of hair to have the potential to provide a non-invasive test for the presence of breast cancer. However, the sensitivity and specificity of this method are yet to be determined.

1.2.7 Biopsy: Biopsy is a medical procedure in which a small amount of tissue or fluid is removed from the breast tissue and examined for its pathology. Using the biopsy techniques, a pathologist can determine whether the tumour is

- Benign or Malignant
- Ductal or Lobular
- Invasive or Non-invasive

Biopsy could be a Fine Needle Aspiration Cytology (FNAC) type in which a thin needle is used to draw fluid or cells from the breast tissue and examined for the presence of cysts or tumour, further confirmed by ultrasound. A Needle biopsy involves use of a needle for removal of a tissue sample from the suspected region that perhaps may not have been detected even in a mammogram. Apart from FNAC and Needle biopsy there could be a surgical biopsy depending on whether a sample of the lump is excised for studying its pathology (Incisional Biopsy) or the entire lump along with a small bit of

normal tissue is removed to study the spread of tumour (Excisional Biopsy). Recently a new technique has been developed called the Sentinel Lymph Node Biopsy. The sentinel node is the first lymph node where the lymphatic vessels drain and most likely to contain cancer cells. The technique involves use of a small amount of dye (for example Technetium) that is injected into the area around the tumour [Veronesi et al., 1997]. Lymphatic vessels carry these substances into the sentinel node. The dye can then be detected using scintillation counter.

1.3 X-ray diffraction and Coherent Scatter:

1.3.1 Attenuation of X-rays by Materials: When an X-ray beam is radiated on a material, its intensity decreases with the distance it travels through the material. For monochromatic radiation in a good geometry (narrow beam) arrangement, the fractional decrease in intensity I of the X-ray beam is directly proportional to the distance traversed by the beam (x) through the material.

$$-\frac{dI}{I} = \mu dx \quad 1.1$$

where μ is the linear attenuation coefficient for a given photon energy is dependent on the properties of materials (for e.g. density ρ) and the wavelength of X-rays.

Simplifying equation 1.1 yields,

$$I_x = I_0 \exp(-\mu x) \quad 1.2$$

where I_0 is the intensity of incident radiation and I_x is the intensity of radiation after passage through the material. The linear attenuation coefficient, μ has units of $(\text{length})^{-1}$ (for e.g. cm^{-1}). Since, μ depends on the density of the material, the mass attenuation coefficients, μ/ρ , are usually expressed in units of cm^2/g and the value of μ/ρ are obtained from measured values of I_0 , I and x .

1.3.2 Photon-matter Interaction: The fundamental unit of an electromagnetic radiation, the photon, interacts with matter by several of four major processes: Coherent scattering, Incoherent scattering, Photoelectric effect or Pair production. The probability of each interaction is determined by a cross section which depends on the energy of its incident photons, density and atomic number of the material. Figure 1.2 shows photon-matter interaction in terms of attenuation coefficient values with increase in photon energy. Concentrating on the diagnostic energy region of 10-160 keV will reveal dominance by three main interactions: elastic scattering (Rayleigh), inelastic scattering (Compton) and photoelectric effect.

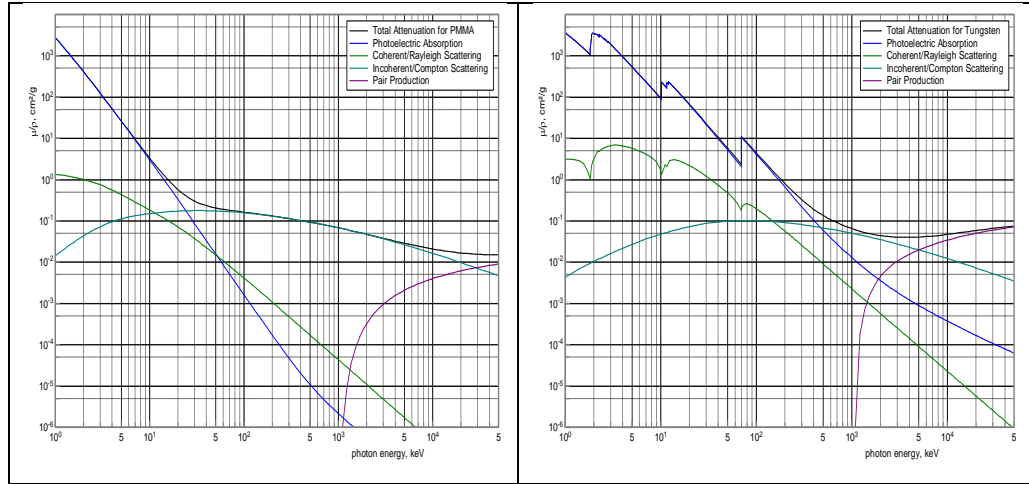


Figure 1.2: Mass attenuation coefficient against Photon energy plot for PMMA and Tungsten showing photon-matter interactions [Source: Boone et al., 1996; software *XMuDat*]

Most of the X-rays undergo photoelectric interaction and deposit all of their energy in the material. In low atomic number materials, a significant amount of scatter is observed at lower energies. The following section is a closer look at X-ray scattering.

1.3.3 X-ray Scattering: When X-rays interact with atoms in a material, two kinds of scattering processes can take place. Coherent scattering occurs when incident photons interact with tightly bound electrons of the atom so as to set them into oscillations to radiate X-rays of wavelength that is the same as that of incident photons. This type of scattering is also known as Rayleigh scattering. Incoherent scattering, alternatively referred to as Compton effect, is observed when the incident beam is partially scattered by the loosely bound electrons of the atom, increasing its wavelength during the interaction. In coherent scattering, as the incident photon interacts with the electrons in the atom, electrons are set to vibrate in resonance with E , the electric vector component of X-rays (polarized ray). This renders electron the frequency of

the photon. The electron being a charged particle and in a vibrating state, by deriving some energy from the incident photon, radiates it at same wavelength as the incident photon [Smith, 2000]. This has been explained by the classical Thomson equation, for which the scattering cross section is given by:

$$\frac{d\sigma_T}{d\Omega} = \frac{r_e^2}{2} * (1 + \cos^2 \theta) \quad 1.3$$

where $\frac{d\sigma_T}{d\Omega}$ is the differential Thomson cross section per electron for elastic scattering of an unpolarized beam, θ is the scatter angle, r_e is the classical electron radius. This equation is an approximation that ignores both magnetic force and relativistic effects. Interference effects can be observed when more than one electron is excited by electromagnetic radiation. So, the differential scatter cross-section for atoms is generally written as the product of Thomson (free electron) cross section and the form factor. This expression describes influence of inter-electron coherence on scattering from a single electron.

$$\frac{d\sigma_{coh}}{d\Omega} = \frac{d\sigma_T}{d\Omega} (\theta) F^2(X, Z) \quad 1.4$$

where $F^2(\chi, Z)$ is the atomic form factor, that depends on the momentum transfer, χ , and the atomic number Z . The form factor is the Fourier transform of the electron charge distribution of the scatterer [Hukins, 1983]. Several model-based indirect methods are available for knowing the charge distribution from a diffraction pattern as measurements always give the intensity of the scatter wave. The momentum transferred to the photon that causes its deflection by an angle is defined as $\chi = (1/\lambda) * \sin(\theta/2)$. The

momentum transfer takes into account the variations in both the photon energy and the scatter angle.

1.3.4 Atomic Form Factor: The atomic form factor, F is the spatial electron distribution in the atom from which the photon can be scattered without any momentum transfer. F is defined as the ratio of the amplitude of waves scattered by the atom to that of a free classically scattering electron (IAM, independent atom model). The atomic number Z replaces F in cases in which an atom is considered to be at a point by an atom that has a diameter that is comparable with the wavelength of the photons. So, secondary waves from different electrons in space have a phase difference that causes in certain directions addition or cancellation of radiation. F can be expressed as follows, in terms of momentum transfer:

$$F(\chi, Z) = \int_0^{\infty} \frac{n_0(r) \sin(4\pi r \sin(\frac{\theta}{2})/\lambda)}{4\pi r \sin(\frac{\theta}{2})/\lambda} dr \quad 1.5$$

where $n_0(r)$ is the density of electrons between radius r and $r+dr$. Hubbell and Overbo [1979] calculated and tabulated values of F , based on Hartree-Fock relativistic K-shell wave function. It includes F values for a range of tissues and tissue-equivalent materials. Coherent scatter from a compound or a mixture can be expressed as:

$$\frac{d\sigma_{\text{coh}}}{d\Omega} = \frac{d\sigma_T}{d\Omega}(\theta) F_m^2(\chi, Z) \quad 1.6$$

where $F_m(\chi, Z)$ is the molecular form factor which approaches the free atom form factor at higher photon energies (higher values of momentum transfer).

In the case of incoherent scattering, scattering of a photon takes place by interaction with a free or a loosely bound electron. The photon transfers some of its energy to the electron and changes its direction. This type of scattering is depending per electron on the atomic number of the material. The differential cross section then depends on the mass density and decreases with increasing energy and is described in terms of the Klein Nishina formula as $\frac{d\sigma_{com}}{d\Omega} = \frac{d\sigma_{KN}}{d\Omega} S_m(\chi, Z)$ where $\frac{d\sigma_{KN}}{d\Omega}$ is the Klein Nishina differential cross-section.

Thus, the expression for the incoherent differential cross-section is given by:

$$\frac{d\sigma_{com}}{d\Omega} = r_e^2 [1 + k(1 - \cos \theta)]^{-2} \left[1 + \cos^2 \theta + \left[\frac{k^2(1 - \cos \theta)^2}{1 + k(1 - \cos \theta)} \right] \right] S(\chi, Z) \quad 1.7$$

where k is the photon energy in electron rest-mass energy units [$k=E(\text{keV})/511$] and θ is the scatter angle, r_e is classical electron radius, Z is the atomic number of the material. $S(\chi, Z)$ is the incoherent structure factor that corrects for the electron binding energies.

1.3.5 Bragg's Diffraction Law: Materials with regular structures, on interaction with electromagnetic waves exhibit the phenomenon of diffraction. The waves interact coherently with the regular structures whose repeat distance is of the order of the wavelength of waves and form interference patterns called diffraction. For example, light is diffracted by a grating having

line spacing of the order of a few thousand angstroms in the range of wavelength of light. The X-rays have a wavelength of order of a few angstroms like the inter-atomic distances in crystalline solids, indicating that X-rays diffract from minerals. In the year 1912, Prof. W.L. Bragg formulated the basis of X-ray diffraction – the Bragg’s law (Figure 1.3).

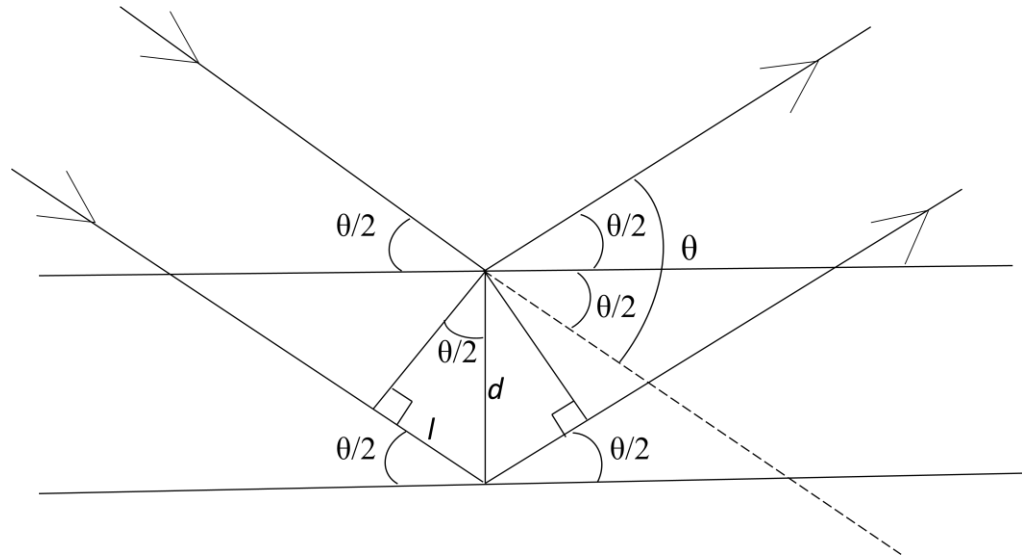


Figure 1.3: A schematic diagram explaining Bragg’s diffraction law

According to the law, under certain geometric conditions, X-rays scattered from crystalline materials can constructively interfere to produce a diffracted beam. Bragg related the inter-atomic spacing in the crystalline material, the wavelength of incident radiation and angle of diffraction by the expression, given by:

$$n \lambda = 2d \sin \left(\frac{\theta}{2} \right) \quad 1.8$$

where n is an integer, d is the distance between atomic planes in a mineral (inter-atomic spacing or d -spacing), measured in angstrom units (\AA), θ is the

angle of diffraction, measured in degrees and λ is the wavelength of the incident X-radiation, measured in angstrom units (\AA).

The diffraction caused by a material on interaction with X-rays can be measured using a diffractometer. This information can then be used to analyze the structure of material. An X-ray diffractometer has the following components: a source of radiation, a monochromator to filter out the unwanted wavelengths, slits to adjust the shape of the beam, a sample and a detector. A Goniometer could be used in combination with a diffractometer to change the scatter angle by adjusting the positions of sample and the detector. Crystallographers use X-ray diffractometer to elucidate structures of several unknown crystals. The diffraction peaks obtained on measurement are interpreted depending on their intensities and positions, with regards to axis labelled 2θ . The intensity of interference from a given set of planes depends upon factors like atomic form factor and the crystal structure.

1.3.6 EDXRD and ADXRD Systems: Energy-dispersive X-ray diffraction (EDXRD) is a X-ray diffraction technique based on coherent scattering of X-ray photons. It has been employed for characterization of materials based on their diffraction profiles. The technique uses a polychromatic source of X-ray, e.g. Tungsten (W) anode (with a suitable filter, Aluminium, for example) and a high resolution energy-resolving detector like the High Purity Germanium (HPGe) that could produce high quality scatter spectra of the sample; the detector is placed at an angle (scatter angle) to the incident beam line (Figure 1.4). This kind of arrangement allows interference

of waves only at certain wavelengths satisfying Bragg diffraction. The choice of scatter angle could be made by a prior knowledge of desired momentum transfer values. Momentum transfer (χ) is a function of energy of the photons E (keV) and the scatter angle θ (degrees) and typically has units, nm^{-1} .

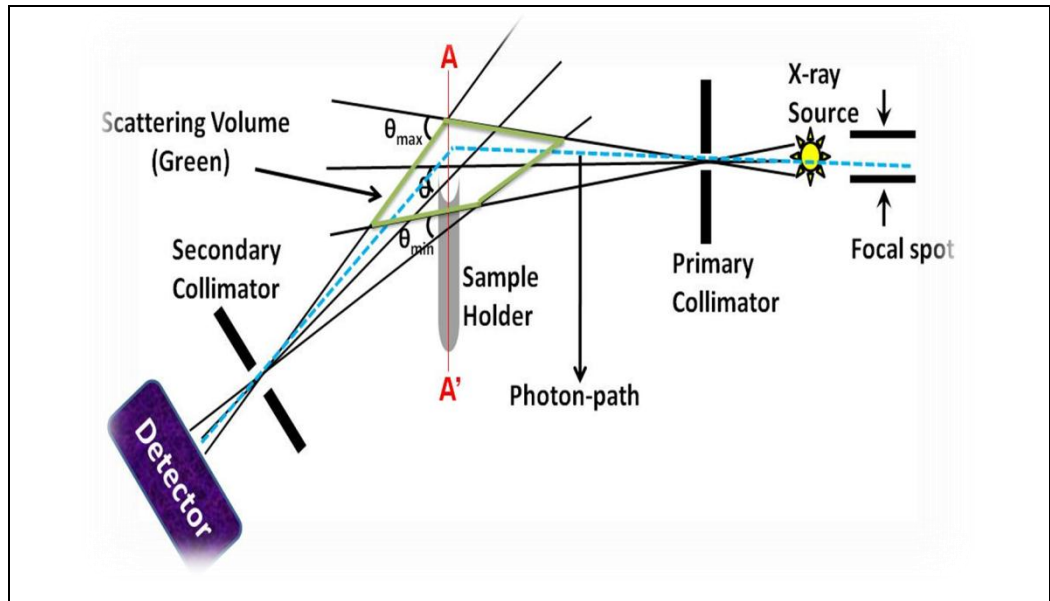


Figure 1.4: A schematic diagram of energy dispersive X-ray diffraction system

The momentum transfer relates the scatter angle to the photon energy by the expression:

$$\chi = \frac{E}{hc} \sin\left(\frac{\theta}{2}\right) \quad 1.9$$

h =Planck's constant, c =velocity of light.

In terms of photon energy, $E = hc/\lambda = hc/(2d*\sin(\theta/2))$. At a fixed scatter angle (EDXRD systems), one can observe a proportionality relation between E and $1/d$ while in the ADXRD systems, as λ is held constant, $\sin(\theta/2)$ becomes

proportional to $1/d$. Thus a plot of scattered intensity against momentum transfer shows peaks that can be related to inter-atomic spacing of the material. Expression of radiation intensity in terms of momentum transfer units enables comparison of diffraction data recorded on any X-ray diffraction system.

As opposed to EDXRD, Angular dispersive X-ray diffraction (ADXRD) is another X-ray diffraction technique that measures scattering of photons at different angles by use of an X-ray diffractometer. In this case, a monochromatic source of X-ray is used in combination with usually CZT detectors, CCD or pixellated detectors.

1.4 X-ray diffraction and Biological tissues: Scientists have shown that biological tissues exhibit X-ray diffraction properties and this feature could be used as their signature for identification. Theodorakou et al., [2008] gives a detailed review on human soft tissue analysis using X-rays or gamma rays. Several tissue types have been analyzed like bone [Royle and Speller, 1995], hair [James et al., 1999], lyophilised blood [Desouky et al., 2001], brain and prostate [Lazarev et al., 2000]. However, there is a good amount of published work that emphasizes on the breast tissue and techniques are being developed for establishing a clear distinction between a normal breast tissue and a tumour.

1.4.1 Breast tissue characterization: Johns et al., [1983] investigated that the coherently scattered photons diverge sufficiently from the primary ray to degrade the diagnostic radiological image contrast and account for a

significant fraction of the total scattering energy fluence at the image receptor. In the last two decades, several groups have shown that X-ray scattering could offer to improve the image contrast and be a potential technique for characterisation of tissues (mainly, breast). Evans et al. [1991], in the early 1990s carried out angular dispersive X-ray diffraction measurements on 19 breast samples and concluded that the diffraction techniques showed a higher sensitivity to changes in breast tissue type than direct transmission methods. Later, Kidane et al. [1999] measured diffraction spectra from 100 tissue samples (out of which 30 were carcinoma) and inferred that both the shape and peak height of the spectra played a key role in the differentiation of tissue types, with the peak due scattered radiation in adipose tissue appearing at a momentum transfer value of 1.1 nm^{-1} and the peak due to carcinoma appearing at a momentum transfer value of 1.6 nm^{-1} . Similar results were produced by Poletti et al. [2002]. X-ray diffraction signatures of breast tissues at momentum transfer values less than 1.0 nm^{-1} were observed by Fernández et al., [2002] and Lewis et al., [2000]. The authors associated change in structure of collagen with the differences seen in the spectra recorded for healthy and cancerous breast tissues. This difference in tissue types was further studied by Geraki et al., [2004] for quantification of the amounts of adipose and fibrous tissues present in breast tissue samples. Around the same time, Harris et al., [2003] employed X-ray diffraction to create planar images of breast tissue using diffracted X-rays at 1.1 , 1.4 and 1.6 nm^{-1} and showed that the diffraction images produced had a higher contrast (but lower spatial resolution) than the transmission images.

The diffraction data can also be used to form a tomographic image. Harding et al. [1990, 1999, 2009] developed a macro-scale diffraction computed tomography (CT) system and produced images of water-bath phantom (50 mm diameter) containing various plastic inserts. Since then the National Synchrotron Light Laboratory in Brazil [Barroso et al., 2001] developed a micro-computed tomography (microCT) system for imaging small plastics. The system was updated by Castro et al., [2004, 2005] for imaging fixed breast tissue samples.

Research work on diffraction enhanced imaging by Bravin et al., [2002], Hasniah et al., [2002], Griffiths et al., [2004] and Round et al., [2005] and more recently, by Chenglin et al. [2007], Changizi et al., [2008], Fernández et al., [2008] and Sidhu et al., [2008] prove the potential that the diffraction techniques have with respect to improving the weaknesses of mammography.

Research work by Griffiths et al., [2008] has achieved (with small breast tissue samples at mammographic energy) an increased image contrast between cancerous and normal breast tissues using microCT as compared to transmission measurements. This work on diffraction employed angular dispersive X-ray diffraction methods but an application of these systems in a hospital would need to make use of energy dispersive X-ray diffraction (EDXRD). Pani et al., [2006] and Griffiths et al., [2007] used a Tungsten target X-ray tube and an energy-resolving detector and showed that EDXRD techniques have great potential for producing diffraction microCT images of small breast tissue samples.

1.4.2 Focus of the project: Research groups have shown that diffraction techniques could be applied for characterising materials. In particular, Energy Dispersive X-ray Diffraction (EDXRD) technique has been successfully used in characterising materials such as plastics, drugs and biological tissues. In particular, for the breast tissues, the tissue size used for characterisation so far has been small, in the range of millimetres. In order to exploit the fullness of the EDXRD technique in characterising breast tissues and hence enable early and precise breast tumour detection, the presented research work aims at taking the existing research work a step forward by developing a breast tissue diffraction analysis system wherein breast-sized tissue equivalent materials have been studied for tumour detection and an optimised EDXRD system for breast tissue analysis has been presented.

In order to bring the EDXRD technique to clinical use one needs to test the technique for breast sized samples. Therefore, this project aims at developing a breast tissue diffraction analysis system, based on coherent scattering of X-rays that could distinguish cancerous and non-cancerous states of breast tissue, with high sensitivity and specificity, and low radiation dose. Such a scattering based detector could be used in combination with the detectors of current imaging units. The images recorded by both the detectors could then be processed for better contrast and other specific features desired on, for instance, a mammogram, thereby, reducing the false reporting about breast cancer.

The breast tissue analysis system based on EDXRD technique has been developed as follows:

- 1) For the development of this breast tissue analysis diffraction system, a ray-tracing model of the EDXRD system has been built. The model has been used to predict diffraction spectra. These model predictions have been further analysed using statistical technique to obtain optimum parameters for an EDXRD system that could be used for large, breast-sized, samples.
- 2) On this 'optimised' EDXRD system, diffraction measurements have been made to characterise materials like plastics as tumour substitutes, pharmaceutical drugs.
- 3) Breast phantoms have been prepared to mimic breast tissues and tumour.
- 4) Diffraction measurements have also been made using these breast phantoms. Different breast thicknesses have been studied along with tumour detection.
- 5) The collected diffraction data have been analysed to produce diffraction images representing breast tissues and tumour. This could provide an additional source of information for breast imaging in terms of tissue composition and tumour detection.

Chapter 2

Ray-tracing model of EDXRD System

The presented research work investigates the potential for X-ray diffraction techniques in breast imaging. Research groups [Kidane 1999, Poletti 2002] have shown that Energy-dispersive X-ray diffraction (EDXRD) technique could be applied to characterize human breast tissues. The difference in diffraction peak positions of the main breast tissues namely adipose (fat) and glandular (muscle) forms the basis of this characterisation. The geometry of an EDXRD system decides the resolution of the system and hence the resolution of the spectral peaks obtained on it. Therefore, an optimal geometry of a diffraction system is the foremost requirement for setting up a realistic high resolution system. Diffraction systems have been successfully set up a number of times at UCL and used for small-sized material characterisation. The research outcomes have been approved and validated by scientific community. However, there has been no known protocol or system parameter set at UCL or elsewhere for characterisation of large samples. Hence the need for developing a computational model that could optimize parameters of a diffraction system for breast-sized samples and breast equivalent tissues. This chapter is dedicated to the development and predictions of the model. Following the section on development of the model, the model-predicted spectra have been presented. Further, these predictions have been

analysed using statistical techniques and the geometry of the EDXRD system has been optimised based on this analysis. The optimised system parameters have been used in setting up an EDXRD system. The spectra collected on this optimised system have been presented and discussed in the next chapter i.e. chapter 3.

2.1 Introduction

2.1.1 System Resolution: The resolution of diffraction spectra of samples collected on an Energy-dispersive X-ray diffraction (EDXRD) technique mainly relies on the energy resolution of the detector used and the geometrical resolution of the system. High-purity Germanium (HPGe) energy resolving detectors are widely used for diffraction systems as they are market's best energy resolving detector with energy resolution of less than 1% at 59.5 keV. The other factor for an improved spectrum resolution is the geometrical resolution of the system. As shown in Figure 2.1, X-ray photons originating from the X-ray tube pass through a source collimator of width d_1 and get scattered on interaction with the sample.

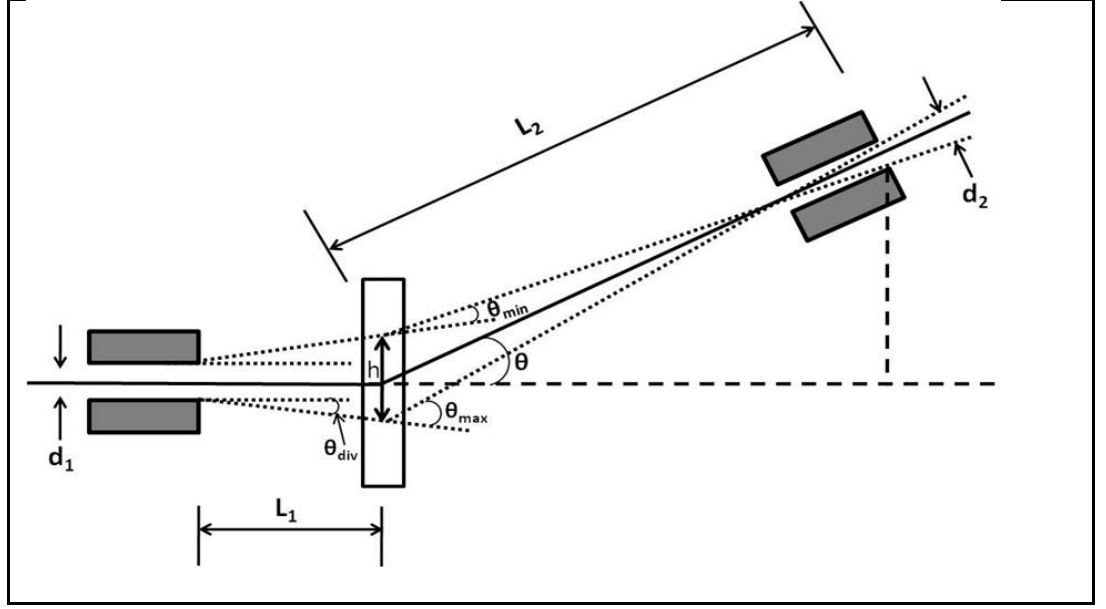


Figure 2.1: A schematic diagram of X-ray diffraction system [Source: Cook, 2008]

These scattered photons follow a path that has a range of angles with respect to the original path axis. A detector placed at an angle θ called the scatter angle collects all photons that are scattered at this angle. However, the detector collimator that offers a width d_2 provides a wider range to the angle θ . Hence, as seen in Figure 2.1 there will be photons scattered along and upto θ_{\min} and θ_{\max} direction too. These can be calculated geometrically using the expression [Cook, 2008] as follows:

$$\theta_{\min} = \tan^{-1} \left[\frac{L_2 \tan(\theta) - \frac{d_2}{2} \cos(\theta) - \frac{h}{2}}{L_2 + \frac{d_2}{2} \sin \theta} \right] - \theta_{\text{div}}$$

and

$$\theta_{\max} = \tan^{-1} \left[\frac{L_2 \tan(\theta) + \frac{d_2}{2} \cos(\theta) + \frac{h}{2}}{L_2 - \frac{d_2}{2} \sin \theta} \right] + \theta_{\text{div}}$$

where

$$h = d_1 + 2L_1 \tan(\theta_{\text{div}})$$

and the quantities have been marked in the schematic diagram of an X-ray diffraction system (Figure 2.1). Hence the whole range $\theta_{\text{max}} - \theta_{\text{min}}$ including the angle θ will be actually detected by the detector. This angular range is dependent on the distances between components of the system and collimator widths used in the system and gives the angular resolution of the system.

The significance of the two factors namely, energy and angular resolution, can be understood by understanding the parameters of an output diffraction spectrum. A diffraction spectrum collected on an EDXRD system is a plot of photon counts against energy of the photons. The energy axis is converted to momentum transfer values using the scatter angle used in the system. Momentum transfer χ is a function that relates the energy of photons E to the scatter angle of the system θ by Bragg relation in the following way,

$$\chi = \left(\frac{1}{hc}\right) * E * \sin\left(\frac{\theta}{2}\right)$$

where χ is measured in nm^{-1} , E is measured in keV, h is the Planck's constant in Js, c is the velocity of light in m/s and the scatter angle θ is measured in radians. The counts against momentum transfer kind of spectrum eases the comparison of results collected on different systems with different system geometries (i.e. different scatter angles). For a diffraction spectrum it can therefore be said that the smaller the width of the peaks the higher the spectrum resolution. Hence the shift

in momentum transfer value needs to be estimated to gain an idea about the spectral resolution. From the above equation, change in momentum transfer can be expressed in terms of change in E and θ to estimate the resolution of the system and the spectral peaks as follows:

$$\frac{\Delta\chi}{\chi} = \sqrt{\left(\frac{\Delta\theta}{\theta}\right)^2 + \left(\frac{\Delta E}{E}\right)^2}$$

For example, for a HPGe detector with an energy resolution of 0.54 keV at 59.5 keV one can calculate the value of $\Delta E/E$ to be $9.0\text{e-}3$. This number is small as compared to the $\Delta\theta/\theta$ for a realistic scatter angle with a range of 0.2. This fact points to the significance of collimator widths, which provide the angular range, used in EDXRD system in deciding the system resolution.

2.2 EDXRD diffraction system model based on ray tracing of photons

The Energy-dispersive X-ray diffraction (EDXRD) system model has been based on ray tracing of photons. In order to understand this tracing of photons, it is first important to understand the system components that limit the direction or passage of photons. In the presented work it is an EDXRD system and an EDXRD system consists of a source of photons, an X-ray tube and an energy-resolving detector like the HPGe detector. Figure 2.2 shows a schematic diagram of an EDXRD system set-up.

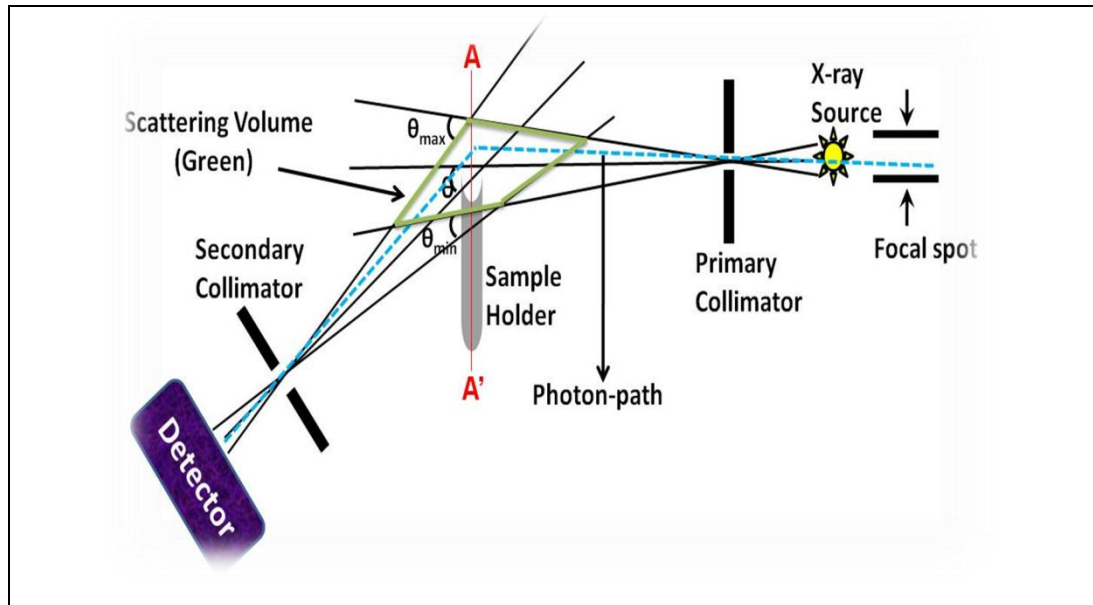


Figure 2.2: A schematic diagram showing EDXRD system set up

The photons diverging from the aperture of the X-ray source are limited using a collimator called the source collimator. The photons that pass through this collimator reach the sample. The photons undergo coherent scattering within the sample. The characterisation of materials using EDXRD diffraction system relies on this coherent scattering interaction of X-ray photons with the sample. In this phenomenon, the photons on entering the sample interact with the atoms of the sample in such a way that during this process they don't lose any of their energy but lose only their original path direction and therefore they get scattered in various directions. These scattered photons reach the detector after passing through a collimator, called the detector collimator, placed just before the detector. The detector and the detector collimator placed at the scatter angle collect all photons scattered at that angle within the angular range provided by the system. Not all scattered photons reach the detector as the detector and also the

detector collimator are positioned at an angle (called the scatter angle) to the original axis of photons. The positions of the X-ray source and the detector, the widths of the collimators and the sample size in the set-up form the important aspect that defines the system geometry and hence govern the spectral resolution. The model has been based on this photon path tracing.

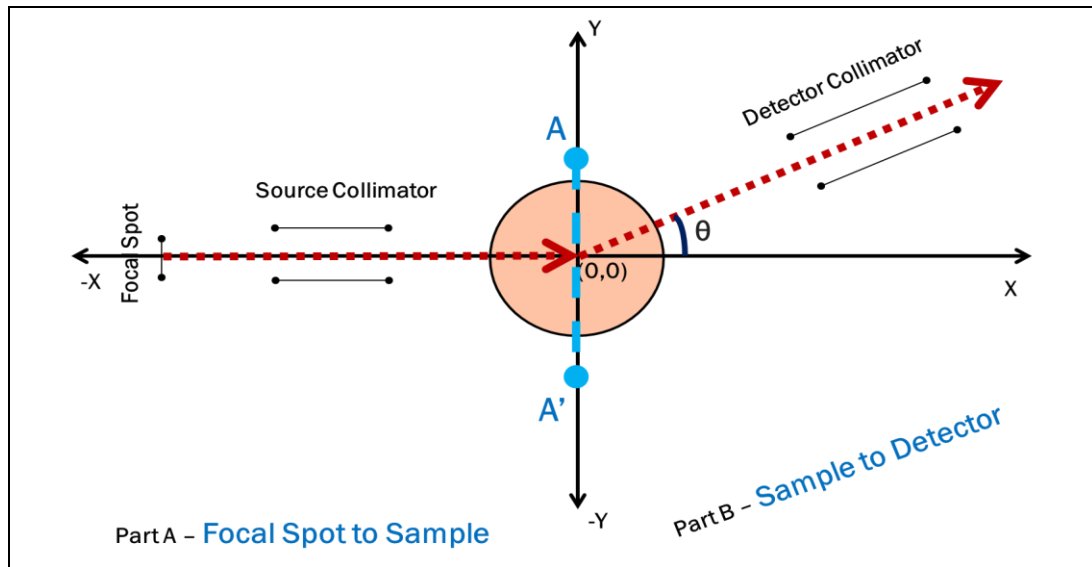


Figure 2.3: Schematic diagram representing the EDXRD system model development based on photon path tracing; AA' is the sample axis

A schematic diagram is shown in Figures 2.2 and 2.3 tracing the path of an input photon all the way from its origin, the focal spot, to the detector after passing through the sample wherein it interacts with the atoms and loses its original direction due to scattering. The details of this geometric ray-tracing have been discussed in the following section. The model has been developed using ITT software called IDL (Interactive Data Language). IDL is a popular software language used for data analysis in medical imaging and astronomy. IDL syntax is similar to that of Fortran and to some extent C.

2.3 Development of EDXRD system model

The photon ray tracing employed in the model has broadly two parts. The first one Part A covers the photon path from the focal spot to the sample axis. The number of photons reaching the source collimator and exiting it to reach the sample axis in the first instance depends on the width of the collimator and its length. The photons that reach the detector collimator to be read by the detector have been traced in the second part Part B of the model. This tracing is dependent on the size of the sample, the width and length of the detector collimator and the angle at which the detector and so the detector collimator have been placed. In terms of modelling the system, a co-ordinate system is set for the whole set-up wherein the centre of the sample is considered as the geometric origin (0,0) and all directions and angles are calculated with respect to this origin (Figure 2.3).

Part A of the model:

The part A of the model is for tracing the photons as they originate from the focal spot, enter the source collimator, exit it and then reach the sample. The model first obtains the size of the focal spot. All points on the focal spot are considered to carry equal number of photons. The focal spot is divided into small points of size one micron. In order to trace the path of a photon originating from any of these points, the following are obtained: the co-ordinates of the point on the focal spot and the co-ordinates corresponding to the source collimator (both at the photon entry and photon exit planes) as shown in Figure 2.4. From this information, for each of the focal spot points, using the angular range -180 to +180 degree with

step size as small as 0.5 the y co-ordinates corresponding to each of the angles can be obtained. This y co-ordinate is the point at which photons hit the plane due to the source collimator. The process is repeated for all points on the focal spot. From this information, points that fall out of the angular range provided by the size of the source collimator are filtered out and only those points that are within the collimator size are considered as shown in Figures 2.4a-d.

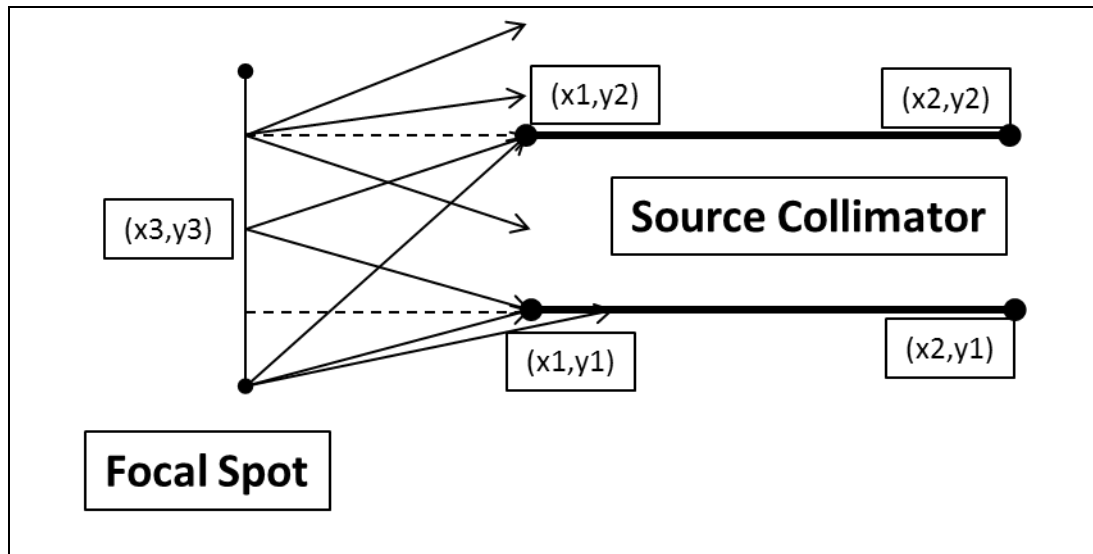


Figure 2.4a: Ray tracing of photons along focal spot-source collimator path

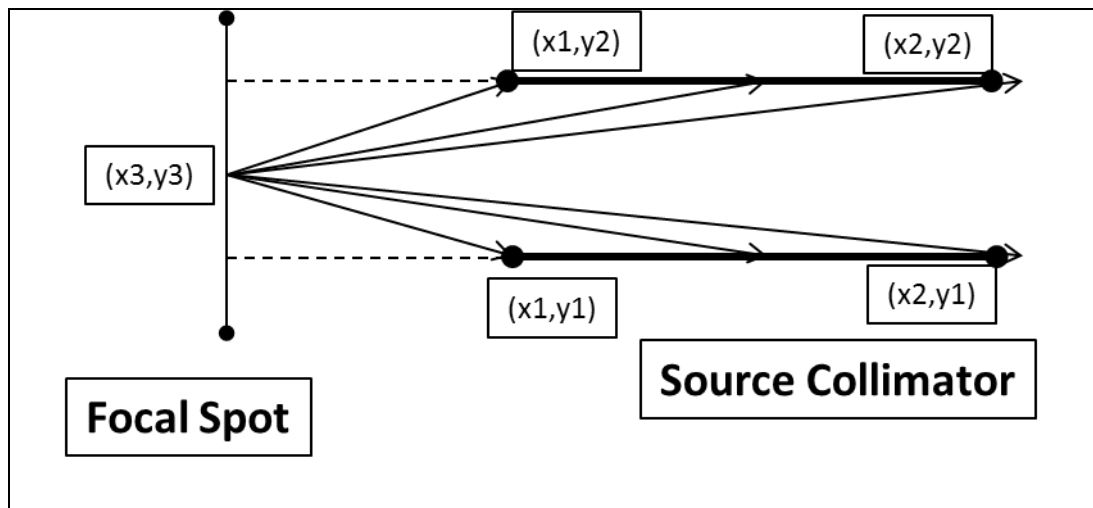


Figure 2.4b: Ray tracing of photons along focal spot-source collimator path

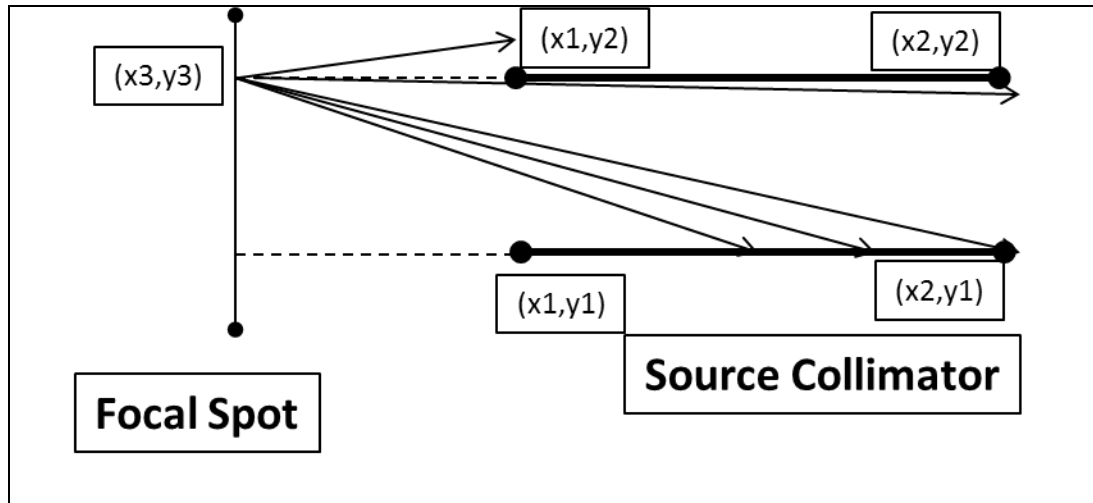


Figure 2.4c: Ray tracing of photons along focal spot-source collimator path

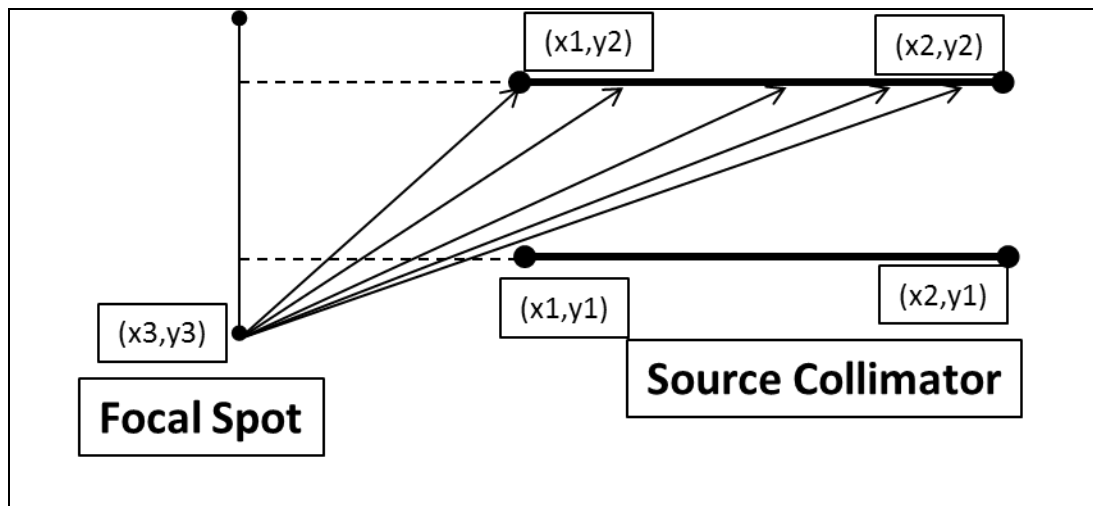


Figure 2.4d: Ray tracing of photons along focal spot-source collimator path

Therefore, only those angles that permit photons to enter and exit through the width of the source collimator are taken forward, as shown in Figure 2.4e below.

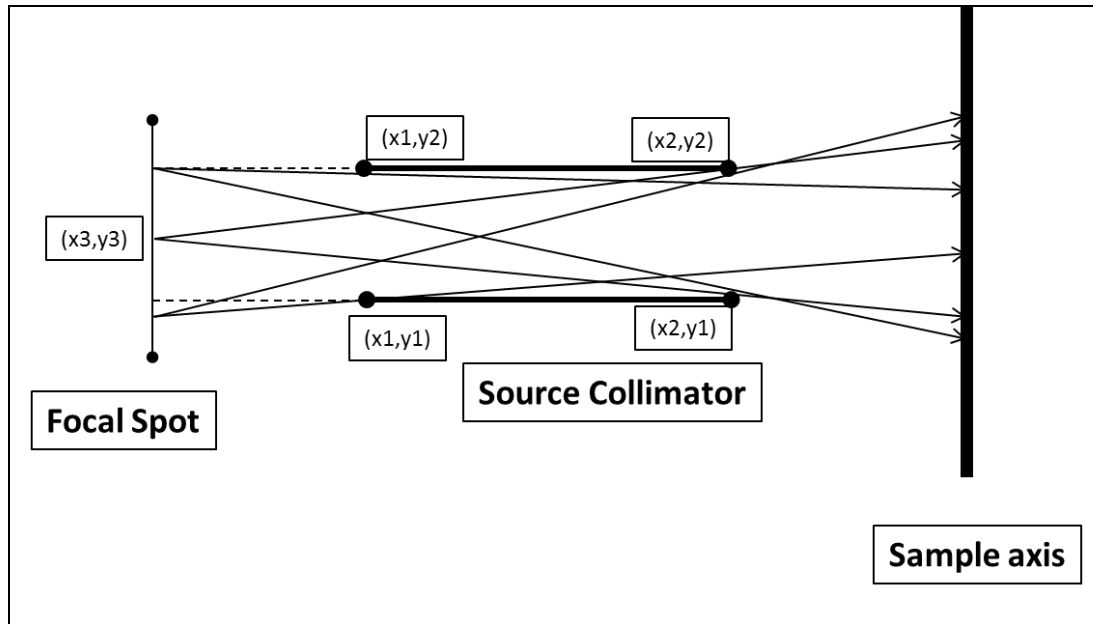


Figure 2.4e: Ray tracing of photons along focal spot-source collimator-sample path

Further, for such photons that get through the source collimator the co-ordinate positions where they hit the sample axis are recorded for the second part of the model. From the number of photons reaching the sample axis corresponding to a position on this axis an intensity profile can be generated.

Part B of the model:

In Part A the photons had travelled from focal spot to the sample through the constraint posed by the width of the source collimator. Part B of the model is dedicated to the ray tracing of photons from the sample on to the detector.

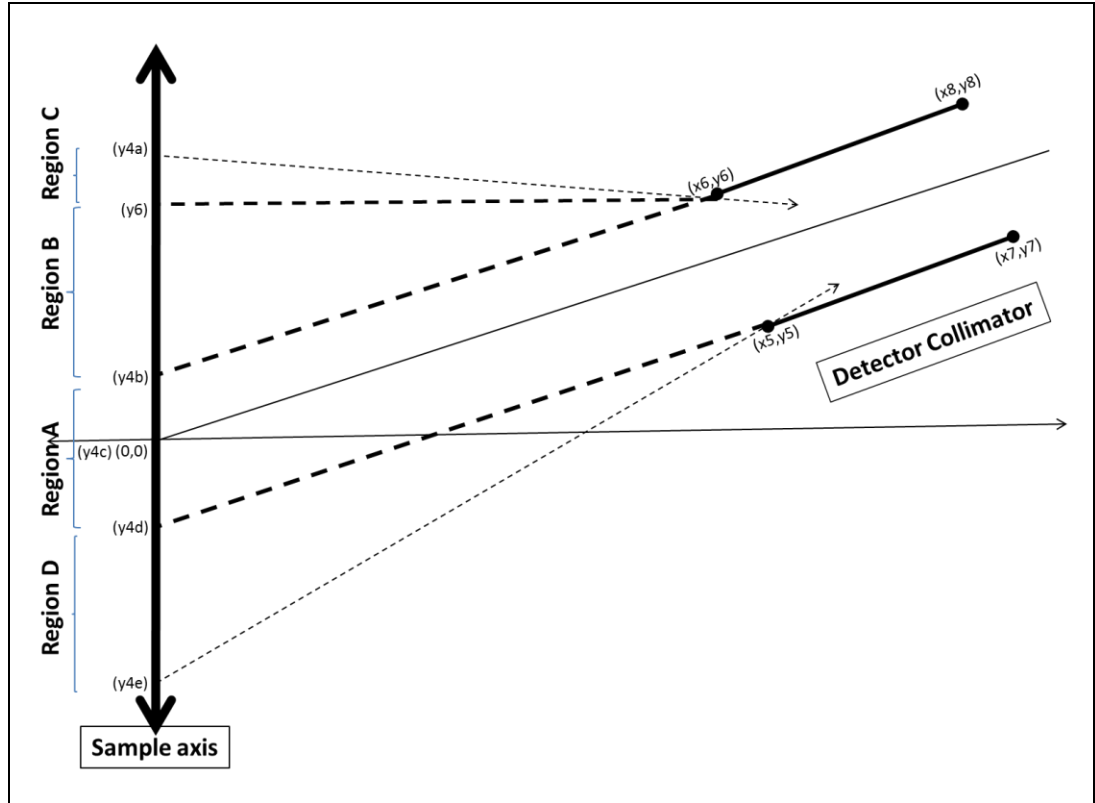


Figure 2.5: Ray tracing of photons along sample-detector collimator path

The detector collimator width is obtained. From the photon positions recorded in part A and in particular, the top and bottom values, the range of photons on the sample axis is obtained. As seen from Figure 2.5 photons with positions falling out of the range, $y4a$ to $y4e$ that can be seen by the detector collimator, would never be able to reach the detector and are therefore discarded. The photon profile at the sample axis is then divided into points of a micron size. For each of these

points on the samples, depending on the width of the detector collimator, an angular range (θ_{\min} and θ_{\max}) is calculated. These points would fall under different regions on the sample axis as shown in Figure 2.5. This angular range is recorded as it includes all such photons at the sample that can be seen by the detector through the detector collimator. Therefore, the output at this stage is a table of angle and the regions on the sample axis in which the photons hit. Starting from θ_{\min} to θ_{\max} in steps of 1/1000 of a radian, a corresponding energy value is obtained using the input momentum transfer values (JCPDS diffraction data) (explained in the next section) to form a profile as per the following expression:

$$E = (\chi * hc) / \sin (\theta/2)$$

These energy values are stored and photons corresponding to one energy value are counted. At this stage a photon diffraction profile has been generated that gives number of photons against their energy value.

When a sample of some width is placed between the two collimators, the sample (its width) is divided into thin strips of size 1/100 mm and a photon profile is generated as explained above. In this case, the range of photon positions on the sample axis would be different depending on the dimension in the y-direction and the size of the collimators that define the region on the sample axis.

2.4 Model inputs for spectrum prediction

In order to predict a spectrum the model requires the size of the focal spot in addition to sizes of collimators and other geometrical distances of the system. As explained in section 2.3, the model ray traces the photon path and calculates a set of angles for each point on the sample that could be seen by the detector. Using each of these angles, an energy value corresponding to each of the momentum transfer lines of the input sample spectra (JCPDS diffraction data) is calculated to obtain a predicted diffraction profile for a sample. Figure 2.6 shows a block diagram representing the EDXRD model.

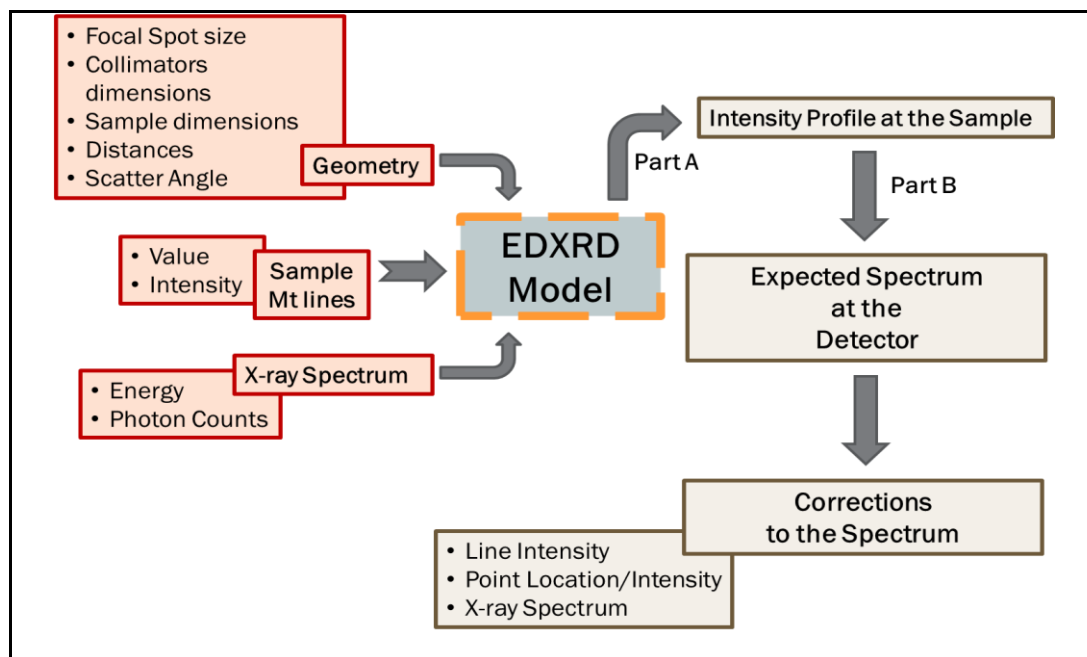


Figure 2.6: Block diagram representing the EDXRD system model; Mt stands for Momentum Transfer; Sample Mt lines refer to JCPDS diffraction spectral lines

For the presented research work, an industrial tungsten anode tube was used as a source of X-rays that produced X-rays in the range 10-110 keV. This range is optimal for the material and thickness of samples used. High-purity Germanium

(HPGe) is market's best energy resolving detector with energy resolution of less than 1% at 59.5 keV and hence has been used for the purpose of collecting the scattered photons and reading out this information in the form of diffraction spectra. The collimators are variable shaped holders in a brass block that allows different collimator widths. Hence, parameters considered that can be varied to optimize the system geometry are the following:

- i. X-ray source voltage (kVp) to obtain desired photon energy (keV)
- ii. Aperture of source collimator
- iii. Size of detector collimator
- iv. Scatter angle

The model is provided with variable geometrical parameters and an energy resolution as measured on the HPGe detector. The computational model tests different combinations of the above parameters. The program is run to predict spectra. The model predictions are then used to optimize best combination of these parameters in terms of spectral resolution and hence material characterization.

The following are the inputs of the model:

1. The X-ray spectrum was generated using software called XCOMP5R that allows multiple kV_p values in one run and generates up to 5 X-ray source spectra at a time. Other inputs to the software are the focal spot size and distance of the detector from the source.
2. The geometrical parameters such as the collimator sizes and lengths, the distances between various components of the system and the scatter angle.
3. The standard diffraction profiles of a range of materials published by the International Centre for Diffraction Data (ICDD) is available in the form of powder diffraction file collection called the JCPDS, an acronym for Joint Committee on Powder Diffraction Standards. As an input to the model a JCPDS profile of the sample is provided. This spectrum has diffraction peak lines that provided the intensity and position of lines on momentum transfer scale.
4. The detector resolution in the form of a Gaussian function is generated as part of the code. This Gaussian function is convolved with the sample profile to include the effect of the energy resolution provided by the detector on the spectrum.

2.4.1 Corrections to profile:

The model predicted diffraction profile is corrected for the following factors.

1. The profile is corrected for the shape of the input X-ray spectrum by multiplying the profile by the normalised X-ray spectrum.
2. The profile obtained is convolved with the Gaussian function representing the energy resolution of the detector.
3. The shape of the collimator correction is done by adjusting the intensity with a shape factor. The shape factor is obtained by calculating the length of the chord of the circles of the cylindrical collimators.
4. The attenuation due to material of the sample is applied by multiplying the profile by a negative exponent of the product of the attenuation coefficient of the material and the thickness of the sample.

The corrected diffraction profile obtained is a number of photons against energy plot. The energy axis is converted to momentum transfer axis using the Bragg relation for a given scatter angle. The model predicted profile is then compared with experimentally measured spectrum.

2.4.2 Parameter set: The set of collimators used for the model are of following widths (in mm): 0.5, 0.9, 1.0, 1.1, 1.2, 1.5, 1.6, 1.7, 1.8, 1.9 and 2.0. Based on the angular resolution these collimators provide, the momentum transfer range they cover and other factors, pairs were made out of these collimators and thirteen sets were obtained as a result (Tables 2.1 and 2.2).

Table 2.1: Angular resolution and momentum transfer range provided by different combinations of collimator sets;

d1=width of source collimator in mm; d2=width of detector collimator in mm

d1 (mm)	d2 (mm)	θ_{\min} (degree)	θ_{\max} (degree)	$\theta_{\max} - \theta_{\min}$ (degree)	Angular resolution at 6 degree	For an average energy of 35 keV		
						χ_{\min} (nm ⁻¹)	χ_{\max} (nm ⁻¹)	$\chi_{\max} - \chi_{\min}$ (nm ⁻¹)
0.5	0.5	5.209	6.790	1.581	0.263	2.093	2.728	0.635
0.5	0.9	4.944	7.055	2.111	0.352	1.987	2.834	0.847
0.9	0.5	4.887	7.110	2.223	0.371	1.964	2.857	0.892
0.5	1	4.878	7.121	2.244	0.374	1.960	2.861	0.901
0.5	1.1	4.811	7.187	2.376	0.396	1.934	2.887	0.954
1	0.5	4.807	7.190	2.384	0.397	1.932	2.889	0.957
0.5	1.2	4.745	7.254	2.509	0.418	1.907	2.914	1.007
1.1	0.5	4.726	7.270	2.544	0.424	1.899	2.921	1.021
1.2	0.5	4.646	7.350	2.705	0.451	1.867	2.953	1.086
0.9	0.9	4.622	7.375	2.753	0.459	1.858	2.963	1.105
0.9	1	4.556	7.441	2.886	0.481	1.831	2.989	1.158
0.5	1.5	4.546	7.452	2.906	0.484	1.827	2.994	1.167
1	0.9	4.541	7.455	2.914	0.486	1.825	2.995	1.170
0.9	1.1	4.489	7.507	3.018	0.503	1.804	3.016	1.212
0.5	1.6	4.480	7.518	3.039	0.506	1.800	3.020	1.220
1	1	4.475	7.521	3.046	0.508	1.799	3.021	1.223
1.1	0.9	4.461	7.535	3.074	0.512	1.793	3.027	1.234
0.9	1.2	4.423	7.574	3.151	0.525	1.778	3.042	1.265
0.5	1.7	4.413	7.585	3.171	0.529	1.774	3.047	1.273
1	1.1	4.409	7.587	3.179	0.530	1.772	3.048	1.276
1.5	0.5	4.404	7.590	3.186	0.531	1.770	3.049	1.279
1.1	1	4.394	7.601	3.207	0.534	1.766	3.054	1.287
1.2	0.9	4.380	7.615	3.235	0.539	1.760	3.059	1.299
0.5	1.8	4.347	7.651	3.304	0.551	1.747	3.073	1.326
1	1.2	4.342	7.654	3.311	0.552	1.745	3.075	1.329

Table 2.1 (contd.): Angular resolution and momentum transfer range provided by different combinations of collimator sets;

d1=width of source collimator in mm; d2=width of detector collimator in mm

d1 (mm)	d2 (mm)	θ_{\min} (degree)	θ_{\max} (degree)	$\theta_{\max} - \theta_{\min}$ (degree)	Angular resolution at 6 degree	For an average energy of 35 keV		
						χ_{\min} (nm ⁻¹)	χ_{\max} (nm ⁻¹)	$\chi_{\max} - \chi_{\min}$ (nm ⁻¹)
1.1	1.1	4.328	7.667	3.339	0.557	1.740	3.080	1.341
1.6	0.5	4.323	7.670	3.347	0.558	1.738	3.081	1.344
1.2	1	4.314	7.681	3.367	0.561	1.734	3.086	1.352
0.5	1.9	4.281	7.717	3.436	0.573	1.721	3.100	1.379
1.1	1.2	4.262	7.734	3.472	0.579	1.713	3.107	1.394
1.2	1.1	4.248	7.747	3.500	0.583	1.707	3.112	1.405
1.7	0.5	4.243	7.750	3.507	0.585	1.705	3.113	1.408
0.9	1.5	4.224	7.772	3.548	0.591	1.698	3.122	1.424
0.5	2	4.215	7.783	3.569	0.595	1.694	3.126	1.433
1.2	1.2	4.181	7.813	3.632	0.605	1.681	3.139	1.458
1.8	0.5	4.162	7.830	3.668	0.611	1.673	3.145	1.472
0.9	1.6	4.158	7.838	3.681	0.613	1.671	3.149	1.478
1	1.5	4.143	7.852	3.709	0.618	1.665	3.154	1.489
1.5	0.9	4.139	7.855	3.716	0.619	1.663	3.155	1.492
0.9	1.7	4.091	7.904	3.813	0.636	1.644	3.175	1.531
1.9	0.5	4.082	7.910	3.828	0.638	1.640	3.177	1.537
1	1.6	4.077	7.918	3.841	0.640	1.639	3.181	1.542
1.5	1	4.072	7.921	3.849	0.641	1.637	3.182	1.545
1.1	1.5	4.063	7.932	3.869	0.645	1.633	3.186	1.553
1.6	0.9	4.058	7.935	3.877	0.646	1.631	3.187	1.556
0.9	1.8	4.025	7.971	3.946	0.658	1.618	3.202	1.584
1	1.7	4.011	7.984	3.974	0.662	1.612	3.207	1.595
1.5	1.1	4.006	7.987	3.981	0.664	1.610	3.208	1.598
2	0.5	4.001	7.990	3.989	0.665	1.608	3.209	1.601
1.1	1.6	3.996	7.998	4.002	0.667	1.606	3.213	1.606
1.6	1	3.992	8.001	4.009	0.668	1.604	3.214	1.609
1.2	1.5	3.982	8.012	4.030	0.672	1.601	3.218	1.618
1.7	0.9	3.977	8.014	4.037	0.673	1.599	3.219	1.621
0.9	1.9	3.959	8.037	4.078	0.680	1.591	3.228	1.637
1	1.8	3.944	8.050	4.106	0.684	1.585	3.234	1.648
1.5	1.2	3.939	8.053	4.114	0.686	1.583	3.235	1.651
1.1	1.7	3.930	8.064	4.134	0.689	1.580	3.239	1.660
1.6	1.1	3.925	8.067	4.142	0.690	1.578	3.240	1.663
1.2	1.6	3.916	8.078	4.162	0.694	1.574	3.245	1.671
1.7	1	3.911	8.081	4.170	0.695	1.572	3.246	1.674
1.8	0.9	3.897	8.094	4.198	0.700	1.566	3.251	1.685

Table 2.1 (contd.): Angular resolution and momentum transfer range provided by different combinations of collimator sets;

d1=width of source collimator in mm; d2=width of detector collimator in mm

d1 (mm)	d2 (mm)	θ_{\min} (degree)	θ_{\max} (degree)	$\theta_{\max} - \theta_{\min}$ (degree)	Angular resolution at 6 degree	For an average energy of 35 keV		
						χ_{\min} (nm ⁻¹)	χ_{\max} (nm ⁻¹)	$\chi_{\max} - \chi_{\min}$ (nm ⁻¹)
0.9	2	3.892	8.103	4.210	0.702	1.564	3.255	1.690
1	1.9	3.878	8.117	4.238	0.706	1.559	3.260	1.701
1.1	1.8	3.864	8.130	4.266	0.711	1.553	3.266	1.713
1.6	1.2	3.859	8.133	4.274	0.712	1.551	3.267	1.716
1.2	1.7	3.850	8.144	4.294	0.716	1.547	3.271	1.724
1.7	1.1	3.845	8.147	4.302	0.717	1.545	3.272	1.727
1.8	1	3.830	8.160	4.330	0.722	1.540	3.278	1.738
1.9	0.9	3.816	8.174	4.358	0.726	1.534	3.283	1.749
1	2	3.812	8.183	4.371	0.728	1.532	3.287	1.755
1.1	1.9	3.798	8.196	4.399	0.733	1.526	3.292	1.766
1.2	1.8	3.783	8.210	4.427	0.738	1.521	3.298	1.777
1.7	1.2	3.778	8.213	4.434	0.739	1.519	3.299	1.780
1.8	1.1	3.764	8.226	4.462	0.744	1.513	3.304	1.791
1.9	1	3.750	8.240	4.490	0.748	1.507	3.310	1.803
1.5	1.5	3.740	8.251	4.511	0.752	1.503	3.314	1.811
2	0.9	3.735	8.254	4.518	0.753	1.501	3.315	1.814
1.1	2	3.731	8.263	4.531	0.755	1.500	3.319	1.819
1.2	1.9	3.717	8.276	4.559	0.760	1.494	3.324	1.830
1.8	1.2	3.698	8.292	4.595	0.766	1.486	3.331	1.845
1.9	1.1	3.683	8.306	4.623	0.770	1.480	3.336	1.856
1.5	1.6	3.674	8.317	4.643	0.774	1.477	3.341	1.864
2	1	3.669	8.320	4.651	0.775	1.475	3.342	1.867
1.6	1.5	3.660	8.331	4.671	0.779	1.471	3.346	1.875
1.2	2	3.651	8.342	4.692	0.782	1.467	3.351	1.883
1.9	1.2	3.617	8.372	4.755	0.793	1.454	3.363	1.909
1.5	1.7	3.608	8.383	4.776	0.796	1.450	3.367	1.917
2	1.1	3.603	8.386	4.783	0.797	1.448	3.368	1.920
1.6	1.6	3.593	8.397	4.804	0.801	1.444	3.373	1.928
1.7	1.5	3.579	8.411	4.832	0.805	1.439	3.378	1.940
1.5	1.8	3.541	8.450	4.908	0.818	1.423	3.394	1.970
2	1.2	3.536	8.452	4.916	0.819	1.421	3.395	1.973

Table 2.1 (contd.): Angular resolution and momentum transfer range provided by different combinations of collimator sets;

d1=width of source collimator in mm; d2=width of detector collimator in mm

d1 (mm)	d2 (mm)	θ_{min} (degree)	θ_{max} (degree)	$\theta_{max} - \theta_{min}$ (degree)	Angular resolution at 6 degree	For an average energy of 35 keV		
						χ_{min} (nm ⁻¹)	χ_{max} (nm ⁻¹)	$\chi_{max} - \chi_{min}$ (nm ⁻¹)
1.6	1.7	3.527	8.463	4.936	0.823	1.418	3.399	1.981
1.7	1.6	3.513	8.477	4.964	0.827	1.412	3.405	1.993
1.8	1.5	3.499	8.491	4.992	0.832	1.406	3.410	2.004
1.5	1.9	3.475	8.516	5.040	0.840	1.397	3.420	2.023
1.6	1.8	3.461	8.529	5.068	0.845	1.391	3.426	2.035
1.7	1.7	3.447	8.543	5.096	0.849	1.385	3.431	2.046
1.8	1.6	3.432	8.557	5.124	0.854	1.380	3.437	2.057
1.9	1.5	3.418	8.570	5.152	0.859	1.374	3.442	2.068
1.5	2	3.409	8.582	5.173	0.862	1.370	3.447	2.076
1.6	1.9	3.395	8.595	5.201	0.867	1.364	3.452	2.088
1.7	1.8	3.380	8.609	5.229	0.871	1.359	3.458	2.099
1.8	1.7	3.366	8.623	5.257	0.876	1.353	3.463	2.110
1.9	1.6	3.352	8.636	5.285	0.881	1.347	3.469	2.121
2	1.5	3.337	8.650	5.313	0.885	1.341	3.474	2.133
1.6	2	3.328	8.661	5.333	0.889	1.338	3.479	2.141
1.7	1.9	3.314	8.675	5.361	0.894	1.332	3.484	2.152
1.8	1.8	3.300	8.689	5.389	0.898	1.326	3.490	2.163
1.9	1.7	3.285	8.702	5.417	0.903	1.320	3.495	2.175
2	1.6	3.271	8.716	5.445	0.908	1.315	3.501	2.186
1.7	2	3.248	8.741	5.493	0.916	1.305	3.511	2.205
1.8	1.9	3.233	8.755	5.521	0.920	1.300	3.516	2.216
1.9	1.8	3.219	8.768	5.549	0.925	1.294	3.521	2.228
2	1.7	3.205	8.782	5.577	0.930	1.288	3.527	2.239
1.8	2	3.167	8.821	5.654	0.942	1.273	3.542	2.270
1.9	1.9	3.153	8.834	5.682	0.947	1.267	3.548	2.281
2	1.8	3.138	8.848	5.710	0.952	1.261	3.553	2.292
1.9	2	3.086	8.900	5.814	0.969	1.241	3.574	2.334
2	1.9	3.072	8.914	5.842	0.974	1.235	3.580	2.345
2	2	3.006	8.980	5.974	0.996	1.208	3.606	2.398

Table 2.2: Angular resolution of the selected 13 collimator sets in increasing order of angular resolution values;
d1=width of source collimator in mm;
d2=width of detector collimator in mm

Set	d1 (mm)	d2 (mm)	Angular resolution at 6 degree
4	0.5	0.9	0.059
5	0.5	1.0	0.062
3	0.5	1.1	0.066
2	1.1	0.5	0.071
10	1.2	0.5	0.075
6	0.5	1.5	0.081
7	0.9	1.1	0.084
1	1.1	0.9	0.085
8	1.0	1.1	0.088
9	1.2	0.9	0.090
11	1.0	1.2	0.092
12	1.2	1.0	0.094
13	1.1	1.2	0.096

As mentioned previously, the breast tissue characterisation is based on difference in the spectral peak positions and intensities. The peaks corresponding to adipose and glandular tissues of the breast appear at 1.1 nm^{-1} and 1.6 nm^{-1} respectively. Hence samples used for the model were selected based on their momentum transfer range ($0.5\text{--}3.0 \text{ nm}^{-1}$) in the diffraction spectra. This range was optimal for the work as it covered the average photon energy range provided by 10–110 kV_p value applied on the X-ray tube at scatter angular range of 4–8 degree. These considerations led to the choice of materials tabulated in Table 2.3. For system optimization, five kV_p values were chosen namely, 40, 50, 60, 70 and 80 and five scatter angle values (in degree) namely, 4, 5, 6, 7 and 8 that provided photon energies corresponding to momentum transfer range $0.5\text{--}3.0 \text{ nm}^{-1}$. Samples used

for the model included plastics, pharmaceutical drugs and commonly used salts/powders that were selected based on the momentum transfer values of the peak positions and number of peaks in their characteristic (JCPDS) spectra. These samples have been tabulated in Table 2.3.

Table 2.3: Sample set used for the model	
No.	Sample
1	Polystyrene (PS)
2	Polyvinyl chloride (PVC)
3	Polymethylmethacrylate (PMMA)
4	Polytetrafluoroethylene (PTFE)
5	Polypropylene (PP)
6	Polyethylene (PE)
7	Paracetamol
8	Caffeine
9	Green Tea
10	Anadin
11	Bicarbonate of soda
12	Ibuprofen
13	Sea-salt
14	Hayfever drug
15	Multivitamin
16	Caster sugar
17	Demerara sugar
18	Granulated sugar
19	Muscavado sugar
20	Hermesetes sweetner

2.5 Model Predictions

Input set 1:

- Focal Spot size: 1.0 mm
- Collimator widths (mm) : 0.5 (p_c), 0.9 (s_c)
- Collimator lengths (mm) : 20 (p_c), 20 (s_c)
- Distance (mm) : fs-280-p_c-45-s_c-25-detector
(fs: focal spot; p_c: source collimator; s_c: detector collimator)
- Scatter Angle : 6 degree
- kV_p : 70
- X-ray anode: Tungsten

An X-ray input spectrum (Tungsten) as shown in Figure 2.7 was generated using XCOMP5R and used as an input to the model.

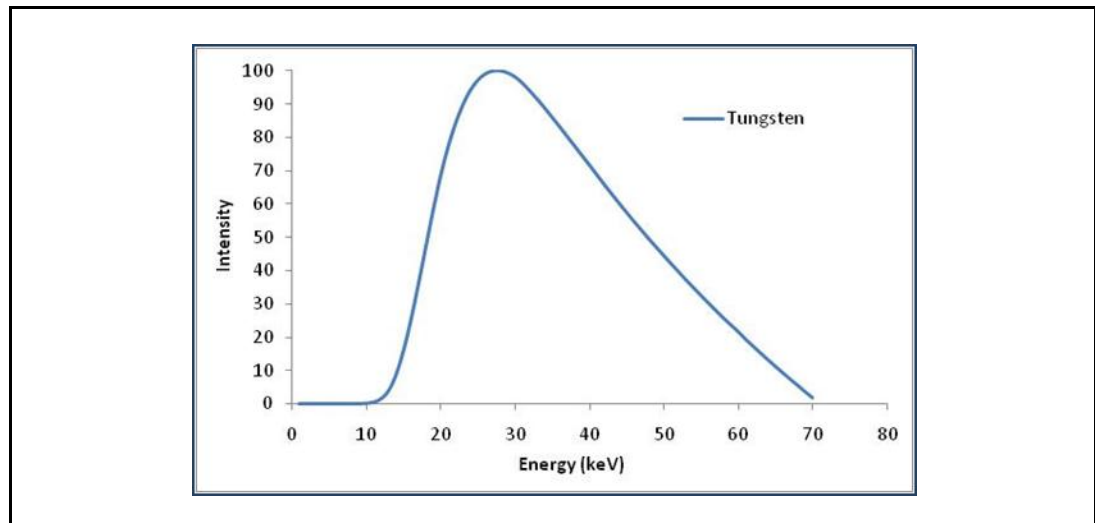


Figure 2.7: X-ray spectrum for Tungsten 70kV_p

The code was run for a 70kV_p Tungsten X-ray source with a focal spot size 1 mm. Other geometrical parameters are given above. The Part A of the model gave the following (Figure 2.8) intensity profile at the sample axis.

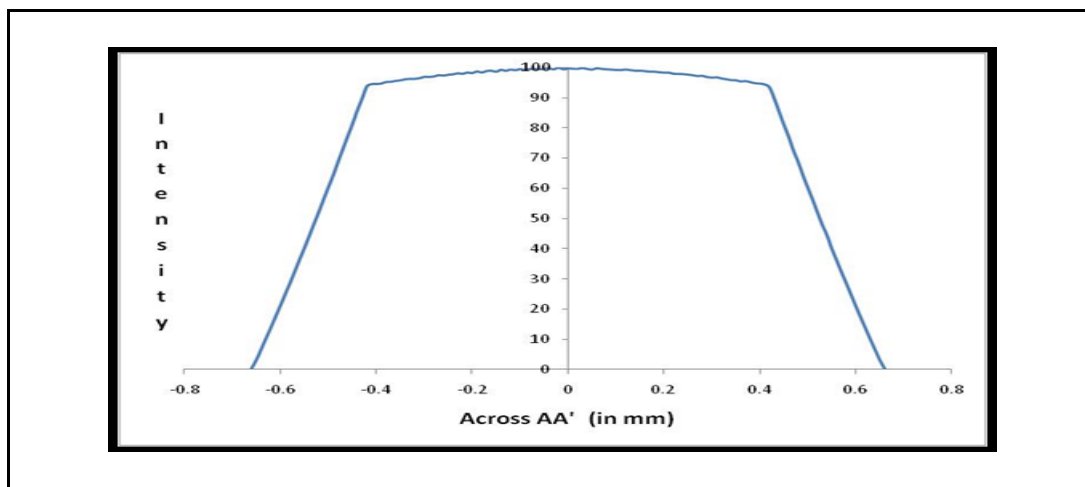


Figure 2.8: Photon intensity profile at the sample

As seen in Figure 2.8, the photon intensity has a maximum at the centre of the sample and gradually reduces as we move towards the edge of the sample. This is a true reflection of the angular range and hence scattering volume provided by the system geometry. Following the part A, the part B of the code was run with Paracetamol (size: 5 X 50mm cylinder) as the sample. The model predicted spectrum is shown in Figure 2.9 that compares this predicted spectrum with experimentally measured and JCPDS spectra.

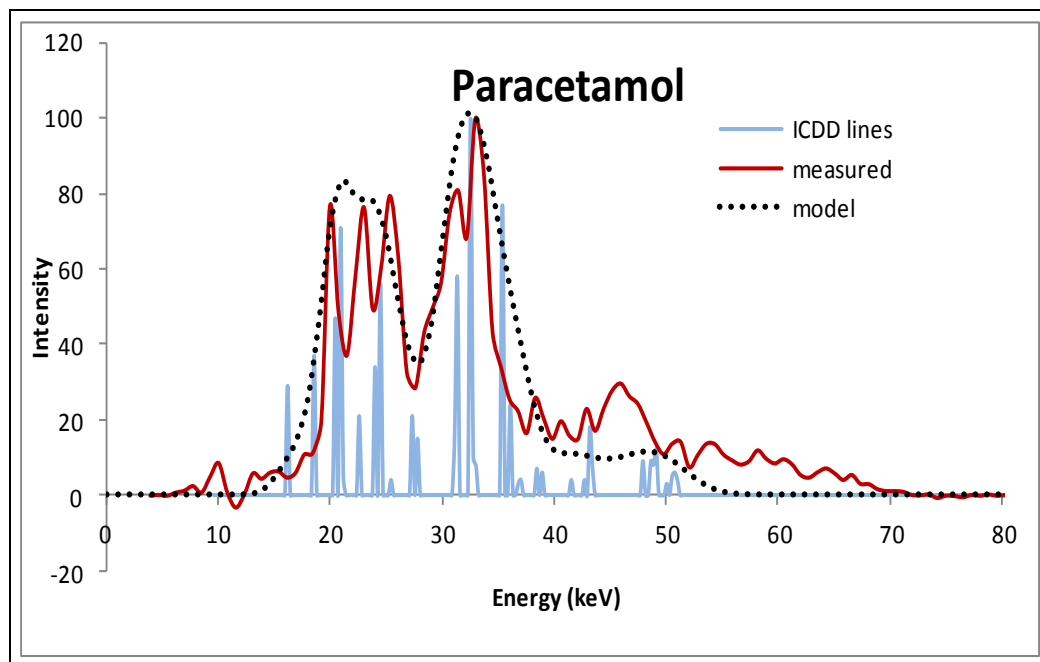


Figure 2.9: Model prediction against measured diffraction spectra for Paracetamol; Dotted curve-model predicted; Solid red curve-measured; Solid blue line-ICDD JCPDS data

Other diffraction spectra predicted by the model using this geometry are shown in Figures 2.10 and 2.11. These correspond to the diffraction spectra for PTFE and PE.

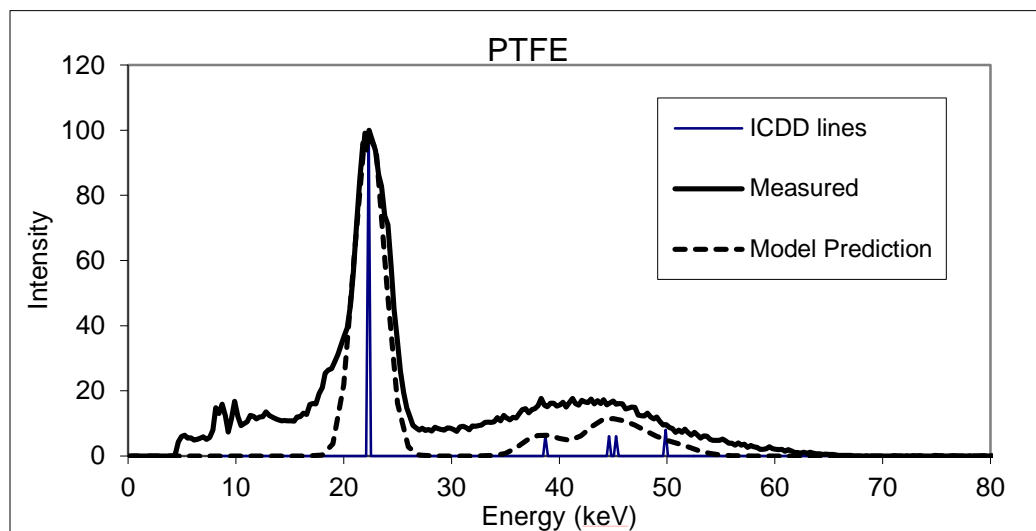


Figure 2.10: Model prediction against measured diffraction data for PTFE; Dashed curve-model predicted; Solid black curve-measured; Solid blue line-ICDD JCPDS data

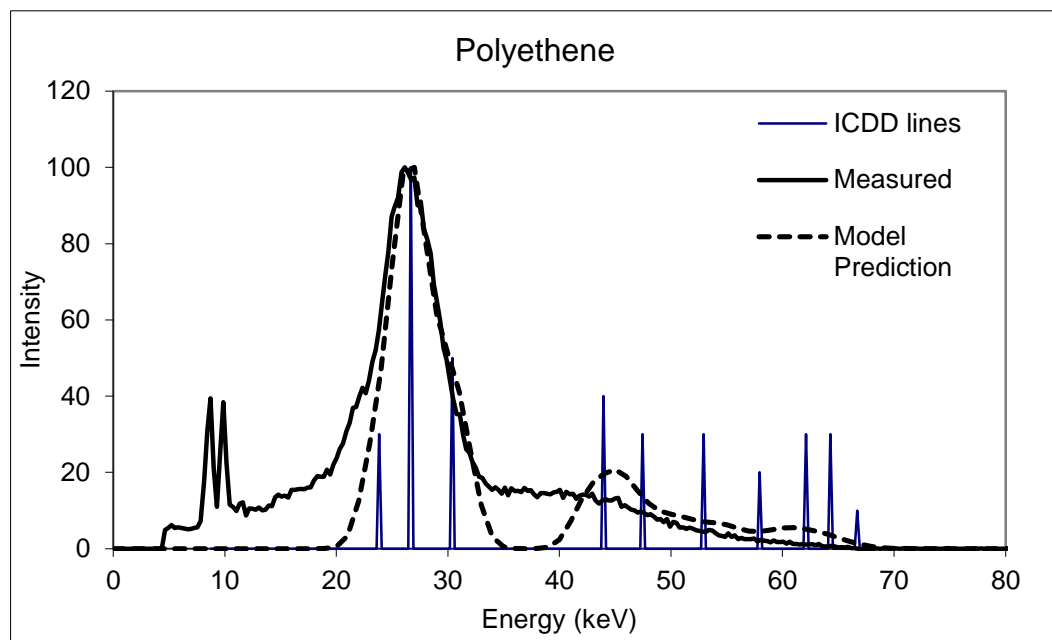


Figure 2.11: Model prediction against measured diffraction data for PE; Dashed curve-model predicted; Solid black curve-measured; Solid blue line-ICDD JCPDS data

Input set 2:

The model code was tested with a different set of geometrical parameters as input as given here:

- Focal Spot size: 1.0 mm
- Collimator widths (mm): 1.0 (p_c), 1.0 (s_c)
- Collimator lengths (mm) : 56 (p_c), 119 (s_c)
- Distance (mm) : fs-40-p_c-170-sample-155.5-s_c-40.5-detector
(fs: focal spot; p_c: source collimator; s_c: detector collimator)
- Scatter Angle : 7 degree
- kV_p : 80
- X-ray anode: Tungsten

The predicted spectrum for Paracetamol for this geometry along with measured and JCPDS spectra have been shown in Figure 2.12.

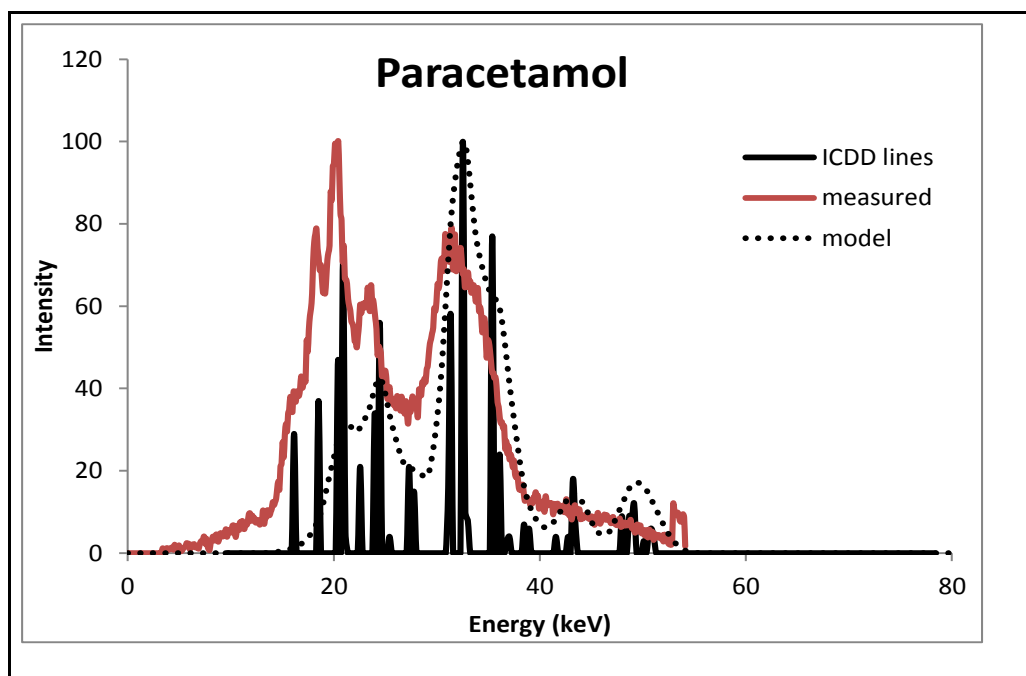


Figure 2.12: Model prediction against measured diffraction data for Paracetamol (input set 2); Dotted curve-model predicted; Solid red curve-measured; Solid black line-ICDD JCPDS data

2.6 Spectral analysis

A spectral analysis has been performed on the presented spectra to estimate the peak parameters like number of peaks, peak position and peak width as compared to the expected spectrum.

Table 2.4: Spectral analysis for model predicted spectra				
Sample/set up	No. of peaks (expected JCPDS peak)	Peak positions	Peak shifts (nm⁻¹)	Peak widths (FWHM) (nm⁻¹)
Fig. 2.9 Paracetamol	2 (8)	Broad Peaks 0.88, 1.34 nm ⁻¹ or 21.00, 32.00 keV	-0.10	0.57
Fig. 2.12 Paracetamol	3 (8)	Broad Peaks 0.884, 1.03, 1.37 nm ⁻¹ or 20.99, 24.49, 32.66 keV	-0.12	0.48
Fig. 2.10 PTFE	1 + 2 (1 main + 3)	1.0 nm ⁻¹ or 23.6 keV	-0.10	0.13
Fig. 2.11 PE	2 + 1 (4+6)	1.01, 1.20, 1.30 nm ⁻¹ or 25.6, 28.9, 32.1 keV	-0.11	0.35

Looking at diffraction spectra in Figures 2.9 - 2.12, the model predicted spectra have peaks about the expected positions with a shift of 0.10 nm⁻¹. The model has convolved the peaks into few broad peaks. The PTFE and PE spectra show peaks within 0.10 nm⁻¹ of the expected peak positions. The average peak width (FWHM) has been found to be 0.52 nm⁻¹ for multi-peak spectra and is more narrow (an average of 0.20 nm⁻¹) for samples with fewer characteristic peaks. This difference in model predictions is characteristic of the materials of the sample, their short-range structure and purity.

Input set 3:

The model was run for the all the collimator sets with rest of the system parameters fixed as given below:

- Focal Spot size: 1.0 mm
- Collimator widths (mm): variable
- Collimator lengths (mm) : 20 (p_c), 20 (s_c)
- Distance (mm) : fs-280-p_c-45-s_c-25-detector
(fs: focal spot; p_c: source collimator; s_c: detector collimator)
- Scatter Angle : 6 degree
- kV_p : 70
- X-ray anode: Tungsten

Spectra were generated and a spectral analysis was performed for all the collimator sets in terms of the number of peaks, peak position and peak width as compared to the expected spectrum. This is shown in Tables 2.5, 2.6 and 2.7.

Table 2.5: Spectral analysis for model predicted spectra for all collimator sets – number of peaks

(multi-pe refers to multiple peaks; yellow shade shows about 80-90% agreement between model predicted and measured+JCPDS data; the blue bar at the bottom of the table gathers maximal yellow shaded columns together to show the best collimator set(s))

ang res		0.085	0.070	0.065	0.058	0.062	0.080	0.083	0.087	0.088	0.075	0.092	0.093	0.095
coll sets		1.1, 0.9 mm	1.1, 0.5 mm	0.5, 1.1 mm	0.5, 0.9 mm	0.5, 1.0 mm	0.5, 1.5 mm	0.9, 1.1 mm	1.0, 1.1 mm	1.2, 0.9 mm	1.2, 0.5 mm	1.0, 1.2 mm	1.2, 1.0 mm	1.1, 1.2 mm
	expected	set1	set2	set3	set4	set5	set6	set7	set8	set9	set10	set11	set12	set13
caffeine	4	3	2	3	2	2	3	2	3	2	3	2	2	3
soda	6	4	5	4	6	2	1	2	3	4	4	4	5	4
anadin	7	3	3	2	3	3	3	3	3	4	3	3	3	3
seasalt	2	2	1	1	1	2	1	1	1	1	1	1	2	1
greentea	4	1	2	1	2	2	1	1	2	1	3	1	1	1
hayfever	3	1	2	1	2	2	2	1	1	1	1	1	1	1
paracetamol	4+4	3	3	2	4	4	3	4	2	4	1	1	2	4
ibuprofen	4	1	2	4	1	3	1	1	1	1	2	1	1	1
tesco multi	6	1	2	1	1	1	1	1	1	1	1	1	1	1
pmma	6	2 + multi-pe	3 + multi-pe	2 + multi-pe	3+	3+	3+	3-4+	1+	1-2+	4+	3-4+	5+	5+
pe	4+6	1	1	1	1	1	1	1	1	1	1	1	1	1
ptfe	1+3	2	2	2	2	2	2	2	2	2	2	2	2	1
pp	6	1	1	1	1	1	1	1	1	1	1	1	1	1
pvc	10	2	3	3	3	3	3	3	3	3	3	3	3	3
ps	9	3	4	3	3	3	2	3	3	3	3	7	7	3
caster sugar	1+3	1+2	1+1	1+0	1+3	1+3	1+4	1+4	1+3	2+2	1+2	1+3	1+0	2+1
dem sugar	1+2	1+1	1+3	1	multi	1	1+3	1+1	1+2	1+2	1	1	1+2	1
gran sugar	1+2	1+4	1+multi	1+2	1+2	1+2	1	1+3	1+1	1+2	1+1	1	1+1	1+1
musca sugar	1+4	1+1	1+4	1+multi	1+3	1+2	1+1	1+2	1+1	1	1	1	1+4	1
hermeset	1+multi	1	3	2	2	2	1	1	2	2	2	2	2	1

Table 2.6: Spectral analysis for model predicted spectra for all collimator sets – peak shift (nm⁻¹)

(yellow shade shows about 80-90% agreement between model predicted and measured+JCPDS data)

ang res	0.085	0.070	0.065	0.058	0.062	0.080	0.083	0.087	0.088	0.075	0.092	0.093	0.095
coll sets	1.1, 0.9 mm	1.1, 0.5 mm	0.5, 1.1 mm	0.5, 0.9 mm	0.5, 1.0 mm	0.5, 1.5 mm	0.9, 1.1 mm	1.0, 1.1 mm	1.2, 0.9 mm	1.2, 0.5 mm	1.0, 1.2 mm	1.2, 1.0 mm	1.1, 1.2 mm
	set1	set2	set3	set4	set5	set6	set7	set8	set9	set10	set11	set12	set13
caffeine	-0.123	-0.305	-0.178	-0.120	-0.260	-0.115	-0.320	-0.308	-0.313	0.023	-0.313	-0.305	-0.583
soda	-0.217	-0.263	-0.350	0.158	-0.812	-0.537	-0.815	-0.592	-0.313	-0.040	-0.435	-0.283	-0.353
anadin	-0.677	-0.673	-0.839	-0.673	-0.700	-0.700	-0.696	-0.687	-0.614	-0.687	-0.677	-0.681	-0.687
seasalt	-0.610	-1.390	-1.390	-1.465	-0.155	-1.435	-1.435	-1.310	-1.405	-1.495	-1.390	-0.400	-1.480
greentea	-0.655	-0.565	-0.663	-0.313	-0.670	-0.670	-0.398	-0.585	-0.473	-0.328	-0.663	-0.670	-0.670
hayfever	-0.593	-0.370	-0.583	-0.240	-0.593	-0.423	-0.623	-0.613	-0.613	-0.583	-0.603	-0.613	-0.603
paracetamol	-0.350	-0.183	-0.563	-0.158	-0.250	-0.373	-0.265	-0.348	-0.143	-0.813	-0.813	-0.560	-0.008
ibuprofen	-0.700	-0.595	-0.048	-0.678	-0.403	-0.685	-0.693	-0.700	-0.510	-0.678	-0.685	-0.670	-0.700
tesco multi	-0.305	-0.125	-0.095	-0.320	-0.365	-0.380	-0.365	-0.335	-0.275	-0.260	-0.320	-0.275	-0.305
pmma	-0.015	-0.105	0.008	-0.037	-0.027	-0.255	-0.100	-0.062	-0.030	-0.012	-0.037	-0.042	-0.047
pe	-0.180	-0.150	-0.168	-0.151	-0.174	-0.177	-0.176	-0.161	-0.154	-0.178	-0.181	-0.179	-0.220
ptfe	-0.112	-0.109	-0.106	-0.113	-0.113	-0.114	-0.112	-0.113	-0.116	-0.111	-0.111	-0.141	-0.144
pp	-0.140	-0.140	-0.152	-0.164	-0.152	-0.176	-0.176	-0.128	-0.176	-0.164	-0.176	-0.128	-0.164
pvc	-0.179	-0.161	-0.161	-0.161	-0.161	-0.161	-0.161	-0.162	-0.162	-0.163	-0.160	-0.161	-0.160
ps	-0.099	-0.098	-0.098	-0.093	-0.098	-0.104	-0.099	-0.099	-0.125	-0.175	-0.245	-0.389	-0.288
hermeset	0.750	-0.040	0.480	0.420	0.420	0.790	0.880	0.450	0.420	0.450	0.450	0.480	0.790
caster sugar	not applicable												
dem sugar	not applicable												
gran sugar	not applicable												
musca sugar	not applicable												
avg	-0.263	-0.330	-0.307	-0.257	-0.282	-0.345	-0.347	-0.359	-0.313	-0.326	-0.397	-0.314	-0.351

Table 2.7: Spectral analysis for model predicted spectra for all collimator sets – peak width (FWHM) (nm^{-1})

(yellow shade shows about 80-90% agreement between model predicted and measured+JCPDS data)

ang res	0.085	0.070	0.065	0.058	0.062	0.080	0.083	0.087	0.088	0.075	0.092	0.093	0.095
coll sets	..1, 0.9 mm\1, 0.5 mm\0.5, 1.1 mm\0.5, 0.9 mm\0.5, 1.0 mm\0.5, 1.5 mm\0.9, 1.1 mm\0, 1.1 mm\0.2, 0.9 mm\0.2, 0.5 mm\0, 1.2 mm\0.2, 1.0 mm\0.1, 1.2 mm\0.1												
	set1	set2	set3	set4	set5	set6	set7	set8	set9	set10	set11	set12	set13
caffeine	0.125	0.093	0.108	0.088	0.088	0.110	0.110	0.095	0.118	0.118	0.133	0.148	0.133
soda	0.060	0.127	0.060	0.108	0.057	0.060	0.067	0.055	0.060	0.042	0.055	0.117	0.078
anadin	0.121	0.117	0.043	0.104	0.104	0.133	0.120	0.129	0.136	0.121	0.117	0.121	0.131
seasalt	0.125	0.290	0.000	0.135	0.000	0.000	0.000	0.000	0.000	0.000	0.230	0.120	0.000
greentea	0.168	0.160	0.115	0.230	0.093	0.153	0.145	0.115	0.138	0.100	0.123	0.130	0.100
hayfever	0.123	0.113	0.113	0.123	0.077	0.180	0.133	0.113	0.100	0.093	0.133	0.123	0.123
paracetamol	0.110	0.040	0.023	0.055	0.080	0.015	0.023	0.023	0.060	0.010	0.000	0.015	0.075
ibuprofen	0.108	0.108	0.138	0.075	0.115	0.108	0.090	0.085	0.130	0.120	0.115	0.098	0.115
tesco multiv	0.320	0.030	0.400	0.400	0.400	0.400	0.400	0.400	0.400	0.400	0.400	0.400	0.400
pmma	0.520	0.520	0.520	0.520	0.490	0.490	0.450	0.450	0.600	0.560	0.490	0.490	0.490
pe	0.280	0.250	0.250	0.210	0.240	0.300	0.270	0.310	0.270	0.250	0.310	0.340	0.300
ptfe	0.340	0.250	0.370	0.310	0.340	0.340	1.060	0.340	0.280	0.250	0.340	0.370	0.340
pp	0.520	0.480	0.520	0.450	0.520	0.490	0.480	0.480	0.490	0.480	0.520	0.550	0.510
pvc	0.003	0.013	0.013	0.016	0.013	0.016	0.013	0.013	0.013	0.013	0.010	0.013	0.013
ps	0.060	0.034	0.053	0.037	0.041	0.053	0.050	0.060	0.063	0.063	0.003	0.007	0.067
caster sugar	0.100	0.100	0.100	0.100	0.100	0.100	0.100	0.100	0.100	0.100	0.100	0.100	0.100
dem sugar	0.350	0.600	0.300	0.090	0.090	0.600	0.090	0.350	0.350	0.350	0.600	0.600	0.600
gran sugar	0.030	0.030	0.030	0.030	0.030	0.030	0.030	0.030	0.030	0.030	0.030	0.030	0.030
musca sugar	0.030	0.030	0.030	0.030	0.030	0.030	0.030	0.030	0.030	0.030	0.030	0.030	0.030
hermesetas	0.580	0.580	0.580	0.580	0.580	0.580	0.580	0.580	0.580	0.580	0.580	0.580	0.580
avg	0.200	0.200	0.190	0.180	0.170	0.210	0.210	0.190	0.200	0.190	0.220	0.220	0.210

From Tables 2.5, 2.6 and 2.7 we can see that there is variability with respect to number of peaks, peak position and peak width as compared to that in the expected spectrum. The range of peak shift is $0.25\text{-}0.39 \text{ nm}^{-1}$. The peak widths are about 0.20 nm^{-1} with least being 0.17 nm^{-1} obtained for set4 (0.5, 0.9) mm. Averaging these parameters for all samples can give us some idea about the robustness of the model but since the samples chosen have variability in their characteristic spectra with respect to number of peaks and their positions, we can group them to study the efficiency of the model. For instance sugars produced greater peak shifts but narrower peaks. Due to their spectra containing multi-peaks the measured data was not justifiable for comparison and hence it was not easy to estimate the level up to which the model could predict for this set of samples. This could be due to the granular nature of these samples due to which in

the measured data peaks appeared shifted on repeating the experiments and the data was not consistent. Considering the plastics, on the whole, main peaks of the characteristic profile were successfully predicted by the model with peak shifts about 0.15 nm^{-1} and peak width in the range $0.03\text{-}0.50 \text{ nm}^{-1}$. The pharmaceutical drug caffeine showed a quite resolved spectrum across collimator sizes with main peaks seen with all sets, peak shifts of about 0.20 nm^{-1} (and peak widths of 0.08 nm^{-1}) for collimators with high angular resolution and maximum peak shift being 0.58 nm^{-1} (maximum peak width of 0.15 nm^{-1}) seen with the collimator sets offering low angular resolution.

From Tables 2.5, 2.6 and 2.7 we can see that collimator sets 1, 4 and 5 produced more resolved spectra for all the samples considered with peak shift of 0.26 nm^{-1} and peak width of 0.175 nm^{-1} . However, to optimise the system geometry a more quantitative analysis technique is required to select predicted spectra that are as close as possible to the JCPDS with respect to position and intensity of peaks. The analysis would also optimise the kV_p value and the scatter angle used in the system. This is explained in the following section.

2.7 Optimisation of system geometry

The breast tissue characterisation is based on difference in the spectral peak positions and intensities, the peaks corresponding to adipose and glandular tissues of the breast appearing at 1.1 nm^{-1} and 1.6 nm^{-1} respectively. Hence samples used for the model were selected based on their momentum transfer range (i.e. $0.5\text{--}3.0 \text{ nm}^{-1}$) in the diffraction spectra. This range was optimal for the work as it covered the average photon energy range provided by $10\text{--}110 \text{ kV}_p$ value applied on the X-ray tube at scatter angular range of $4\text{--}8$ degree. For system optimization, five kV_p values were chosen namely, 40, 50, 60, 70 and 80 and five scatter angle values (in degree) namely, 4, 5, 6, 7 and 8 that provided photon energies corresponding to momentum transfer range $0.5\text{--}3.0 \text{ nm}^{-1}$. From the previous sample set eight samples were selected that included plastics and pharmaceutical drugs based on the momentum transfer values of the peak positions and number of peaks in their characteristic (JCPDS) spectra. These samples have been tabulated in Table 2.8.

Table 2.8: Sample set used for system optimisation	
No.	Sample
1	Polystyrene (PS)
2	Polyvinyl chloride (PVC)
3	Polymethylmethacrylate (PMMA)
4	Polytetrafluoroethylene (PTFE)
5	Polypropylene (PP)
6	Polyethylene (PE)
7	Paracetamol
8	Caffeine

In order to optimize the EDXRD system geometry the code was run for all the eight samples for different combinations of tube potential, scatter angle and collimator widths as given in Table 2.9. Therefore, for one sample there were 325 spectra predicted and in total for eight samples 2600 spectra. This was done by writing another piece of code wherein routines were used to call a procedure for a different set of input values.

Table 2.9: Parameter sets for system geometry optimisation				
kV _p value (kV)	Scatter Angle (degree)	Collimator set no.	Source Collimator width (mm)	Detector Collimator width (mm)
40, 50, 60, 70, 80	4, 5, 6, 7, 8	Set 1	1.1	0.9
40, 50, 60, 70, 80	4, 5, 6, 7, 8	Set 2	1.1	0.5
40, 50, 60, 70, 80	4, 5, 6, 7, 8	Set 3	0.5	1.1
40, 50, 60, 70, 80	4, 5, 6, 7, 8	Set 4	0.5	0.9
40, 50, 60, 70, 80	4, 5, 6, 7, 8	Set 5	0.5	1.0
40, 50, 60, 70, 80	4, 5, 6, 7, 8	Set 6	0.5	1.5
40, 50, 60, 70, 80	4, 5, 6, 7, 8	Set 7	0.9	1.1
40, 50, 60, 70, 80	4, 5, 6, 7, 8	Set 8	1.0	1.1
40, 50, 60, 70, 80	4, 5, 6, 7, 8	Set 9	1.2	0.9
40, 50, 60, 70, 80	4, 5, 6, 7, 8	Set 10	1.2	0.5
40, 50, 60, 70, 80	4, 5, 6, 7, 8	Set 11	1.0	1.2
40, 50, 60, 70, 80	4, 5, 6, 7, 8	Set 12	1.2	1.0
40, 50, 60, 70, 80	4, 5, 6, 7, 8	Set 13	1.1	1.2

2.7.1 Multivariate analysis:

The spectra obtained from model predictions were used further for a multivariate partial least squares (PLS) regression. The software used to perform this analysis was The Unscrambler R (Unscrambler v10.1 (2010), Camo, Norway). This method finds the principle components of sets of known data using which predicts the response from unknown data sets [Marten and Naes 1991]. The PLS regression technique establishes a linear relationship between a multi-dimensional matrix of predictors (X) and responses (Y) using a regression model of the form

$$Y = XB + C$$

where Y is a set of target variables to be quantified, for example sample concentration, X is a set of many variables (the counts in each detector channel from the measured diffraction profile of a sample), B a regression coefficient matrix and C is a matrix of residuals i.e. the data that cannot be explained by the model.

Using calibration, the regression coefficients B are determined where known X and Y data are used to build a mathematical regression model. The X matrix in this calibration set used 512 variables, one corresponding to each energy channel. Using each of the x variables in the model would make it extremely complex, inaccurate and would require long computational processing time. Therefore, the x-variables are reduced to their principle components (PCs), where each PC is linearly related to the x-variables. These Principle components are new variables

that describe the main difference between objects or samples here. The first Principle Component describes the greatest variation between objects. The second Principle Component describes the next greatest variation and so on. Having a large number of PCs begin to describe only noise and that could be a cause of inaccurate predictions. Therefore, a suitable number of PCs is selected by picking the number that produces the first local minimum in the residual variance. By doing so, the data is well explained and the noise is omitted.

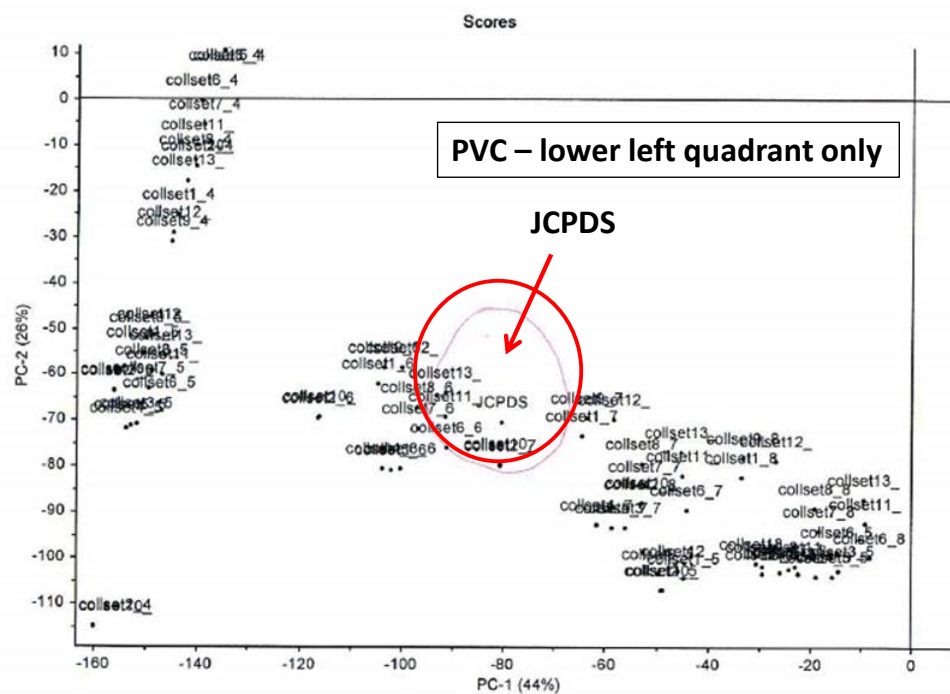
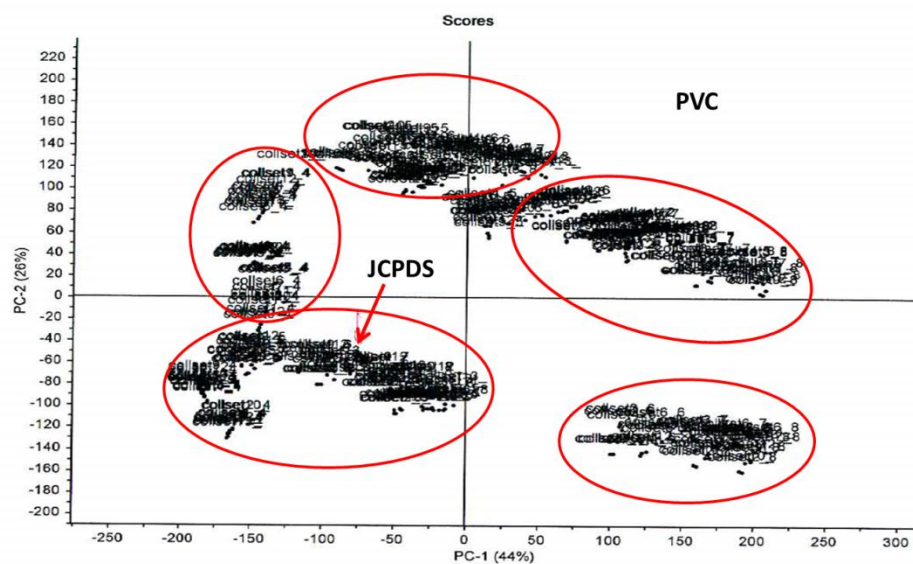
2.7.2: PCA analysis output – scores plot

The PCA analysis produces the following types of plots that can be interpreted as given below:

1. Residual variance gives the error measures and tells how different the samples are from their modelled behaviour.
2. Scores plot are plots of values of each sample projected on the plane of the PCs. Samples that are close are similar here. These are useful to examine groups in the data seeing how different variables affect the PCs. Also from the outliers one can get to know about the samples that are hugely different from the rest of the group.
3. Loadings give the relationship between variables.
4. Influence parameter helps in identifying the outliers.

In this work the Y matrix was the geometrical combination sets. For instance the model was built with model predicted diffraction spectra of PMMA sample for all combinations of kV_p , scatter angle and the collimator sets 1-13. The JCPDS data set of X and Y was used as the training set for calibration. As described by Marten and Naes (1991) the PCA is used to extract information from the X matrix that is related to Y for a maximal covariance between X and Y. The software is then used to run PCA analysis on the sample sets. For the purpose of system optimisation the scores plots were most relevant and have been presented here in Figure 2.13 for all the samples.

Figure 2.13a: Scores plot for PVC



[illegible]

Figure 2.13c: Scores plot for PP

The plot displays PC-1 (44%) on the x-axis and PC-2 (18%) on the y-axis. The 'PP' cluster is located in the upper right quadrant, while the 'JCPDS' cluster is in the lower right quadrant. A red circle highlights 'collset1204' in the JCPDS region, with a red arrow pointing to it from the lower left.

Figure 2.13d: Scores plot for PMMA

The plot displays PC-1 (47%) on the x-axis and PC-2 (24%) on the y-axis. Data points are labeled with 'collset' followed by a number and a subscript (e.g., collset6_8, collset6_5, collset6_4, collset9_8, collset7_6, collset10_8, collset10_6, collset10_4, collset10_3, collset10_2, collset10_1, collset10_0, collset10_4, collset10_3, collset10_2, collset10_1, collset10_0, collset10_4, collset10_3, collset10_2, collset10_1, collset10_0). A red circle highlights a cluster of points labeled 'JCPDS' with a red arrow pointing to it.

Figure 2.13e: Scores plot for PTFE

A PCA scores plot for PTFE. The x-axis is PC-1 (39%) ranging from -150 to 200. The y-axis is PC-2 (29%) ranging from -200 to 150. The plot shows several clusters of data points. A red circle highlights a single point labeled 'JCPDS' at approximately (-55, 15). A red arrow points from the text 'JCPDS' in the lower right quadrant to this circled point. Other labels include 'PTFE' in the upper right, 'collset1' through 'collset14' in the lower right, and 'collset1' through 'collset14' in the upper left. The label 'JCPDS' also appears in the lower right quadrant.

Figure 2.13f: Scores plot for Caffeine

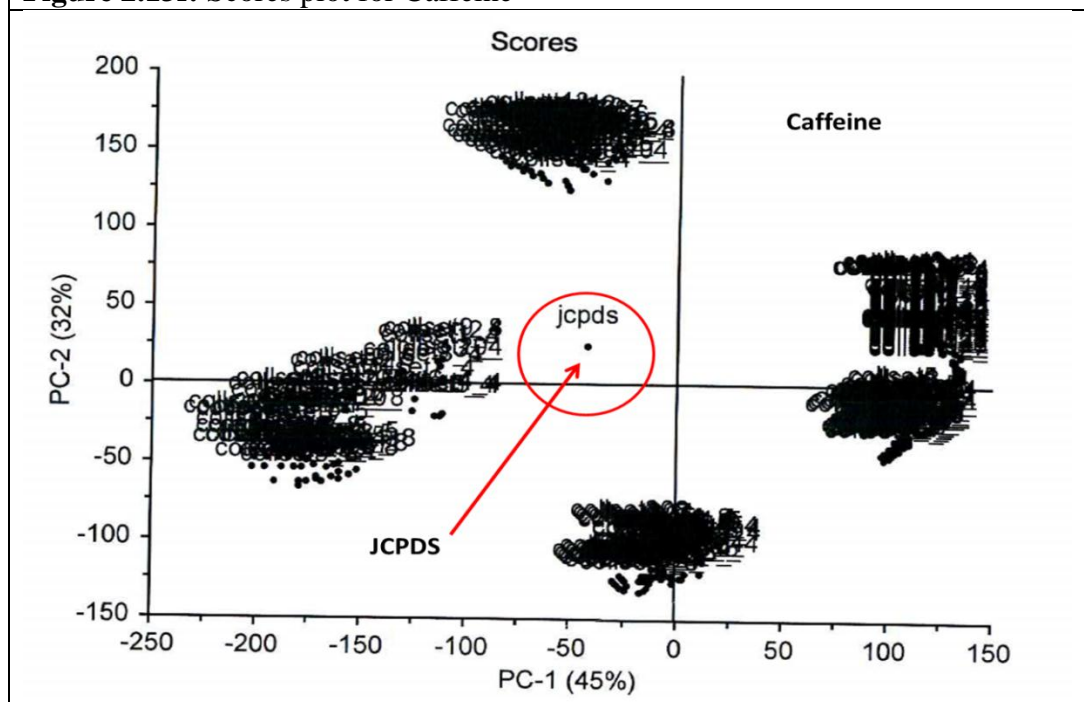


Figure 2.13g: Scores plot for Paracetamol

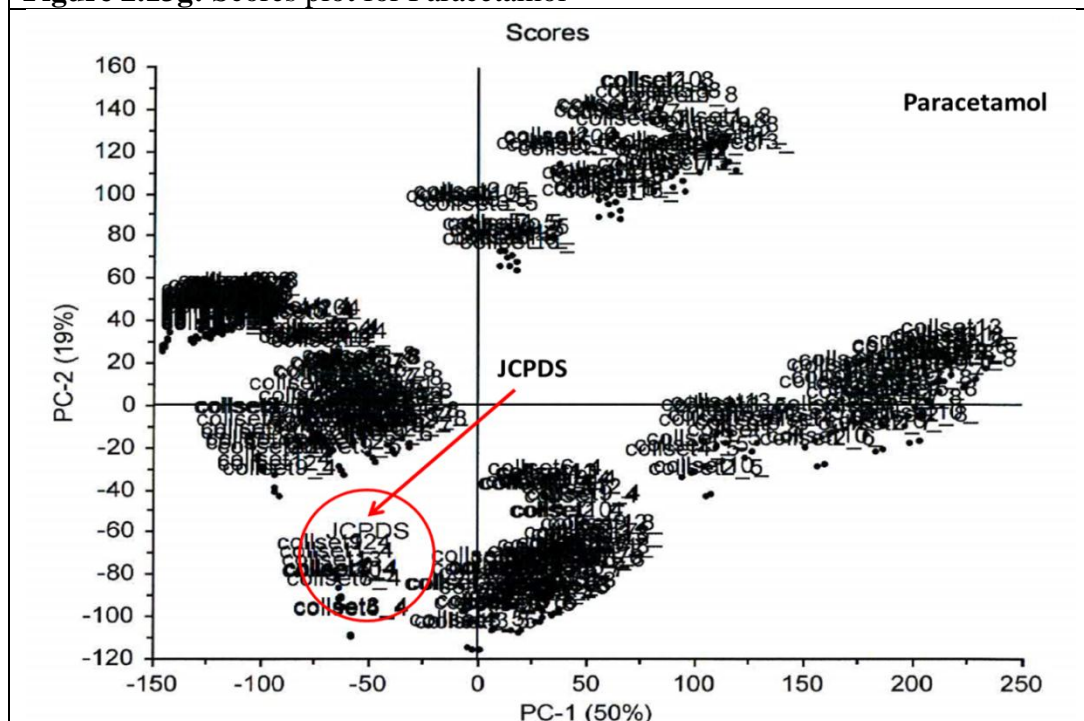
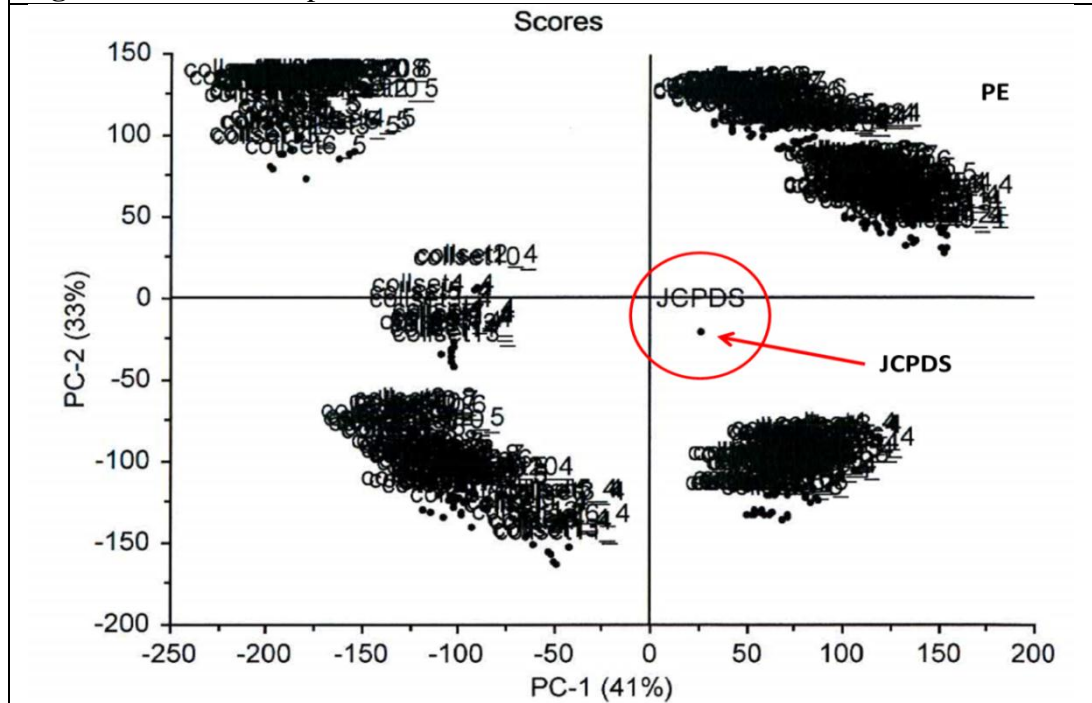


Figure 2.13h: Scores plot for PE



It was observed from the scores plot shown in Figure 2.13 that the score point corresponding to the JCPDS spectrum stood out from the rest of the group as expected. This point has been circled in red and pointed out by a red arrow. Score points corresponding to collimator sets that gave similar angular resolution values were found clustered together as also seen with points corresponding to similar photon energies (kV_p values). These clusters have been marked in red for PVC as shown in Figure 2.13a.

A rank chart was prepared based on top 20 points closest to the JCPDS score. A frequency analysis was performed to obtain the most common set across all

samples. The chart was then reduced to 10 sets and the following sets were obtained to be the most optimum:

Table 2.10: System Geometry Optimisation based on Model Predictions				
kV _p value (kV)	Scatter Angle (degree)	Collimator set no.	Source Collimator width (mm)	Detector Collimator width (mm)
40	6	4	0.5	0.9
		2	1.1	0.5
		10	1.2	0.5
For kV _p ≥ 60				
60	6	2	1.1	0.5

The PCA analysis of the model predicted spectra resulted in 40 kV to be the optimal tube potential with 6 degree scatter angle for three sets of collimators – set 2, 4 and 10 (Table 2.10). The analysis was customized to include kV_p values higher than 60 and found 6 degree with collimator set 2 as the optimal one. Since the collimator set 2 is similar to set 10 with only 0.1 mm difference in the size of source collimator, the set 10 was discarded and Table 2.10 was updated to Table 2.11 as follows:

Table 2.11: Revised - System Geometry Optimisation based on Model Predictions				
kV _p value (kV)	Scatter Angle (degree)	Collimator set no.	Source Collimator width (mm)	Detector Collimator width (mm)
40	6	4	0.5	0.9
40, 60	6	2	1.1	0.5

Using the above optimal geometrical settings an EDXRD system has been set up and materials have been characterised. This has been detailed in the following chapter.

Chapter 3

Material Characterisation using Optimised EDXRD System

The energy dispersive X-ray diffraction (EDXRD) system employs a collimated polychromatic X-ray source and a collimated energy-resolving detector, placed at a specific angle to the incident beam. In this kind of arrangement, the incoming photons of different energies interact with the material (electrons of atoms) of the sample and scatter depending on the momentum transferred to them by the electrons and get detected by the detector, exhibiting Bragg diffraction.

This chapter will detail the setting up of EDXRD system using geometry optimized previously based on model predictions and materials will be characterised to build a database of diffraction data.

Chapter 2 detailed the development of model for EDXRD system, its predictions and optimization of geometrical parameters of the system. According to this optimization, a 40 kV_p tube potential was predicted to be optimal for a scatter angle of 6 degree for collimator set 4 i.e. (source collimator, detector collimator) widths (mm) being (0.5,0.9). The other optimal geometric sets are collimator sizes (1.1,0.5) mm at 6 degree scatter angle at 40 and 60 kV_p as tabulated in Table 3.1. For the purpose of referencing these optimized sets we name them as sets 1, 2 and 3 (Table 3.1), not to be confused with collimator sets used earlier.

Table 3.1: Sets - System Geometry Optimisation based on Model Predictions					
Optimised geometry set no.	kV _p value (kV)	Scatter Angle (degree)	Collimator set no.	Source Collimator width (mm)	Detector Collimator width (mm)
1	40	6	4	0.5	0.9
2	40	6	2	1.1	0.5
3	60	6	2	1.1	0.5

3.1 EDXRD system design

An EDXRD system has been set up (Figure 3.1) in order to characterize materials according to the optimised geometric parameters obtained from model predicted spectra.

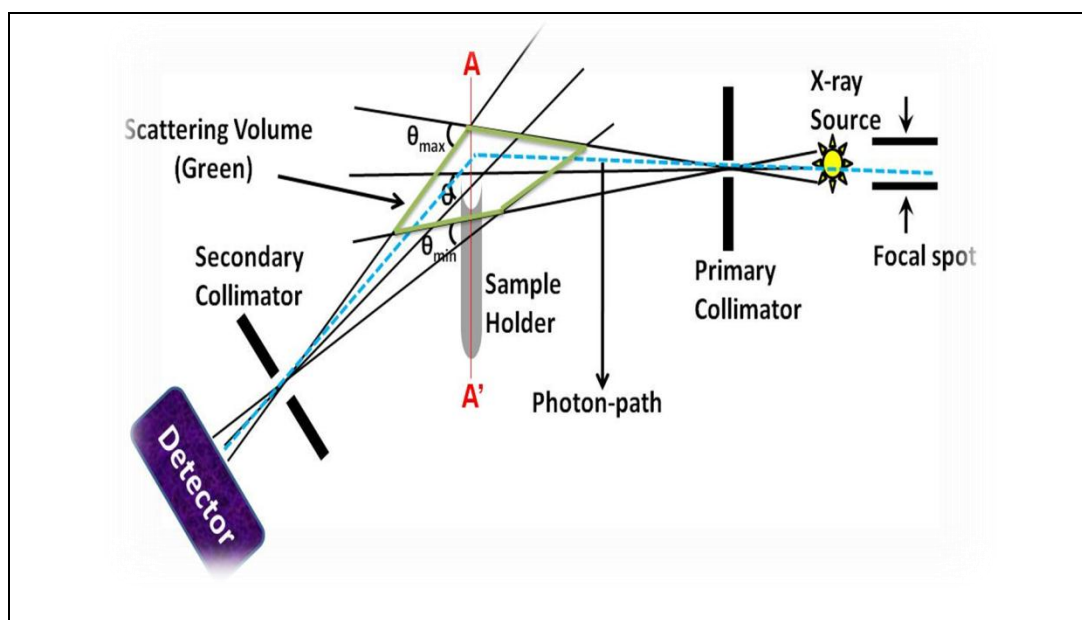
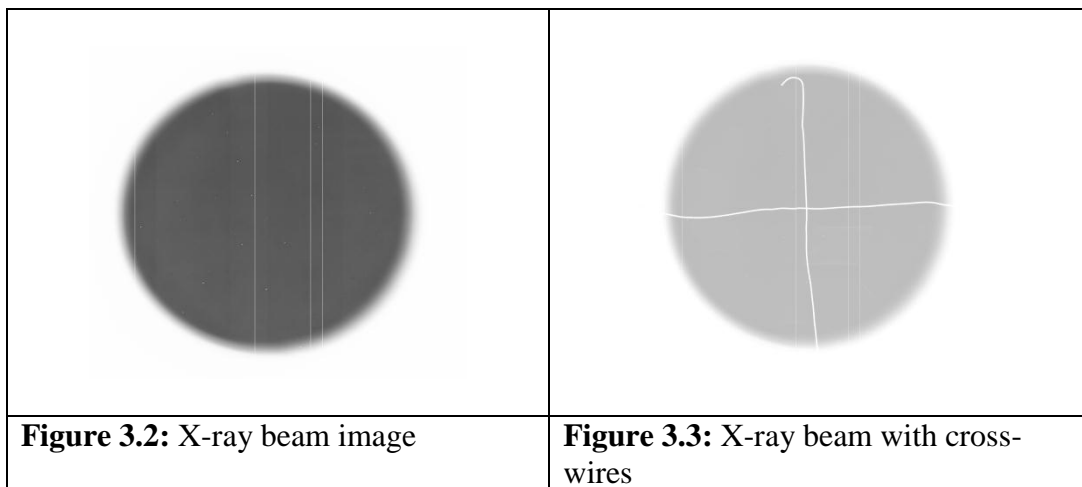


Figure 3.1: A schematic diagram showing EDXRD system set up



For this purpose the components of EDXRD system were set up as follows:

3.1.1 X-ray Source

A Tungsten (W, $Z=74$) target industrial X-ray tube (AGO installations, Philips), with Aluminium filter (nominal thickness 2 mm) was used as the polychromatic X-ray source. This produced a maximum output potential of 110 kV and 30 mA. The source was first aligned parallel to the optical bench using a flat panel pixelated detector called DPix (2304 x 3200 pixels) placed at about 2 m from the X-ray source and at a height that could cover the whole beam. The images were collected using software ViVA (Varian Medical Systems, Inc., CA, USA). The detector was calibrated first and then an image was taken with X-rays on. The centre of the circular beam was located using a code written in IDL. A set of cross wires were stuck on the detector and their intersection was used to mark the position of the centre of the beam on its image as shown in Figures 3.2 and 3.3.



The source collimator was first placed as close as possible to the X-ray source aperture. The source collimator is mounted on a set of translation stages that allow X-Y movement and also Z-axis adjustment up to half a micron. An initial alignment was obtained using lasers. By translating the source collimator in small steps across (500 micron) the source aperture images were taken and the centre of the collimator was made to coincide with that of the beam. The image is shown in Figure 3.4. Now, the detector collimator was placed behind the source collimator leaving just enough gap of the size of an average breast i.e. 4.5 cm. The detector collimator is mounted on a set of translation stages that allow X-Y movement and also Z-axis adjustment up to half a micron. This arrangement also included a rotary stage (upto 1° of a degree) that will be used later to set the scatter angle. An initial alignment was obtained using lasers. By translating the detector collimator in small steps (500 micron) across the source collimator images were taken and the centre of the collimator was made to coincide with that of the centre of the source collimator and therefore the source aperture. The image is shown in Figure 3.5.

	
Figure 3.4: Source collimator alignment with X-ray beam	Figure 3.5: Detector collimator alignment with X-ray beam

3.1.2 Detector and MCA

A high purity germanium (HPGe) detector with a planar crystal of diameter 36 mm and depth 13 mm (model GLP16/95/16PS, EG & G Ortec, Oakridge, TN, USA) was used to detect the scattered photons. This is placed opposite the X-ray source. The diffraction spectra were analysed using an MCA with change sample and sample ready connections (921 EG & G Ortec) whilst the static sample measurements used a computer-based MCA card (TRUMP PCI, EG & G Ortec). A software Maestro, EG & G Ortec was used to assign the detected photons to one of the 512 energy channels. The multi-channel analyzer (MCA) analyses the pulses (amplitude proportional to energy deposited by scattered photons in the detector) that leave the detector.

3.1.3 Detector output

The output of MCA is a spectrum of counts of scattered photons against channels. The channels could be calibrated for photon energy so as to have a count per channel against photon energy spectrum. The system was calibrated using Am-241 radionuclide source (nominal activity: 370 kBq) and the energy resolution of the detector was measured as 0.52 keV at 59.5keV. A software Maestro, EG & G Ortec was used to assign the detected photons to one of the 512 energy channels. The output generated by Maestro is a spectrum in .chn format. By use of IDL code these .chn files are converted to a more readable format like .xls and counts against energy or momentum transfer graphs can be plotted for analysis.

3.1.4 Setting up the scatter angle

An arrangement was made using a metallic strip mounted on a translation stage to be used as the sample holder. Using the stage the strip was positioned in between the two collimators. A sample with known spectrum (for example, Caffeine) was placed on this sample holder in the middle of the source and detector collimator and in line with the beam axis. In order to set the scatter angle to 6 degree, the detector collimator was rotated by 6 degree using the rotary stage. The detector is now placed right at the back of the detector collimator. With X-ray tube operating at 40 kVp, source collimator width set as 0.5 mm and detector collimator width set as 0.9 mm, a spectrum is then recorded. Background counts are recorded with

no sample in the sample holder. This count was then subtracted from the counts obtained with sample placed on the sample holder, so as to correct for the counts due to the background. The peak positions and intensities are compared with the standard JCPDS spectrum. Using the translation stages the detector collimator is adjusted until the two spectra are in agreement where the peaks obtained actually correspond to a scatter angle of 6 degree.

3.2 Characterisation of materials - samples

As explained above, the diffraction system is now aligned and set at 6 degree scatter angle. Since the scatter angle is common to all the optimized geometry sets this is not disturbed until all measurements have been taken. This system is now used to characterize materials that will build a diffraction database which will be further used to generate diffraction images. The following materials have been characterized using this system:

- (1) Plastics and Pharmaceutical drugs
- (2) Breast-equivalent tissues

3.2.1 Plastics and Pharmaceutical drugs

Eight samples including six plastics and two pharmaceutical drugs were selected out of a group of twenty samples for which the JCPDS data was available. Plastics are dense materials that can very well be used as tumour substitutes due to their characteristic diffraction profiles. Caffeine (99% pure) and Paracetamol have also been used as samples for characterisation (Table 3.2).

Table 3.2: Sample set	
No.	Samples
1	Polystyrene (PS)
2	Polyvinyl chloride (PVC)
3	Polymethylmethacrylate (PMMA)
4	Polytetrafluoroethylene (PTFE)
5	Polypropylene (PP)
6	Polyethylene (PE)
7	Caffeine
8	Paracetamol

Plastics were cut to 5 X 50 mm size to be used as samples. Caffeine and Paracetamol in their powder form were filled in Polypropylene straws of 5 X 50 mm size and used as samples.

3.2.2 Breast-equivalent tissues – cuboid breast phantoms

In order to test the potential of EDXRD technique in breast imaging, the optimized geometry was used to measure the diffraction profiles of large samples. For this purpose, breast phantoms were prepared of varying thickness using animal tissues. These phantoms were prepared so as to mimic tumour in breast tissues. Plastics and pharmaceutical drugs placed inside these breast phantoms would mimic a breast tissue. Phantoms were prepared using pig fat and muscle to substitute for human tissues. Slices of fat and muscle tissues of appropriate thickness were arranged vertically to mimic human breast tissue of different thickness. A 1 cm thick phantom was practically not possible as it had to contain 0.5 cm each of fat and muscle tissue that was not easy to cut. Therefore, a 2 cm thick breast phantom was prepared by a slice of 1 cm of fat tissue and a slice of 1 cm of muscle tissue as shown in Figure 3.6. In a similar way, 3 cm (1 cm muscle sandwiched between 1 cm fat either side) and 4 cm (2 cm muscle sandwiched between 1 cm fat either side) breast phantoms were prepared. These tissues were placed carefully in a sample case made out of thin perspex sheets supported by varnished wood as shown in Figure 3.6. The breast phantoms containing breast-equivalent tissue were stored in a freezer at a temperature of -35°C when not in use.

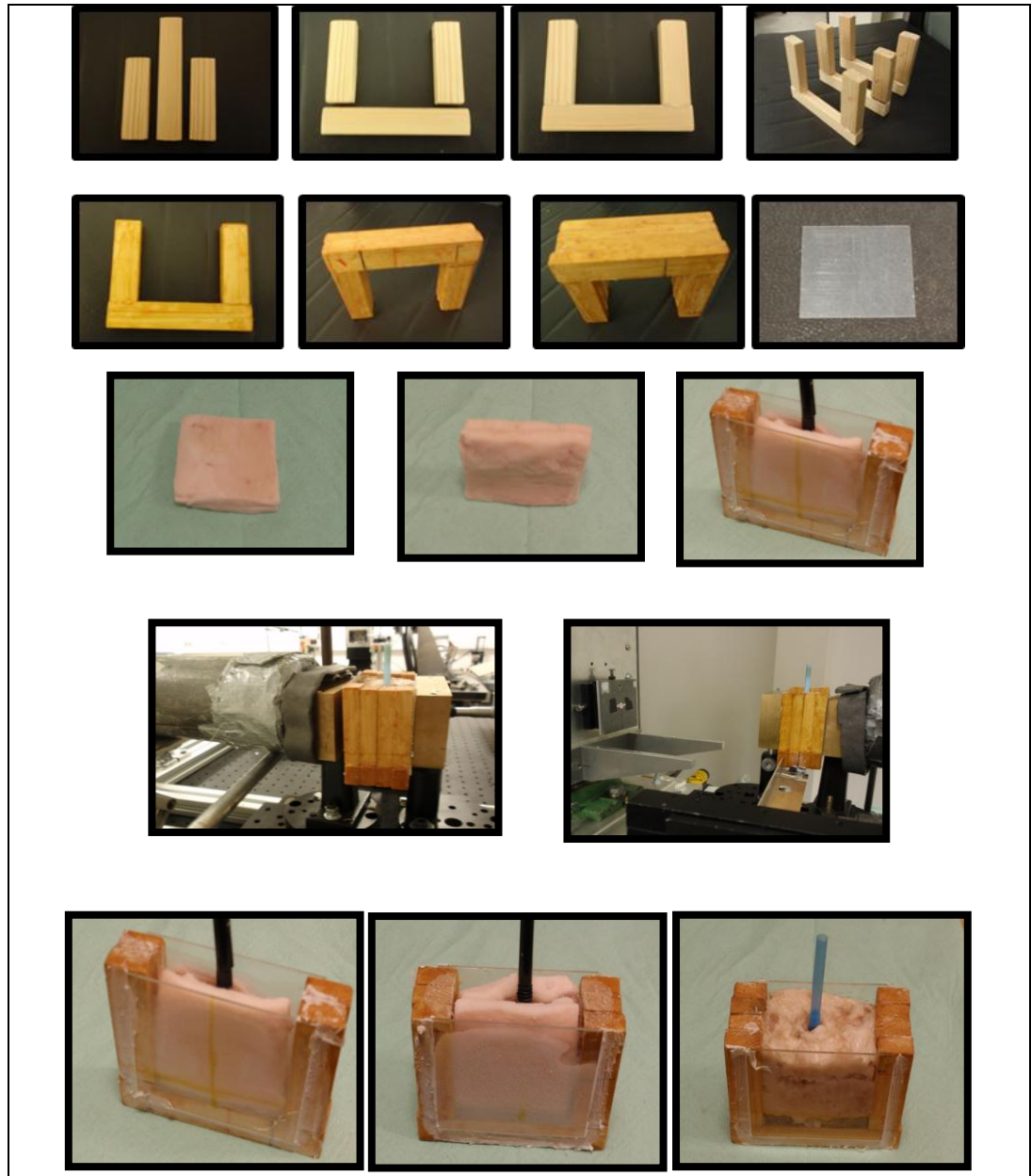


Figure 3.6: Breast phantom preparation – thickness 2 cm, 3 cm and 4 cm

Plastics cut to 5 x 50 mm size or Polypropylene straw (5 x 50 mm) containing powdered pharmaceutical drug was placed in the centre of the phantom. The

phantoms were placed on the sample holder in between the two collimators and spectra were recorded.

3.2.3 Breast-equivalent tissues – triangular breast phantoms

In order to explore the breast thickness, triangular shaped phantoms were prepared using animal muscle tissues and lard. The purpose of these phantoms was to have a diffraction spectrum corresponding to a range of tissue thickness. These diffraction measurements will then be processed further to generate diffraction images as explained in chapter 4.

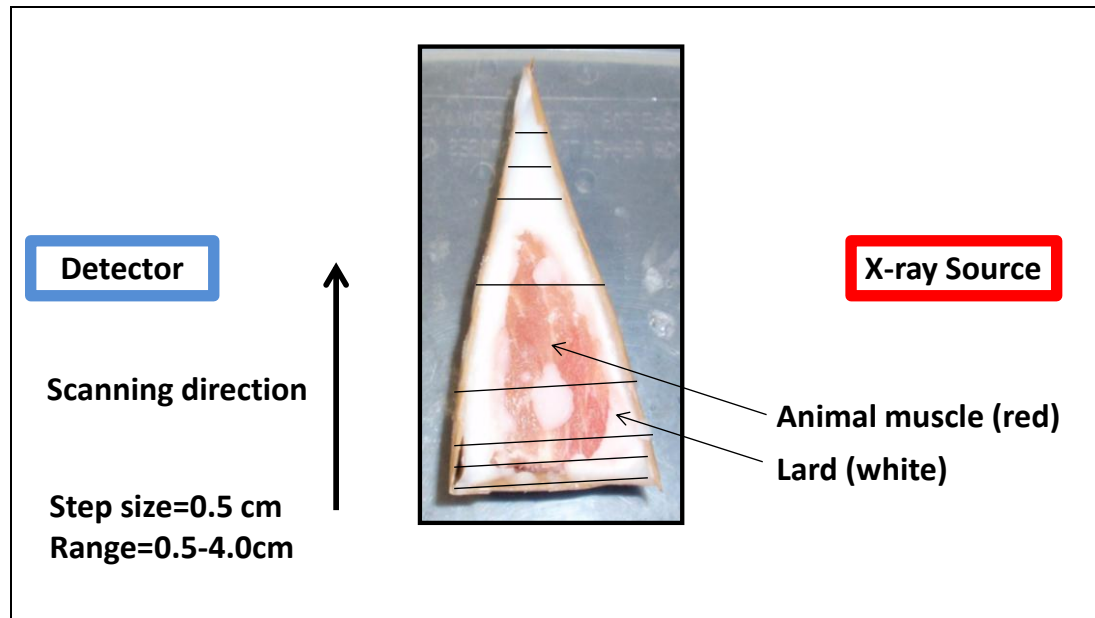
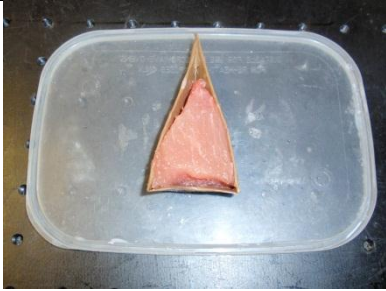
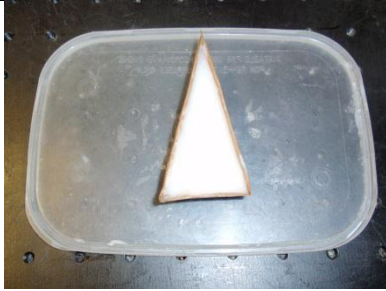
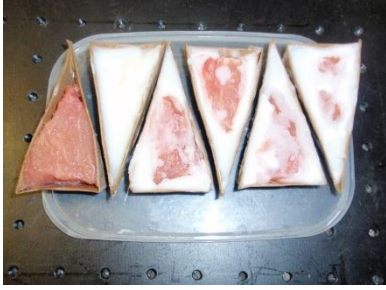



Figure 3.7: Breast phantom – diffraction measurement taken in steps of 0.5 cm

For this purpose, the tissues were placed in cardboard cut in to triangles, stuck together and water proofed with brown tape (Figure 3.7). The base of these triangles was set as 4 cm and the vertical height was set as 6 cm. This was done so

diffraction measurements could be made at different thickness of the tissues. For this purpose, muscle tissue of size 3.5, 3.0, 2.5, 2.0 cm was placed in these triangular cases and the space surrounding the muscle tissue was filled with molten lard. Figures 3.8 show the pictures of the breast phantoms containing different tissue composition. The breast phantoms containing breast-equivalent tissue were stored in a freezer at a temperature of -35°C when not in use.

	
<p>Figure 3.8a: All muscle (M) phantom</p>	<p>Figure 3.8b: All fat/lard (L) phantom</p>
	
<p>Figure 3.8c: Phantoms – All muscle (4.0 M), all fat (4.0 L), 3.5 M 0.5 L, 3.0 M 1.0 L, 2.5 M 1.5 L, 2.0 M 2.0 L (numbers refer to tissue width in cm)</p>	<p>Figure 3.8d: Phantoms with markings - All muscle (4.0 M), all fat (4.0 L), 3.5 M 0.5 L, 3.0 M 1.0 L, 2.5 M 1.5 L, 2.0 M 2.0 L (numbers refer to tissue width in cm)</p>

3.3 Diffraction spectra

Diffraction spectra were recorded for plastics, pharmaceutical drugs and tissues using sets 1, 2 and 3 (recalling Table 3.1) geometries as optimized in chapter 2.

Table 3.1: Sets - System Geometry Optimisation based on Model Predictions					
Optimised geometry set no.	kV _p value (kV)	Scatter Angle (degree)	Collimator set no.	Source Collimator width (mm)	Detector Collimator width (mm)
1	40	6	4	0.5	0.9
2	40	6	2	1.1	0.5
3	60	6	2	1.1	0.5

3.3.1 Spectra for plastics and pharmaceutical drugs

Following are the diffraction spectra recorded at Set 1 i.e., 40 kV for 0.5 mm source collimator and 0.9 mm detector collimator.

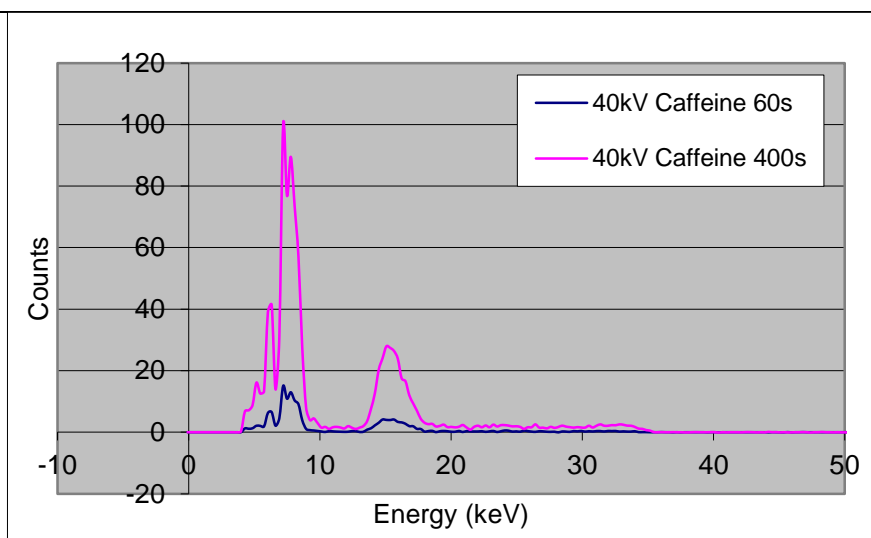


Figure 3.9a: Diffraction spectrum of Caffeine collected at set 1 for 60s and 400s

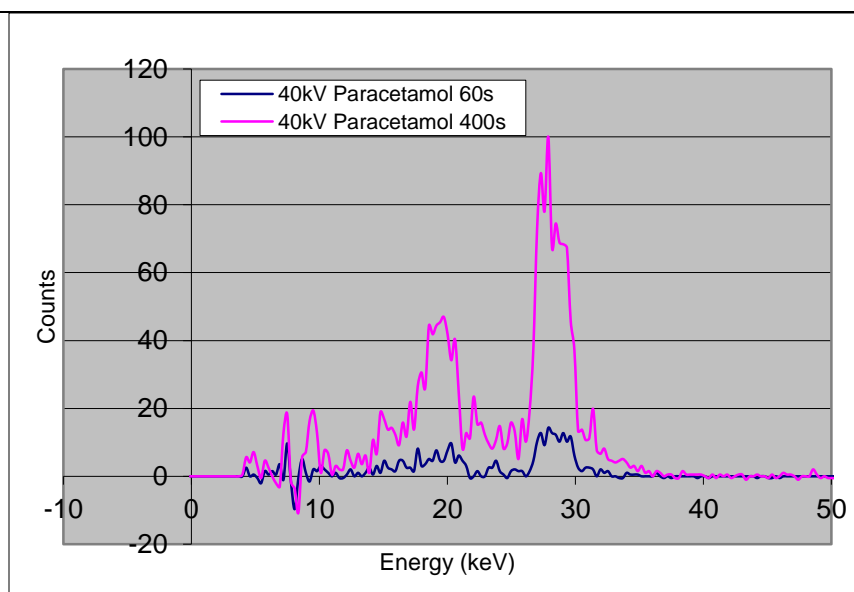


Figure 3.9b: Diffraction spectrum of Paracetamol collected at set 1 for 60s and 400s

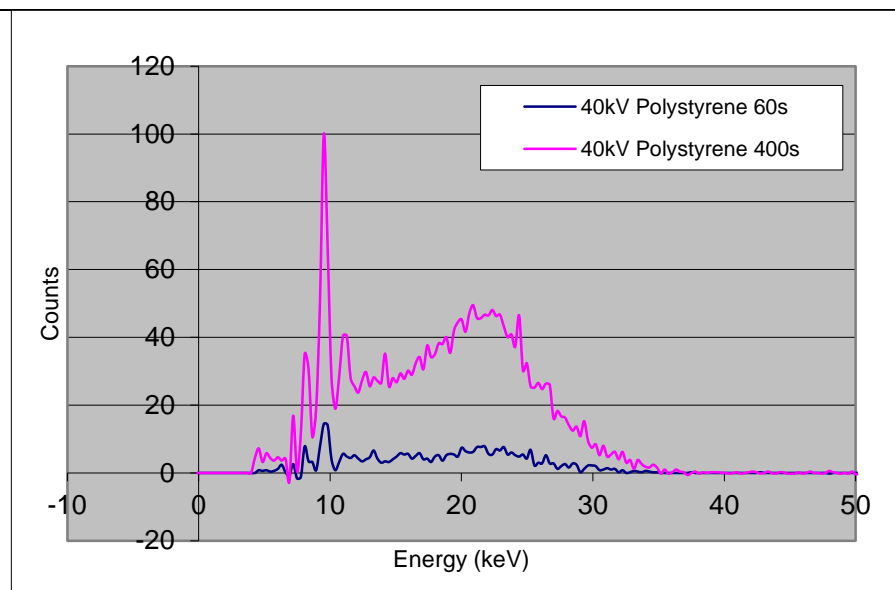


Figure 3.9c: Diffraction spectrum of Polystyrene collected at set 1 for 60s and 400s

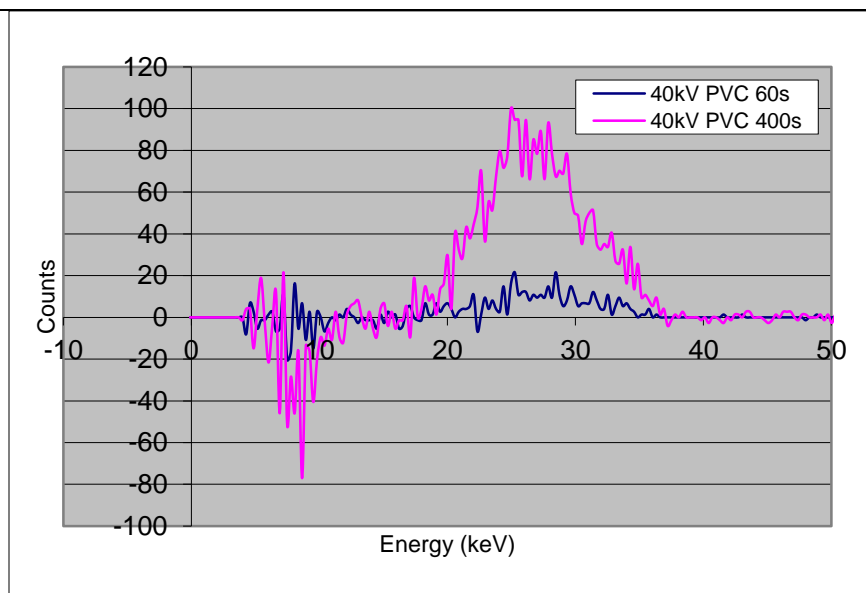
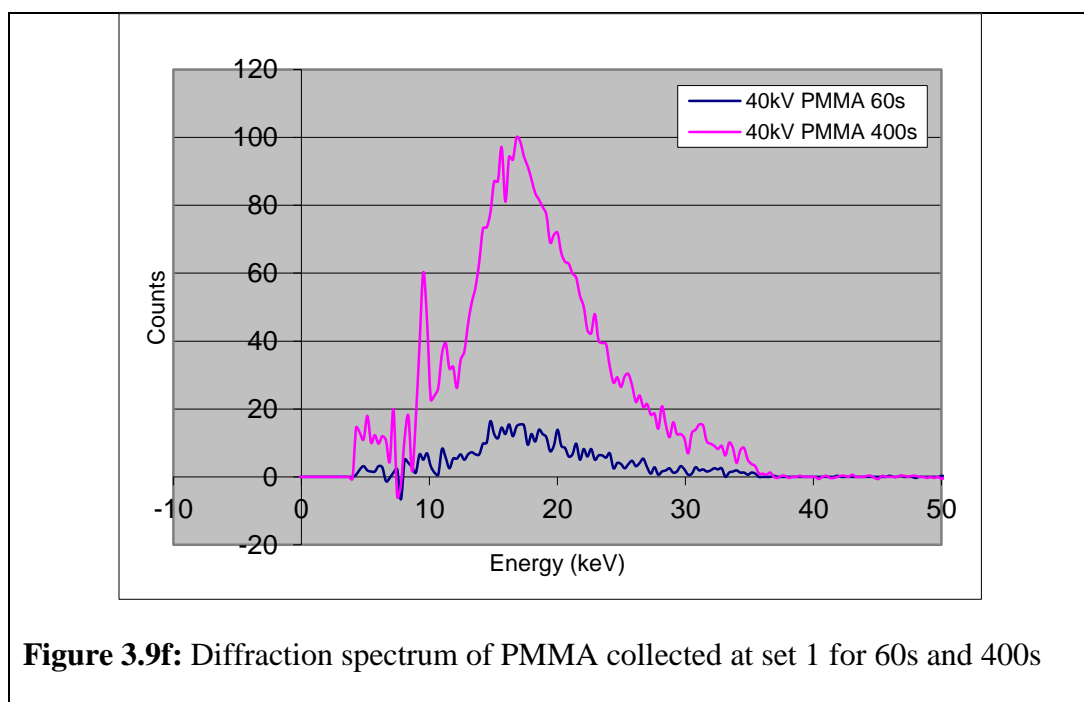
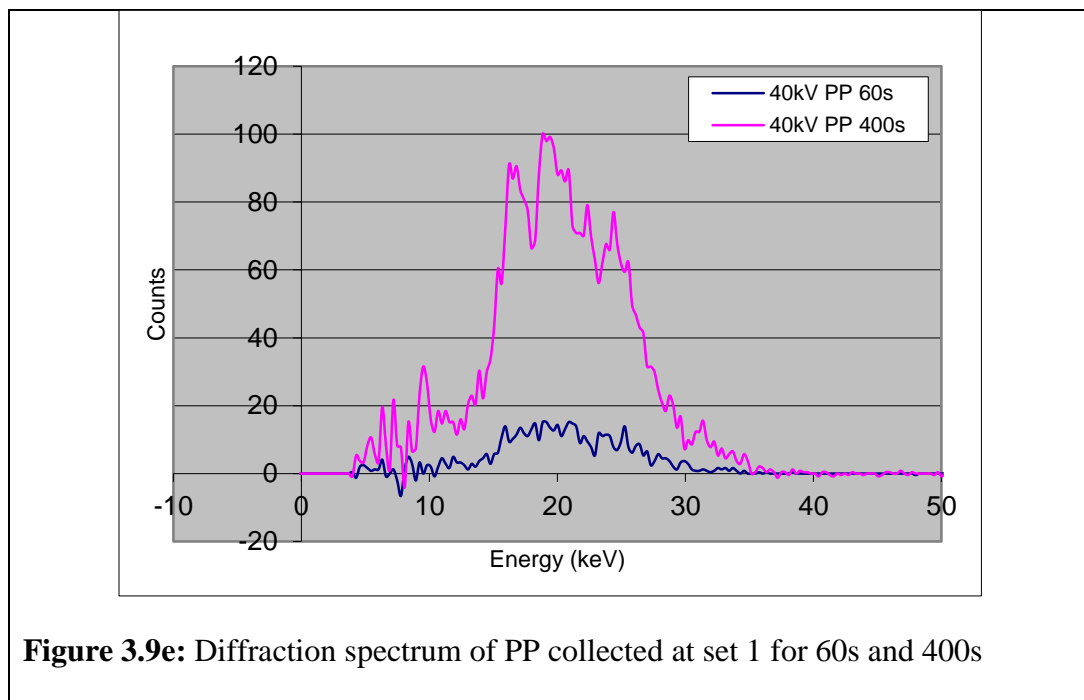
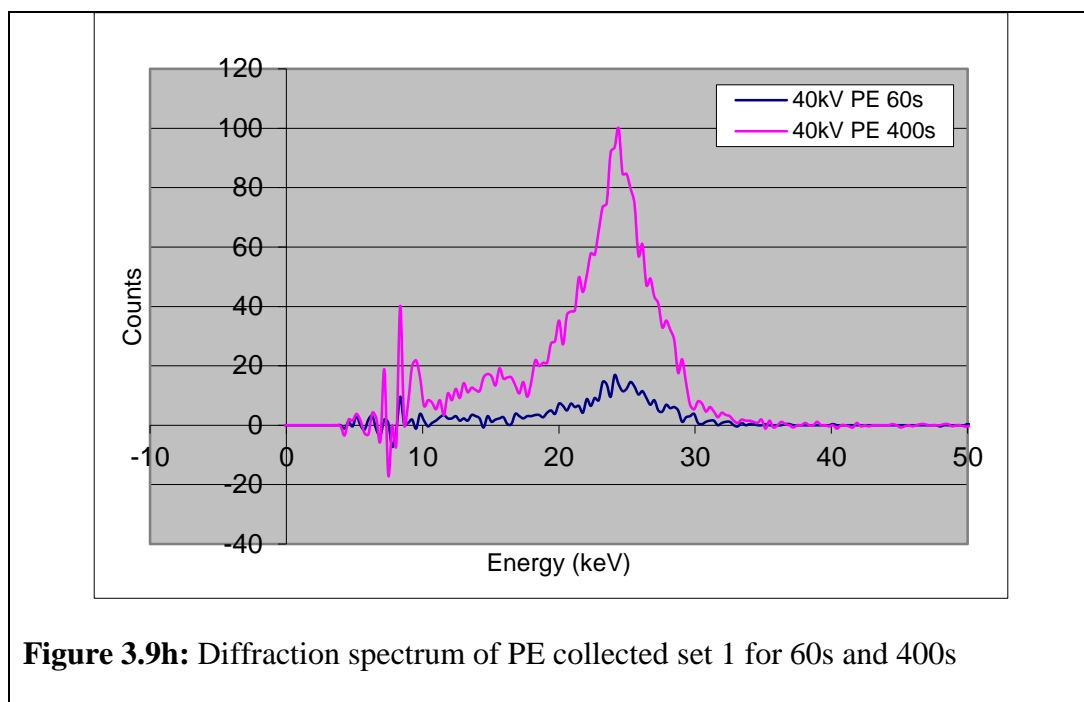
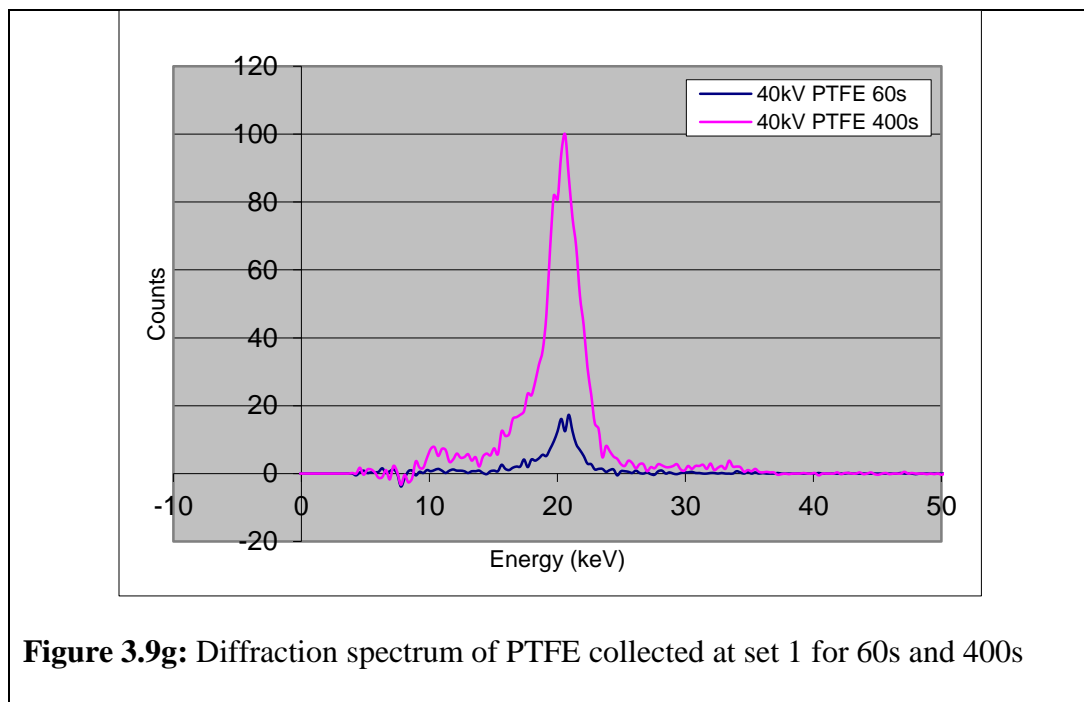


Figure 3.9d: Diffraction spectrum of PVC collected at set 1 for 60s and 400s (negative counts appear when the background is subtracted from the sample spectrum containing sample attenuation of the characteristic lines)

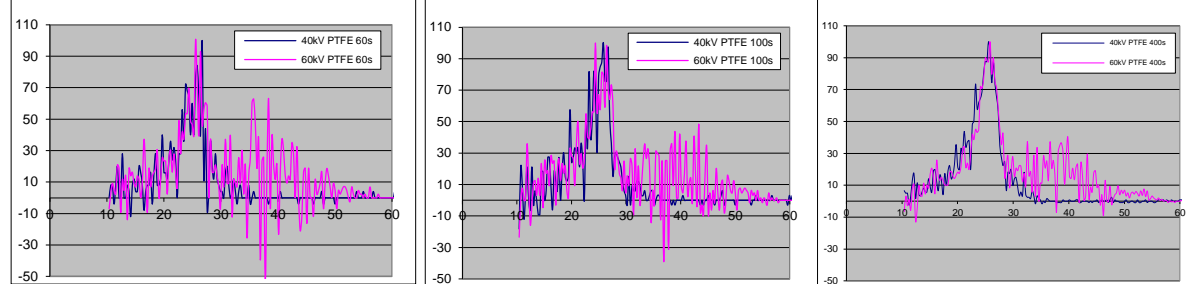




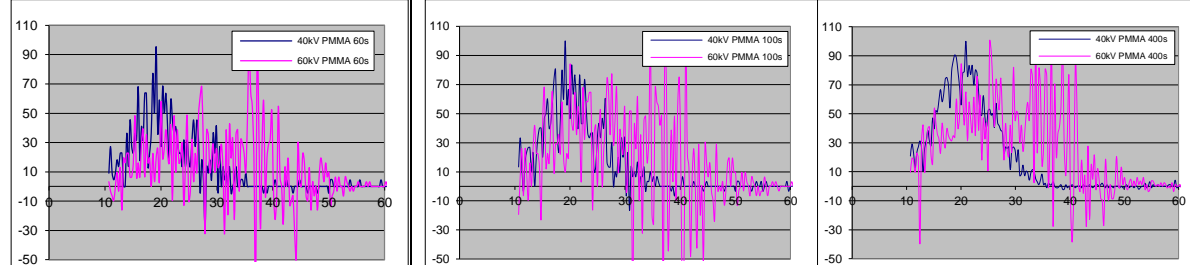
The spectra shown in Figure 3.9 show that for materials like PMMA and PVC the peaks are broader with (FWHM) widths upto 0.8 nm^{-1} . For plastics like PTFE, PE the major peak positions are in agreement with the JCPDS data upto 0.2 nm^{-1} on momentum transfer axis (about 4.7 keV on the energy axis). The overall characteristic profile shape for plastics and pharmaceutical drugs is in agreement with JCPDS. However, the shape of the spectra is more explicit only for the higher acquisition time.

As we move from Set 1 to Set 2, the source collimator gets wider allowing more photons to enter the sample. However, the detector collimator is narrower in Set 2. The spectra taken at Set 2 have wider peaks than that taken at Set 1. The profile shape is worse with Set 2. Figure 3.10 shows comparison of normalized diffraction spectra measured at Set 2 and Set 3 for 60s, 100s and 400s. The spectra are more characteristic at higher acquisition time for both the sets. However, it is the set 3 that allows the high energy peaks to appear on the spectra, as seen from Caffeine and PTFE spectra.

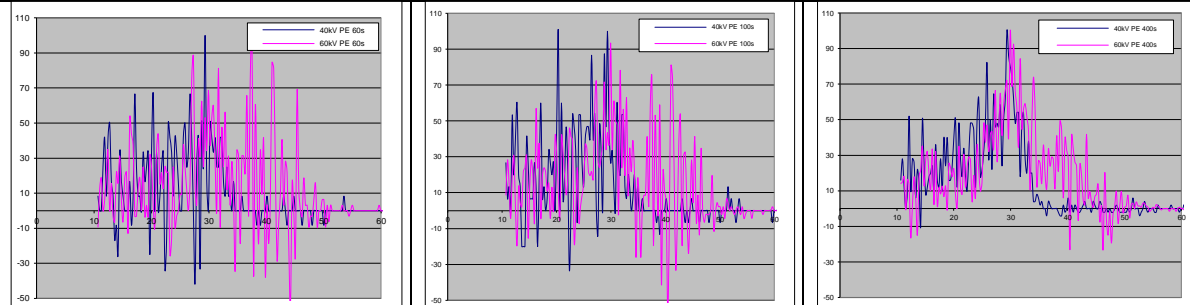
PTFE for 60s, 100s and 400s



PMMA for 60s, 100s and 400s



PE for 60s, 100s and 400s



Caffeine for 60s, 100s and 400s

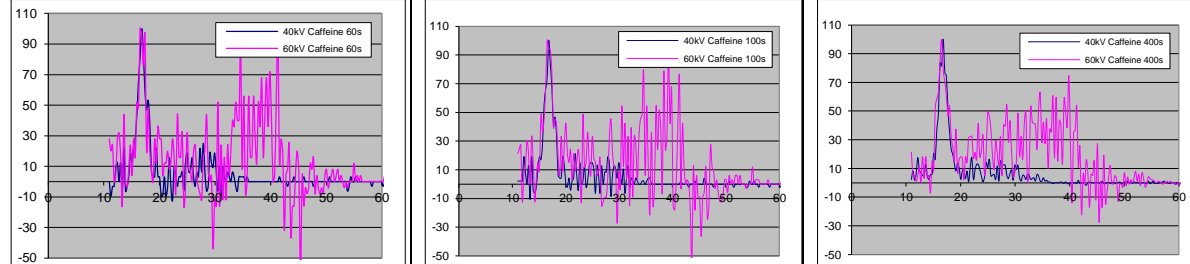
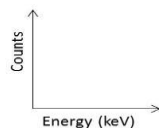


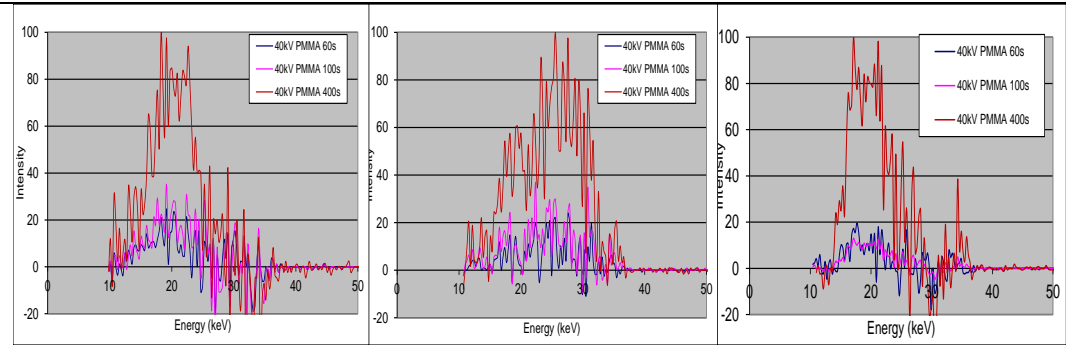
Figure 3.10: Normalized Photon Intensity (counts) against Energy (keV) diffraction spectra measured at set 2 and 3: 40 and 60 kV; 1.1, 0.5 mm



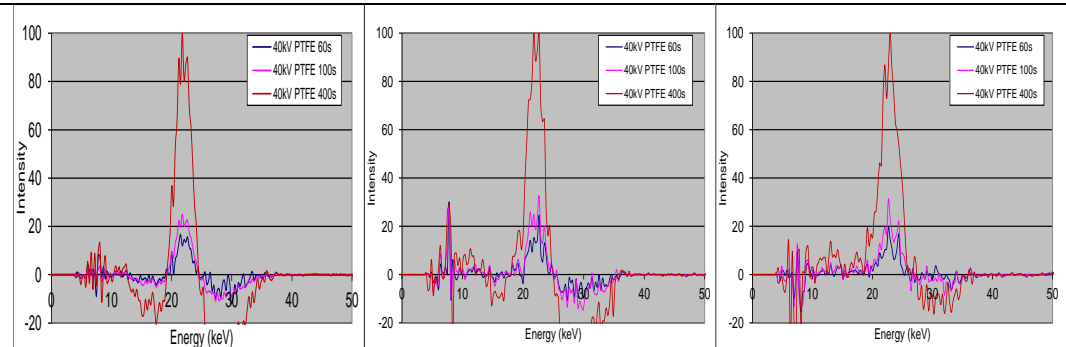
3.3.2 Spectra for large samples – breast-equivalent tissues

Tissues have been characterised using cuboid shaped phantoms described earlier in this chapter. These phantoms were prepared for 2cm, 3cm and 4 cm thickness. Diffraction spectra were recorded for each of these thicknesses at Set 1, 2 and 3 system settings. These spectra are presented in Figures 3.11 and 3.12.

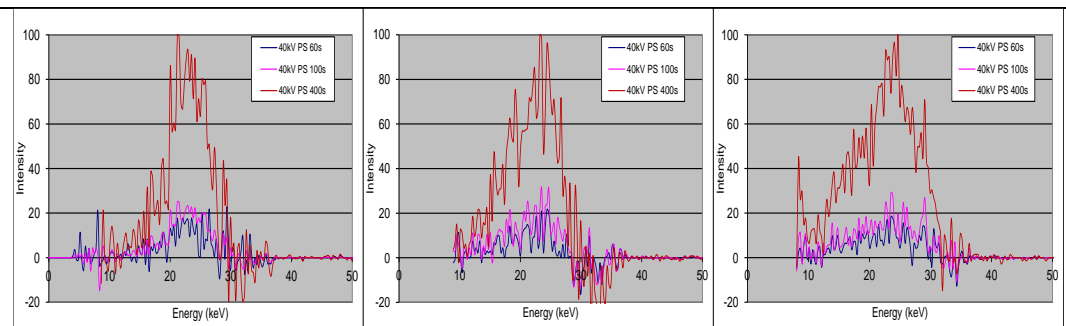
PMMA 2cm, 3cm and 4cm



PTFE 2cm, 3cm and 4cm



PS 2cm, 3cm and 4cm



PE 2cm, 3cm and 4cm

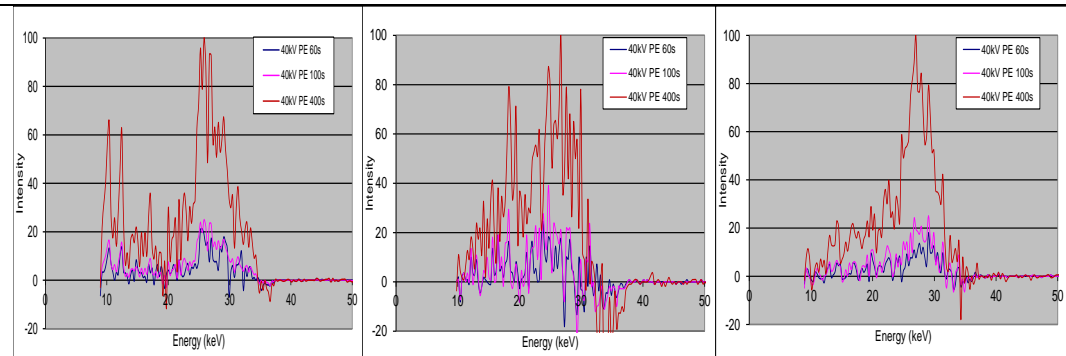


Figure 3.11: Normalized Photon Intensity against Energy (keV) diffraction spectra for tissues Set 1: 40 kV 0.5, 0.9 mm; 60s, 100s and 400s

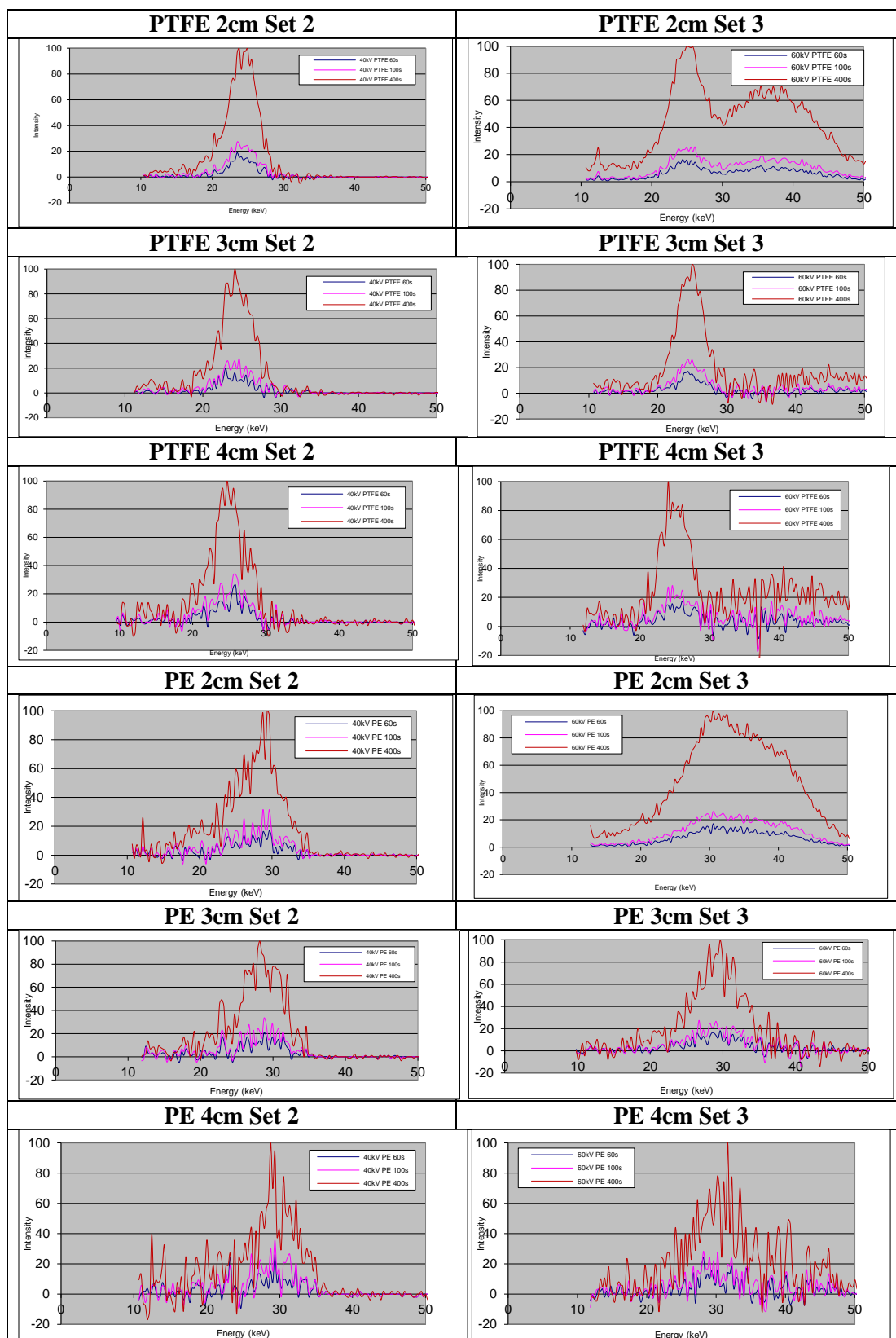


Figure 3.12: Normalized Photon Intensity against Energy (keV) diffraction spectra for tissues for Set 2 and Set 3: 60s, 100s and 400s

From the spectra shown in Figures 3.11 and 3.12, the following are observed:

- (1) For long acquisition times the spectra are more resolved and have the characteristic shape as compared to the short times.
- (2) Spectrum for PTFE and other materials with characteristic spectra having one or two main peaks are better defined in terms of peak positions (shift up to 0.30 nm^{-1}) and peak widths (FWHM) (up to 0.68 nm^{-1}).
- (3) As the thickness of phantoms increases, the peaks in the spectra do not change much with regard to their position, shape and width. The overall characteristic profile of the spectrum for most of the materials is conserved with increasing tissue thickness.
- (4) Set 2 and 3 generated better spectra in terms of peak shape and overall profile even for low acquisition times.
- (5) For spectra obtained with Set 3 that had 60kV, as expected, high energy peaks are more defined as compared to spectra obtained with Set 1 and Set 2.
- (6) With any of the optimised sets, it was indeed possible to clearly see two peaks of the characteristic spectrum of the materials. Hence the system settings are suitable for a sample with a characteristic spectrum containing two peaks. Since this fact depends on the type of material used, for the purpose of tissue characterisation the system has been found to be sufficient.

3.3.3 Spectra for tissues – triangular phantoms

On the same EDXRD system that has been set up with the optimized kV_p and collimator sets, diffraction spectra were recorded by scanning the triangular phantoms at different tissue widths for the range 0.5 – 4.0 cm.

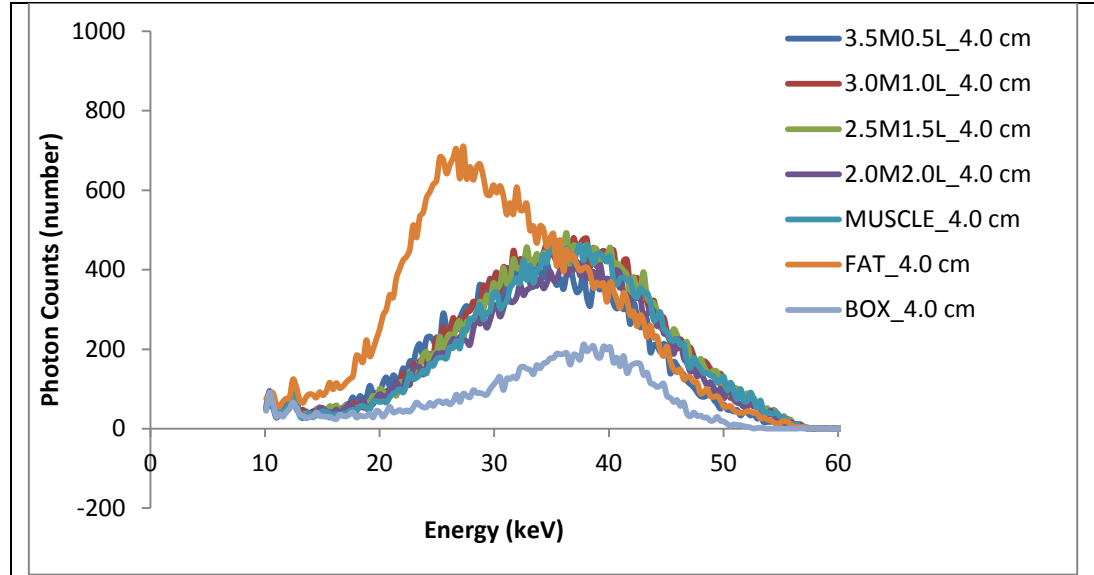


Figure 3.13: Profile of counts against energy (keV) for the breast phantoms with different tissue compositions for set 1

Figure 3.13 shows a plot of counts against energy for the breast phantoms of different tissue compositions measured at Set 1 system settings. As seen, ‘fat only’ peak stands out of the rest of the spectra at 1.1 nm^{-1} (26 keV), with the breast phantoms with mixed composition peaking at 1.6 nm^{-1} (38 keV). The information from these plots is specific to a tissue thickness and will be used in the chapter 4 to produce diffraction images for tissue characterization.

3.4 Tissue diffraction spectrum database

The focus of this research work is to develop a breast tissue diffraction analysis system based on EDXRD technique. In order to have a tissue diffraction analysis system, it is a pre-requisite to have tissue diffraction data. In this chapter the characterisation of materials has been presented. The spectra collected at the optimised system setting for a range of materials, for a range of tissue thickness could all be collected together in the form of a tissue diffraction spectrum database. Table 3.3 presents a tabular form of this tissue diffraction spectrum database.

Table 3.3: Tissue diffraction spectrum database					
Sample No.	System parameters	Tissue thickness (mm)	Object in the tissue	JCPDS Spectrum of object	Measured spectrum
1	Set 1	5	-	-	√
2	Set 1	10	-	-	√
3	Set 1	15	-	-	√
4	Set 1	20	-	-	√
5	Set 1	25	-	-	√
6	Set 1	30	-	-	√
7	Set 1	35	-	-	√
8	Set 1	40	-	-	√
9	Set 1	20	PTFE	√	√
10	Set 1	20	PE	√	√
11	Set 1	20	PVC	√	√
12	Set 1	20	PMMA	√	√
13	Set 1	20	PP	√	√
14	Set 1	20	PE	√	√
15	Set 1	20	PS	√	√
16	Set 1	20	Caffeine	√	√
17	Set 1	20	Paracetamol	√	√
18	Set 1	30	PTFE	√	√
19	Set 1	30	PE	√	√
20	Set 1	30	PVC	√	√
21	Set 1	30	PMMA	√	√
22	Set 1	30	PP	√	√
23	Set 1	30	PE	√	√
24	Set 1	30	PS	√	√
25	Set 1	30	Caffeine	√	√
26	Set 1	30	Paracetamol	√	√
27	Set 1	40	PTFE	√	√
28	Set 1	40	PE	√	√
29	Set 1	40	PVC	√	√
30	Set 1	40	PMMA	√	√
31	Set 1	40	PP	√	√
32	Set 1	40	PE	√	√
33	Set 1	40	PS	√	√
34	Set 1	40	Caffeine	√	√
35	Set 1	40	Paracetamol	√	√
36	Set 2	5	-	-	√
37	Set 2	10	-	-	√
38	Set 2	15	-	-	√
39	Set 2	20	-	-	√

40	Set 2	25	-	-	√
41	Set 2	30	-	-	√
42	Set 2	35	-	-	√
43	Set 2	40	-	-	√
44	Set 2	20	PTFE	√	√
45	Set 2	20	PE	√	√
46	Set 2	20	PVC	√	√
47	Set 2	20	PMMA	√	√
48	Set 2	20	PP	√	√
49	Set 2	20	PE	√	√
50	Set 2	20	PS	√	√
51	Set 2	20	Caffeine	√	√
52	Set 2	20	Paracetamol	√	√
53	Set 2	30	PTFE	√	√
54	Set 2	30	PE	√	√
55	Set 2	30	PVC	√	√
56	Set 2	30	PMMA	√	√
57	Set 2	30	PP	√	√
58	Set 2	30	PE	√	√
59	Set 2	30	PS	√	√
60	Set 2	30	Caffeine	√	√
61	Set 2	30	Paracetamol	√	√
62	Set 2	40	PTFE	√	√
63	Set 2	40	PE	√	√
64	Set 2	40	PVC	√	√
65	Set 2	40	PMMA	√	√
66	Set 2	40	PP	√	√
67	Set 2	40	PE	√	√
68	Set 2	40	PS	√	√
69	Set 2	40	Caffeine	√	√
70	Set 2	40	Paracetamol	√	√
71	Set 3	5	-	-	√
72	Set 3	10	-	-	√
73	Set 3	15	-	-	√
74	Set 3	20	-	-	√
75	Set 3	25	-	-	√
76	Set 3	30	-	-	√
77	Set 3	35	-	-	√
78	Set 3	40	-	-	√
79	Set 3	20	PTFE	√	√
80	Set 3	20	PE	√	√
81	Set 3	20	PVC	√	√
82	Set 3	20	PMMA	√	√
83	Set 3	20	PP	√	√

84	Set 3	20	PE	√	√
85	Set 3	20	PS	√	√
86	Set 3	20	Caffeine	√	√
87	Set 3	20	Paracetamol	√	√
88	Set 3	30	PTFE	√	√
89	Set 3	30	PE	√	√
90	Set 3	30	PVC	√	√
91	Set 3	30	PMMA	√	√
92	Set 3	30	PP	√	√
93	Set 3	30	PE	√	√
94	Set 3	30	PS	√	√
95	Set 3	30	Caffeine	√	√
96	Set 3	30	Paracetamol	√	√
97	Set 3	40	PTFE	√	√
98	Set 3	40	PE	√	√
99	Set 3	40	PVC	√	√
100	Set 3	40	PMMA	√	√
101	Set 3	40	PP	√	√
102	Set 3	40	PE	√	√
103	Set 3	40	PS	√	√
104	Set 3	40	Caffeine	√	√
105	Set 3	40	Paracetamol	√	√

This table can be extended by adding more objects and tissue thickness values in addition to different sets of system parameters. Diffraction data from this database can be used to produce diffraction images for tumour detection. This is explained in the following chapter, Chapter 4.

Chapter 4

Breast Tissue Diffraction Analysis System

The aim of this research work is to develop a breast tissue diffraction analysis system based on EDXRD technique. This chapter describes how the collected diffraction data have been further analysed to produce diffraction images representing breast tissues and tumour. This could provide an additional informational source for breast imaging in terms of tissue composition and hence tumour detection.

4.1 Breast tissue diffraction data analysis

As described in the chapter 3, triangle-shaped breast phantoms were prepared to explore breast thickness and tumour detection. The data collected is a set of diffraction measurements taken for a breast tissue composition i.e., varying amounts of muscle and fat, for tissue widths of the range 0.5 – 4.0 cm. This data could provide an insight into tissue composition. Diffraction data taken with cuboid-shaped breast phantoms could serve as a useful data to mimic the path traversed by a photon on entering the breast. All these diffraction measurements form a database of diffraction spectra that is analysed further to produce diffraction images. For instance, Figure 4.1 shows diffraction spectra

corresponding to 4 cm width for different tissue composition phantoms and PTFE for 40kV and (0.5,0.9) mm collimator set.

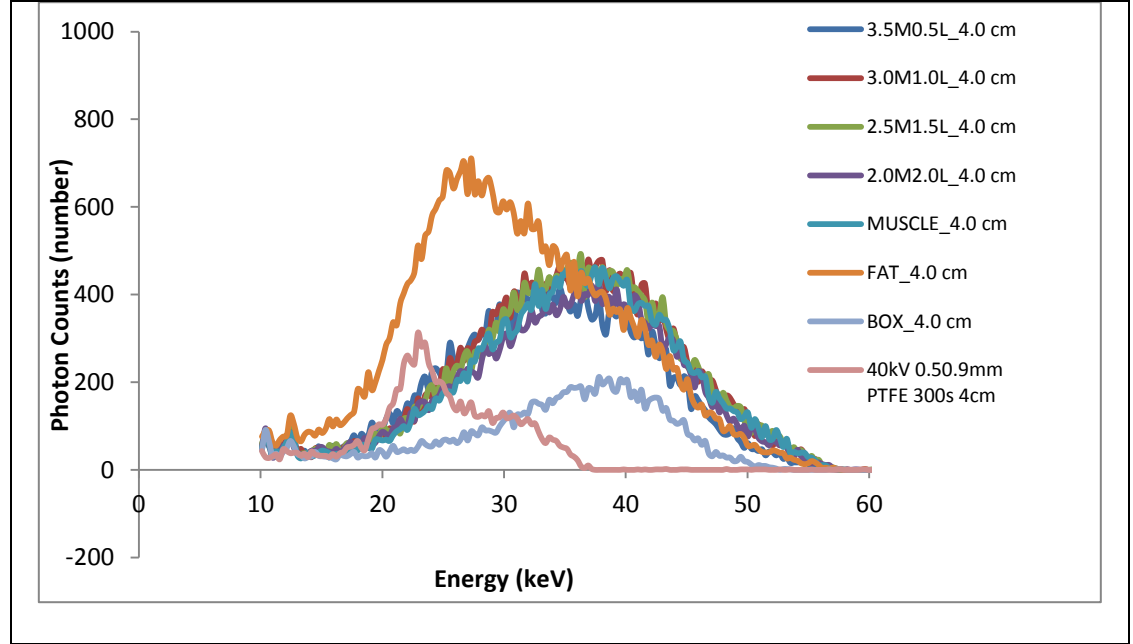


Figure 4.1: Diffraction spectra for breast phantoms and PTFE; PTFE: 4cm thickness, 40 kV, (0.5,0.9) mm collimator set

From the spectra of Figure 4.1 one can see that breast tissue spectra cluster together in the high energy region of 35 keV overlapping with muscle only phantom with the exception of lighter fat shifting towards 25 keV. The PTFE has a low density than the breast tissues (muscle) and its characteristic peaks is seen at 24 keV (1.0 nm^{-1}). The difference in densities of the two is reflected in the ratio of intensities of the mixed tissues to that of the PTFE, $\sim 2:1$. This difference could be used to characterize tissues of the breast and hence locate tumour. Therefore, spectra corresponding to a particular width of the breast could be used to obtain a function of the distance traversed by a photon within the breast. This information

could further be used in generating a diffraction image wherein the pixels would have intensities as a function of these path lengths.

In order to apply this approach to the whole of database, integrated counts under the diffraction spectra collected for the tissue width range 0.5 – 4.0 cm were plotted against the widths. Figure 4.2a, 4.2b, 4.2c show integrated counts over the full spectrum plotted against tissue width for different tissue compositions for the three sets of system geometry predicted by the model.

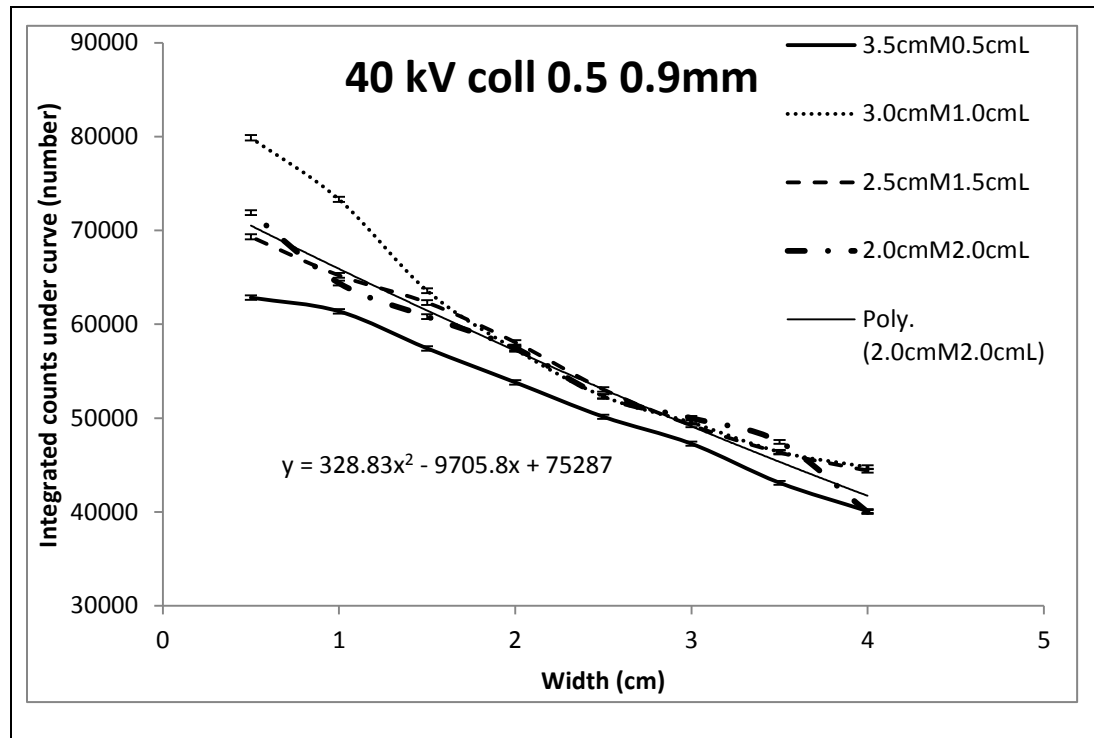


Figure 4.2a: Integrated counts over the full spectrum plotted against tissue width of breast tissues for different tissue composition; Set1: 40 kV; (0.5,0.9) mm collimator set; Also shown is the fitted curve and equation for 2.0cmM2.0cmL

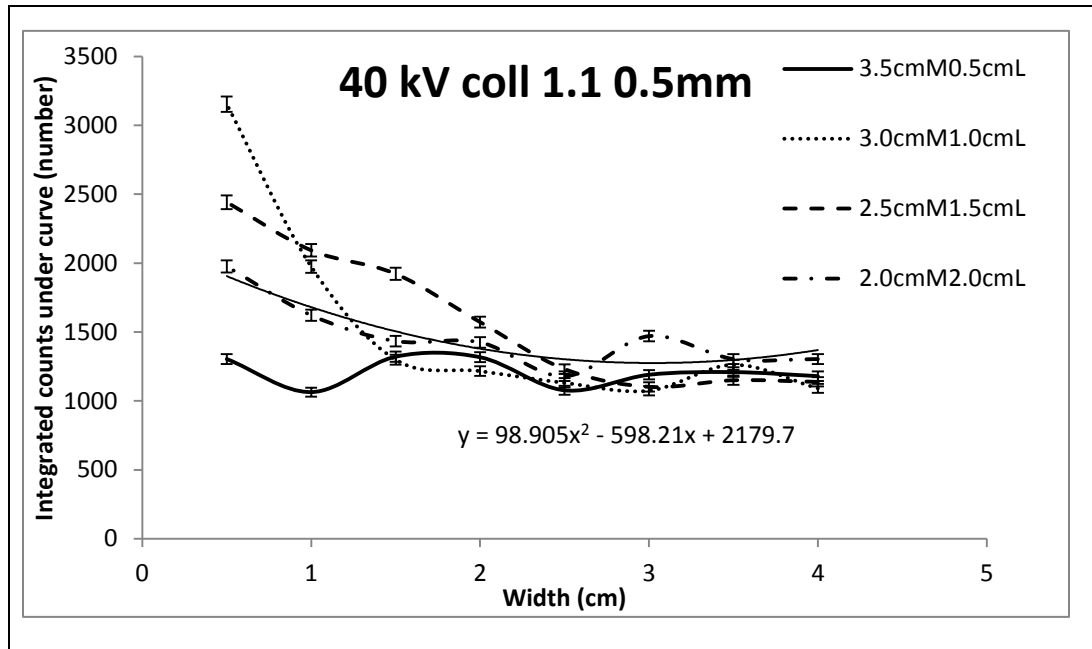


Figure 4.2b: Integrated counts over the full spectrum plotted against tissue width of breast tissues for different tissue composition; Set2: 40 kV; (1.1,0.5) mm collimator set; Also shown is the fitted curve and equation for 2.0cmM2.0cmL

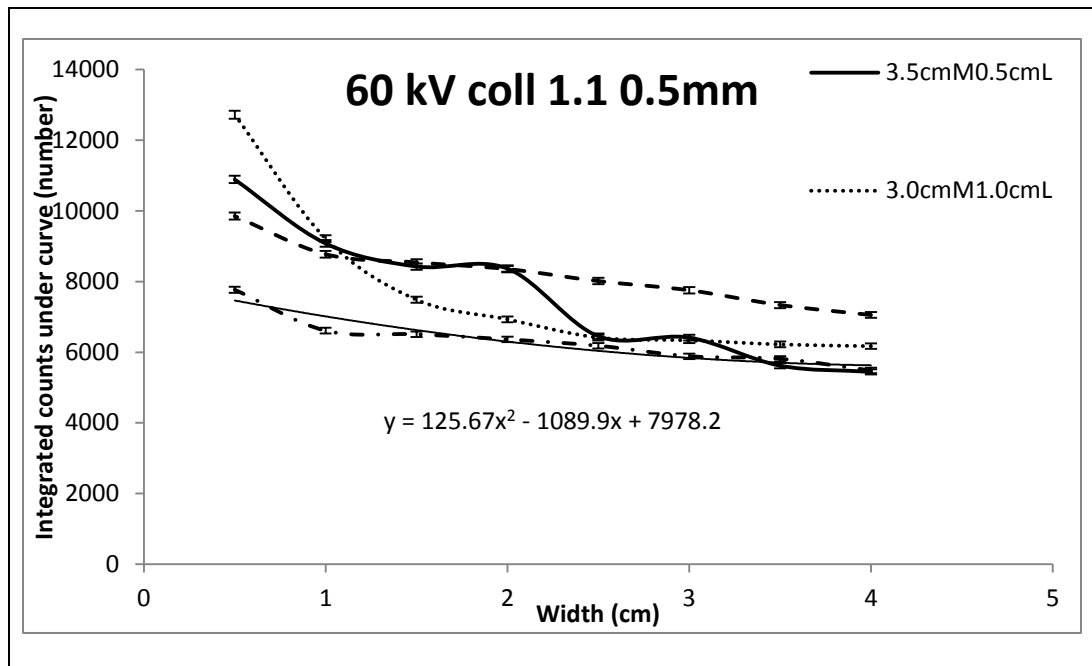


Figure 4.2c: Integrated counts over the full spectrum plotted against tissue width of breast tissues for different tissue composition; Set3: 60 kV; (1.1,0.5) mm collimator set; Also shown is the fitted curve and equation for 2.0cmM2.0cmL

- (1) From Figure 4.2a, 4.2b, 4.2c one can note that counts are high for a thinner tissue slice than a thick chunk of tissue. The counts fall as we move from 0.5 cm towards 4.0 cm width. This trend is seen for all geometrical sets 1, 2 and 3.
- (2) For 40 kV sets only i.e., set1 and set2, the counts are higher for collimator set 1.1,0.5 mm than 0.5,0.9 mm accounting for higher photon flux through the bigger source collimator, 1.1 mm.
- (3) As we move to set3, higher kV_p value of 60 kV justifies the increase in counts.
- (4) The difference in counts with change in muscle and fat compositions indicates the sensitivity of the system to tissue composition. The error bars further indicate that the curves are quite distinct at lower widths although the difference reduces with increase in width.
- (5) A polynomial curve is fitted to these data points to be able to use it to calculate the photon intensity for any given path length in the range.
- (6) Difference in curves for different tissue composition demands for separate curve fits for each data set. For instance, for a composition of 2.0M2.0L with equal amount of muscle and fat, curve fit and equations obtained have been shown above in Figure 4.2a, 4.2b, 4.2c and used in the analysis to follow. Equations have been obtained for each of the curves fitted. These equations will be used to produce diffraction images as explained in the following sections.

4.2 Representation of breast

In order to produce diffraction images of breast tissue, for simplicity, the breast has been taken as a hemi-spherical shaped object. As shown in Figure 4.3, for a photon to enter the breast and traverse a length through it, the chord of the spherical cap of the breast is the best geometrical representation of the path length. Thus, a distance of $2a$ in Figure 4.3 is the maximum that a photon can traverse through the breast at a distance h from the nipple.

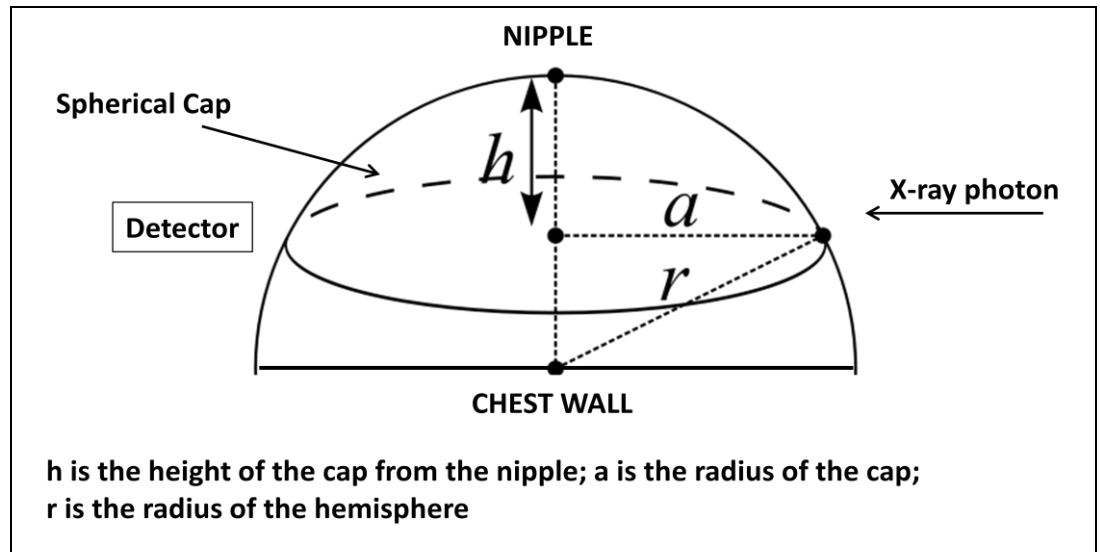


Figure 4.3: Breast representation and photon path length

The current imaging modalities place detectors very close to the breast to extract maximal tissue information, therefore, for the present work, any scattering directions have been omitted and each of these chords of the various layers of spherical caps represent a path length that a photon can take while it is within the breast. The above geometry of the breast and the spherical caps have been

modeled in IDL to calculate the path lengths for a step size (h in Figure 4.3) of 0.5 cm. Hence for an average breast of diameter 4.0 cm a 9 X 5 matrix is obtained as follows:

The path lengths have been obtained for different sets of h and h_1 where h is the distance of the cap from the nipple and h_1 is the size of the chords of the cap: h ranging from 0 to 4.0 cm, in steps of 0.5 cm, for each value of h , h_1 ranging from 0 to 4.0 cm in steps of 0.5 cm. This covers the whole breast and the matrix obtained allows a mapping of these values on to an image with 9 X 5 pixels.

Recalling the equations obtained in section 4.1, these equations are functions of the chords of the spherical cap or the path lengths and an intensity value can be obtained corresponding to each of the calculated path lengths. The image filled with these intensity values on plotting represents the tissue depending on choice of h and h_1 . This concept will show its significance in the following section where diffraction images are presented to study breast tissues and diffraction system.

4.3 Diffraction images for breast tissue characterisation

In order to characterize breast tissues a significant difference between the intensity values of the pixel(s) representing them is essential. This has implications to locating tumour in the breast. A breast tumour is denser than the normal tissues but denser breast tissues could obscure the presence of tumour on an image. To explore characterisation of breast tissues, diffraction images have

been produced using equations corresponding to that of the curve fits for diffraction spectra data for plastics like PVC, PP, PTFE and pharmaceutical drugs like Caffeine and Paracetamol obtained using cuboid breast phantoms. In these experiments a straw of diameter 0.5 cm was placed in breast phantoms of thickness 2, 3 and 4 cm. Using the diffraction data for these three thickness values, plots as shown in Figure 4.4a-h have been produced wherein integrated counts over the full spectrum against sample width for the three sets of system geometry predicted by the model i.e. set1, 2 and 3 with following parameters:

Set1: 40 kV; (0.5,0.9) mm collimator set

Set2: 40 kV; (1.1,0.5) mm collimator set

Set3: 60 kV; (1.1,0.5) mm collimator set

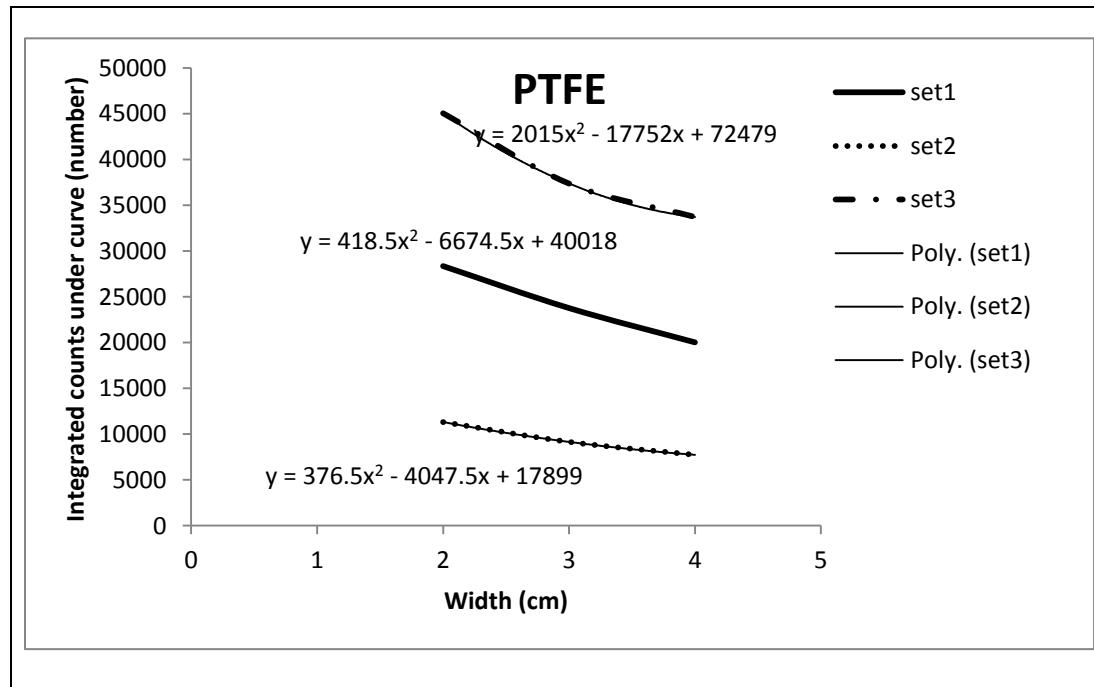


Figure 4.4a: Plot of integrated counts over the full spectrum against sample width for PTFE for the three sets of system geometry predicted by the model set1, set2 and set3; Also shown are the corresponding fitted curves and equations

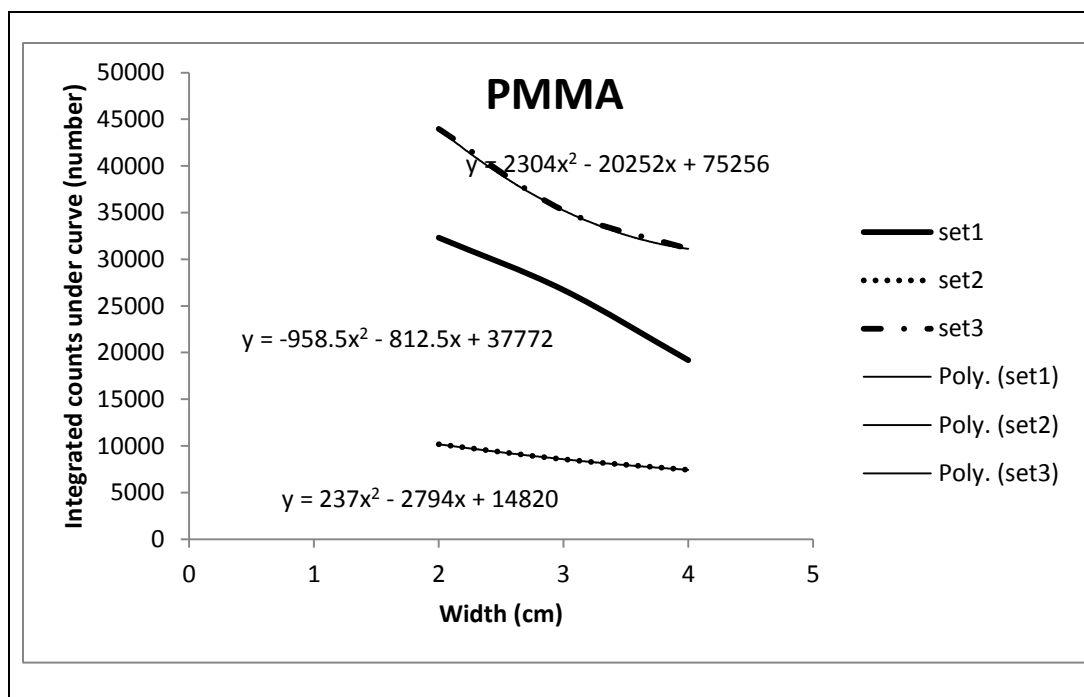


Figure 4.4b: Plot of integrated counts over the full spectrum against sample width for PMMA for the three sets of system geometry predicted by the model set1, set2 and set3; Also shown are the corresponding fitted curves and equations

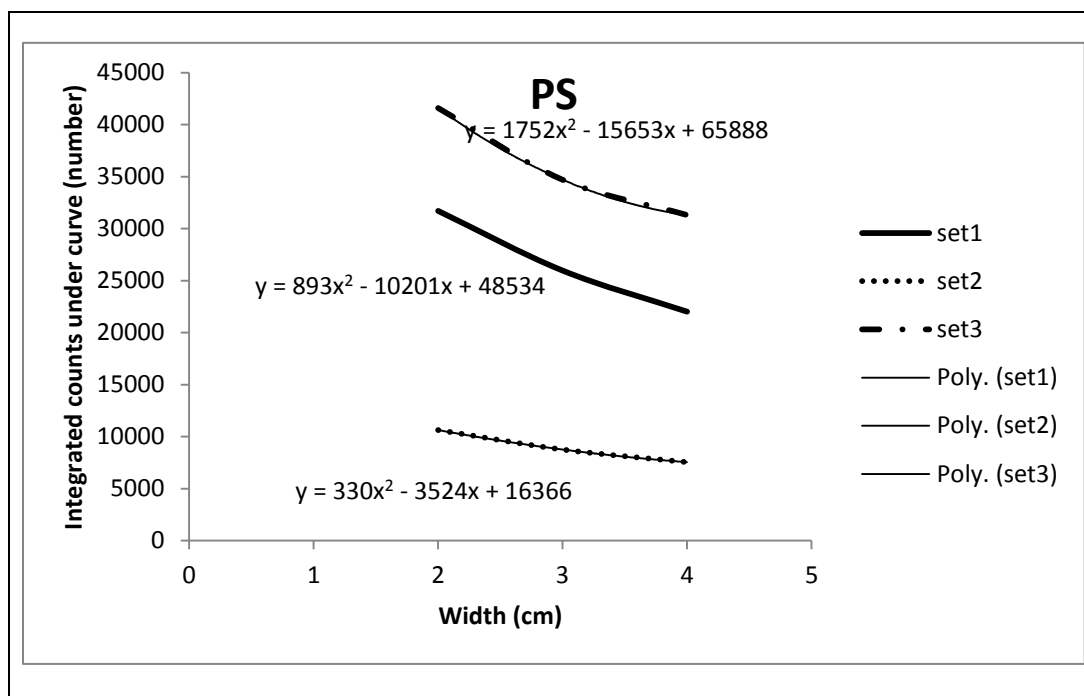


Figure 4.4c: Plot of integrated counts over the full spectrum against sample width for PS for the three sets of system geometry predicted by the model set1, set2 and set3; Also shown are the corresponding fitted curves and equations

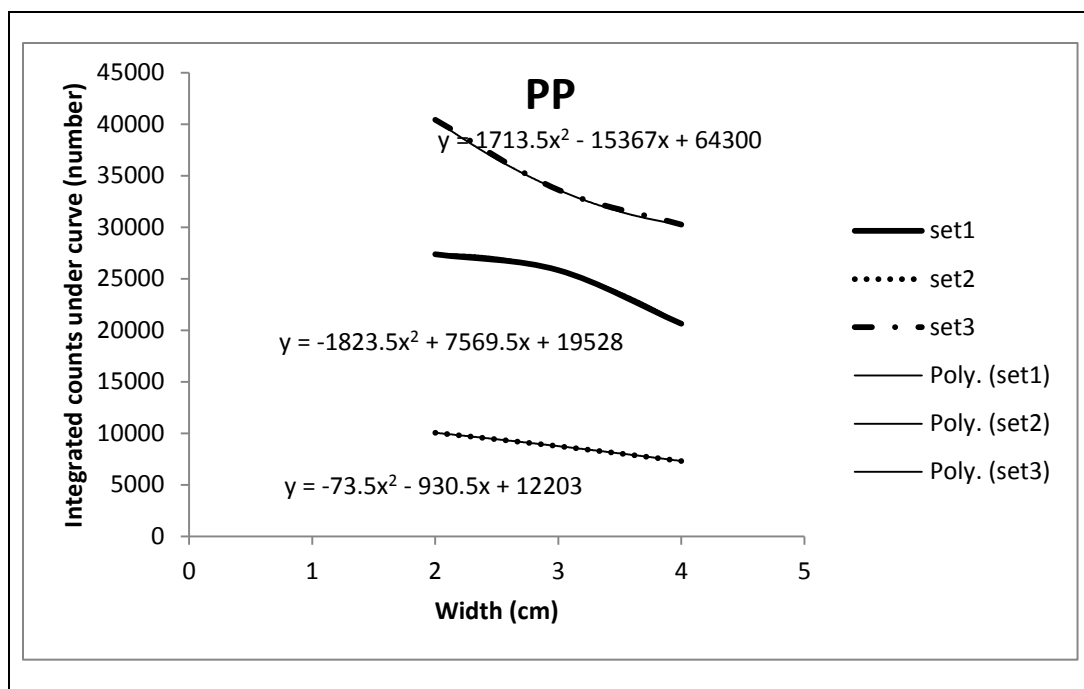


Figure 4.4d: Plot of integrated counts over the full spectrum against sample width for PP for the three sets of system geometry predicted by the model set1, set2 and set3; Also shown are the corresponding fitted curves and equations

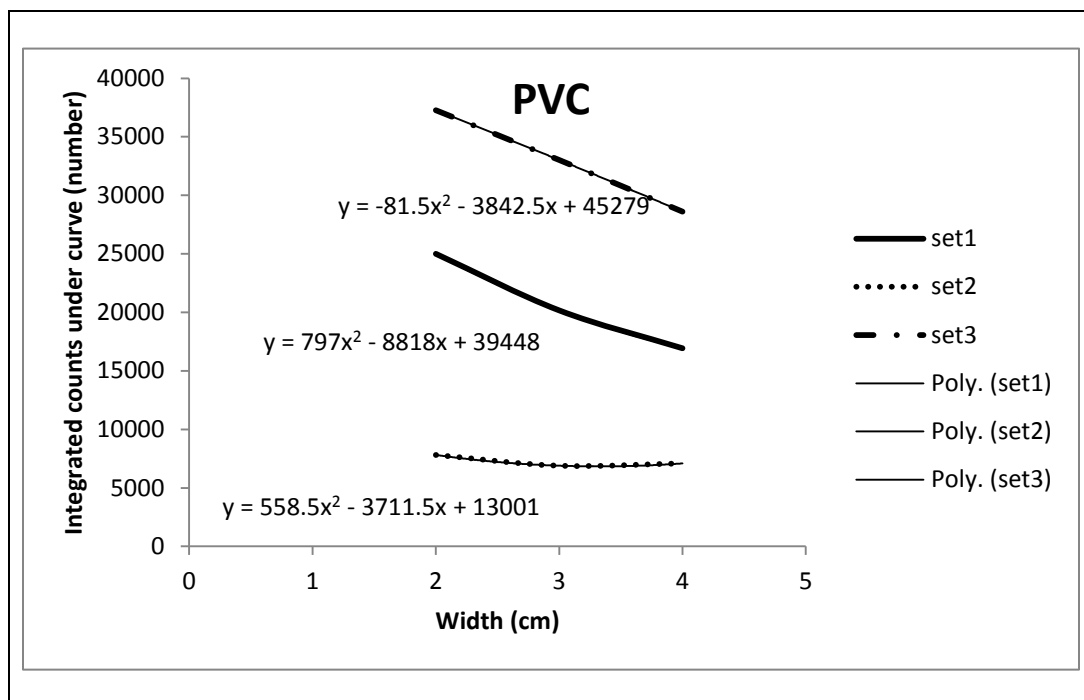


Figure 4.4e: Plot of integrated counts over the full spectrum against sample width for PVC for the three sets of system geometry predicted by the model set1, set2 and set3; Also shown are the corresponding fitted curves and equations

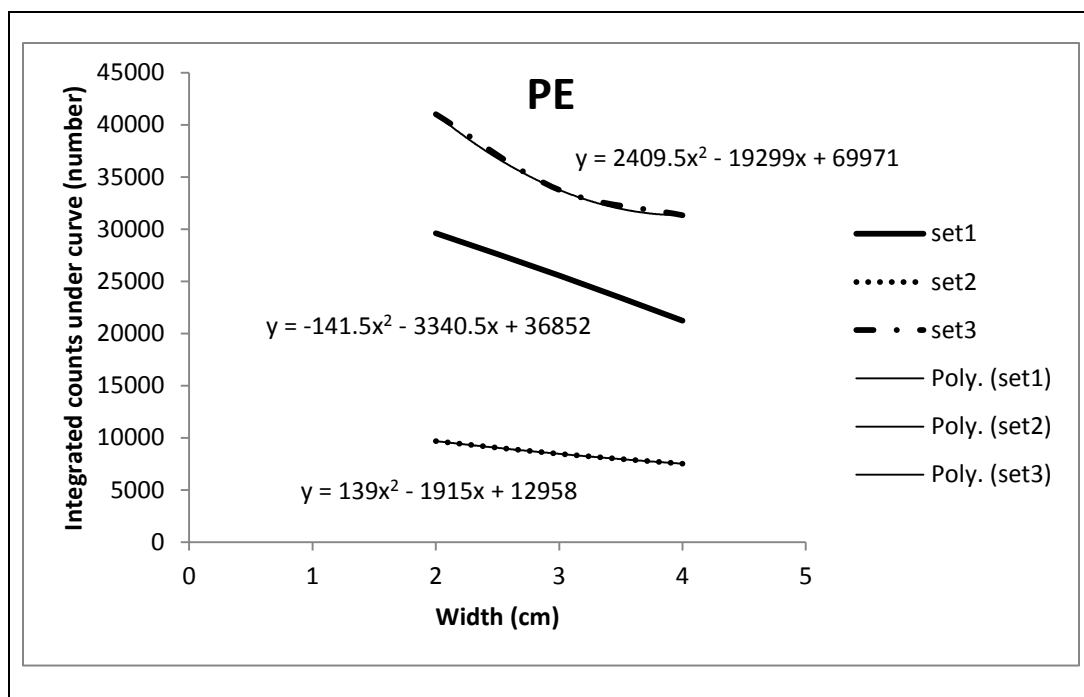


Figure 4.4f: Plot of integrated counts over the full spectrum against sample width for PE for the three sets of system geometry predicted by the model set1, set2 and set3; Also shown are the corresponding fitted curves and equations

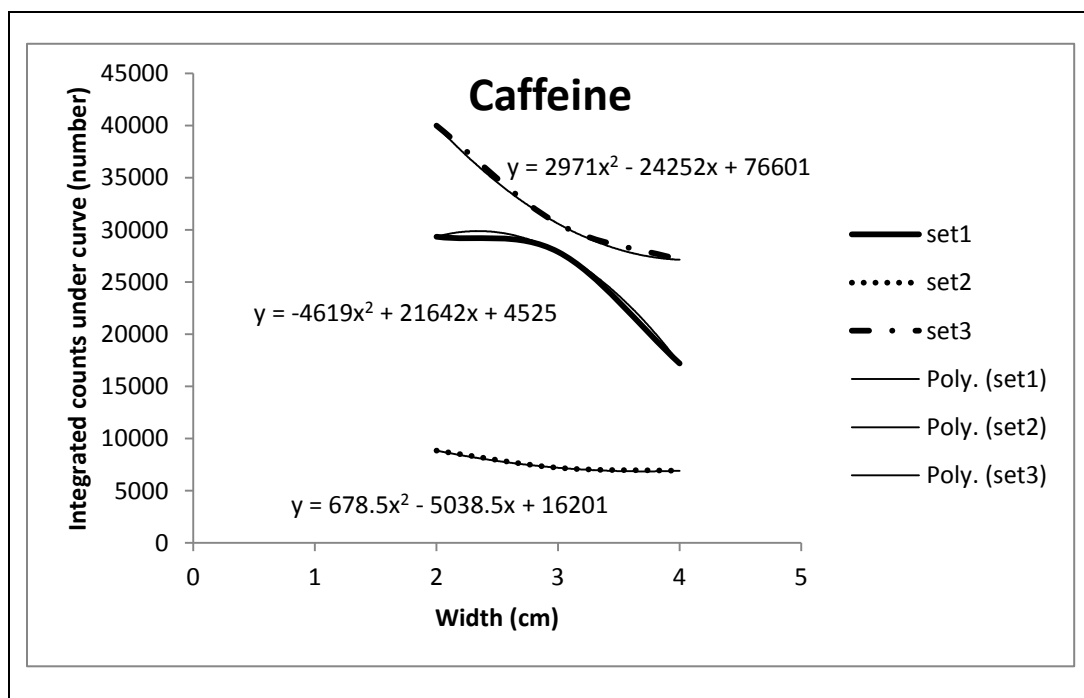


Figure 4.4g: Plot of integrated counts over the full spectrum against sample width for Caffeine for the three sets of system geometry predicted by the model set1, set2 and set3; Also shown are the corresponding fitted curves and equations

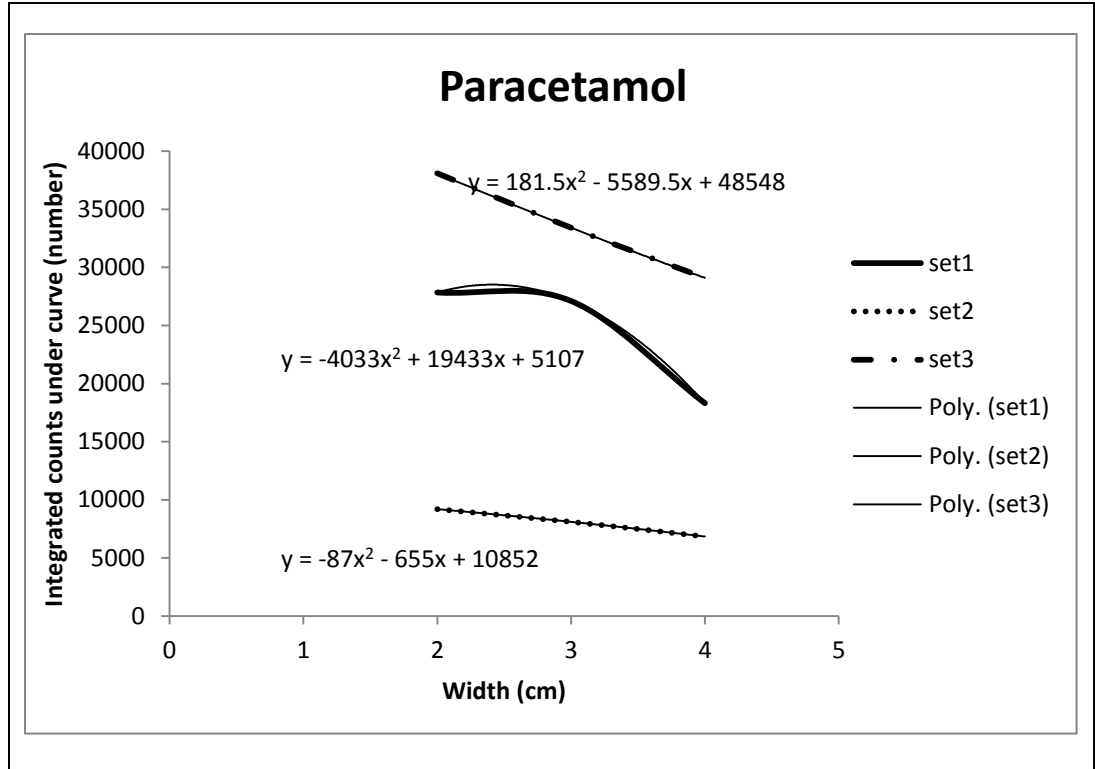


Figure 4.4h: Plot of integrated counts over the full spectrum against sample width for Paracetamol for the three sets of system geometry predicted by the model set1, set2 and set3; Also shown are the corresponding fitted curves and equations

A polynomial curve is fitted to the data points for each of the sets and the corresponding equation is obtained. This equation corresponding to a sample is used in the function of the path length travelled by the photon inside the breast (as detailed in section 4.2 on breast representation). Therefore, the intensity of the pixel corresponding to the sample is obtained. The samples have been used as tumour substitutes. To produce a diffraction image of a breast containing a tumour (a sample), a code was written in IDL that calculated the value of each of the pixels of the breast image using equations from Figure 4.2 and Figure 4.4 in a

function obtained from the breast representation of section 4.2. Under different system geometries, the position of tumour and its size i.e. number of pixels, have been varied. Diffraction images have been produced for a breast of size 4.0 cm for all combinations of

(1) System geometry set :

Set1

Set2

Set3

(2) Position of tumour in the breast :

pos1 (in the middle but close to chest wall)

pos2 (towards one side but close to surface)

pos3 (right behind the nipple)

(3) Size of tumour i.e. number of pixels :

0.5 cm – 1 pixel (1pix)

1.0 cm – 2 pixels (2pix)

2.0 cm – 4 pixels (4pix)

Diffraction images for PMMA and Paracetamol are shown in Figure 4.5a, 4.5b respectively.

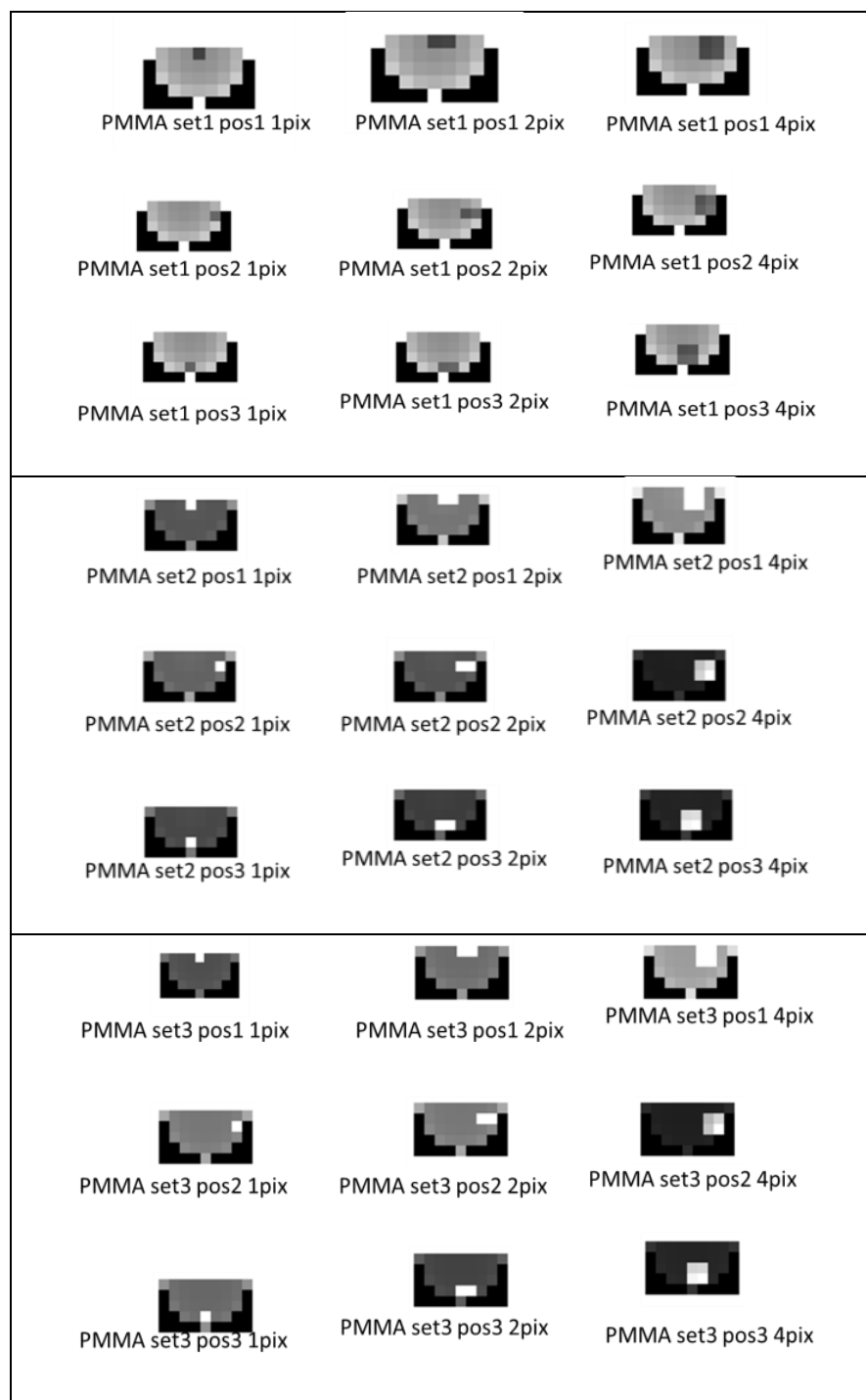


Figure 4.5a: Diffraction images for tissue characterisation for PMMA for Sets 1,2 and 3; Sample positions 1,2 and 3; Number of pixels 1,2 and 4

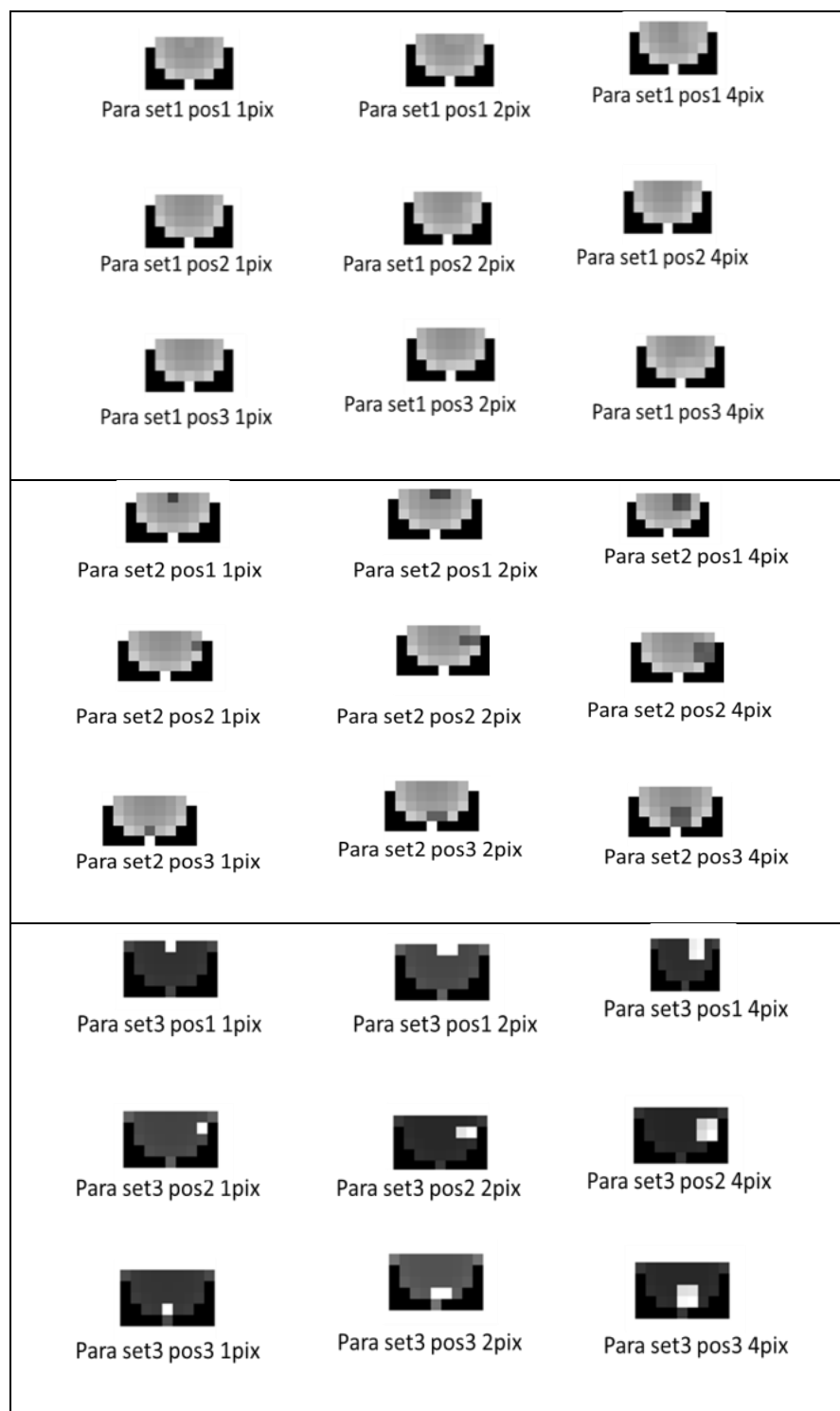


Figure 4.5b: Diffraction images for tissue characterisation for Paracetamol for Sets 1,2 and 3; Sample positions 1,2 and 3; Number of pixels 1,2 and 4

- (1) According to the above representation of the shape of the breast a photon entering the breast around the nipple area has a smaller path length to travel than at the chest wall. Therefore, a sample (tumour) located near the nipple is easily identifiable than the one embedded deep inside. This is also observed when the size of the tumour grows i.e. when the number of pixels is increased to four wherein the pixel closer to the breast surface has a higher intensity.
- (2) Set 2 gives better tumour detectability than set 1 due to high photon flux. However, it depends on the material and the way the diffraction information has been used. For instance, diffraction intensity corresponding to a specific window (energy ranges) can be picked depending on the analysis.
- (3) Higher kV_p value of set 3 improves the photon intensity and hence the tumour detection even if the position of tumour is close to chest wall.
- (4) One pixel sized tumour (size 0.5 cm) is identifiable though not in all cases. The larger the number of pixels the bigger the size of tumour and hence the harder the tumour detection.
- (5) In the case of Paracetamol (image shown below for 4 pixel sized tumour located close to nipple), the image corresponding to set 1 shows a low intensity corresponding to the sample (tumour) although the tumour is big enough for detection. Detection of tumour of a size of four pixels is improved

by set 3. In addition to geometric resolution provided by set 3, this could be due to higher kV as the peaks of Paracetamol and the muscle fall in the region 25-35 keV.



As seen in this chapter, the diffraction measurements have been used to produce diffraction images for tissue characterization and hence tumour detection. The geometric parameter settings are important in tumour detection depending on the position and size of the tumour. By choosing appropriate energy bands for the analysis, tumour detection can be enhanced. Further improvements can be made to this analysis and are discussed in the Conclusions chapter.

Chapter 5

Conclusions and Future Work

The focus of the presented research work is to develop a tissue diffraction analysis system. The work of Kidane et al., 1999 and the like have proved the potential for Energy-dispersive X-ray diffraction techniques in tissue characterisation. However, the work done so far has been with small tissue sizes in the range of millimeters. In order to associate the Energy-dispersive X-ray diffraction technique with breast tissues there is a need for extending the tissue sizes used by the technique to large ones, of the breast sizes. This work is an effort in this direction.

5.1 Conclusion

Keeping the aims of the work in mind the following can be concluded about the work:

- (1) The geometry of an EDXRD system is the basis of the system resolution and hence the spectral resolution. In order to obtain most optimum system geometry for breast sized samples, a model based on ray tracing of photons has been successfully developed.

- (2) The model could be used to predict spectra for materials in the momentum transfer range $0.5 - 3.0 \text{ nm}^{-1}$.
- (3) The predicted spectra had an average peak shift (with respect to the JCPDS spectra) of about 0.30 nm^{-1} and an average peak width (FWHM) of 0.20 nm^{-1} .
- (4) The model predicted spectra were used to successfully optimize the system geometry for large samples of the size of a breast.
- (5) Three sets have been obtained as a result of optimization.

Sets - System Geometry Optimisation based on Model Predictions					
Optimised geometry set no.	kV _p value (kV)	Scatter Angle (degree)	Collimator set no.	Source Collimator width (mm)	Detector Collimator width (mm)
1	40	6	4	0.5	0.9
2	40	6	2	1.1	0.5
3	60	6	2	1.1	0.5

- (6) From characterisation of tissues using these optimized system parameters sets, peak parameters obtained with large samples have been found to be in a similar range for all the sets, however, the spectra measured with set 3 showed better characteristic shape profile even in high energy range.

- (7) The material characterisation using 3 system parameter sets, 6 plastics, 2 pharmaceutical drugs, breast phantoms (2cm, 3cm and 4cm sizes) and breast phantoms (providing tissue thickness in the range 0.5 – 4.0 cm) have led to a tissue diffraction database of more than 100 spectra in it.
- (8) The database of diffraction spectra has been used to process the information from diffraction spectra to produce diffraction images corresponding to breast tissues with tumours of different sizes, the smallest being 0.5 cm, located at various positions within the breast.

For instance, a tumour of size 0.5 cm (in figure shown below) is blurred under set 1, is visible under set 2 geometry and has a high contrast under set 3 geometry. The above fact re-iterates the significance of the geometrical parameters of an EDXRD system. Thus suitable system parameters are required depending on the type of materials being characterised.



(9) Set 3 system parameter settings included a higher kV_p value. For breast tissue imaging, this could be interpreted as a lower dose delivered to the patient.

The breast tissue diffraction analysis system could provide an additional source of information for breast imaging in terms of tissue composition and tumour detection. Exploration of the tumour sizes and their locations has implications on early and precise detection of breast cancer.

5.2 Future Work

The presented work is a step forward in breast tissue characterisation.

Possible improvements can be made by modeling the EDXRD system and the photon-matter interaction through Monte-Carlo algorithms. Such approaches would allow taking account of multiple-scattering of photons that has not been included in the presented work.

Further, the tissues used in this work are animal tissues. Real human breast tissues can be used for a more realistic data for tissue diffraction analysis.

References:

Adler LP, Crowe JP, al-Kaisi NK, Sunshine JL, Evaluation of breast masses and axillary lymph nodes with [F-18] 2-deoxy-2-fluoro-D-glucose PET, *Radiology* 187(1993) 743-750

American Joint Committee on Cancer (AJCC) – *AJCC Cancer Staging Manual* 6(2002) 2003

American Cancer Society (ACS), *Breast Cancer Facts & Figures*, 2011-2012 (Survival rates are based on patients diagnosed between 2001 and 2007)

Balogun FA, Brunetti A, Cesareo R, Volume of intersection of two cones, *Radn. Phys. and Chem.* 59(2000) 23-30

Banks E, Reeves G, Beral V, Bull D, Crossley B, Simmonds M, Hilton E, Bailey S, Barrett N, Briers P, English R, Jackson A, Kutt E, Lavelle J, Rockall L, Wallis MG, Wilson M, Patnick J, Influence of personal characteristics of individual women on sensitivity and specificity of mammography in the Million Women Study: cohort study, *British Medical Journal*, 329(2004) 477-479

Barroso RC, Lopes RT, de Jesus, EFO, Oliviera LF, X-ray diffraction diffraction microtomography using synchrotron radiation, *Nucl. Instr. and Meth. Phys. Res. A* 471(2001) 75-79

Bockisch A, Freudenberg LS, Schmidt D, Kuwert T, Hybrid Imaging by SPECT/CT and PET/CT: Proven Outcomes in Cancer Imaging, *Seminars in Nuclear Medicine*, 39(4)(2009) 276-289

Boone JM, Chavez AE, *Med. Phys.* 23(1996) 1997 – Photon attenuation data based on this work used in generating mass attenuation coefficient plots using software *XMudat*

Boyd NF, Guo H, Martin LJ, Sun L, Stone J, Fishell E, Jong RA, Hislop G, Chiarelli A, Minkin S, Yaffe MJ, Mammographic Density and the Risk and Detection of Breast Cancer, *N. England J. Med.* 356(2007)

Bravin A, Fiedler S, Thomlinson W, Very low dose mammography: new perspectives in diffraction enhanced imaging (DEI) mammography, *SPIE* 4682(2002) 167–173

Briki F, Busson B, Salicru B, Esteve F, Doucet J, Breast-cancer diagnosis using hair, *Nature* (1999)

Buist DSM, Aiello EJ, Miglioretti DL, White E, Mammographic Breast Density, Dense Area, and Breast Area Differences by Phase in the Menstrual Cycle, *Cancer Epidemiology Biomarkers and Prevention*, 15(2006) 2303-2306

Burns PN, Halliwell M, Wells PNT, Webb AJ, Ultrasonic Doppler studies of the breast, *Ultrasound Med. Biol.* 8(1982) 127-143

Carter CL, Allen C, Henson DE, Relation of tumor size, lymph node status, and survival in 24,740 breast cancer cases, *Cancer* 63(1989) 181-187

Castro CRF, Barroso RC, Anjos MJ, Lopes RT, Braz D, Coherent scattering characteristics of normal and pathological breast human tissues, *Radn. Phys. and Chem.* 71(2004) 649-651

Castro CRF, Barroso RC, de Oliveira LF, Lopes RT, Coherent scattering X-ray imaging at Brazilian National Synchrotron Laboratory: Preliminary breast images, *Nuclear Instruments and Methods in Physics Research A* 548(2005) 116-122

Chakraborty DP, The effect of the anti-scatter grid on full-field digital mammography phantom images, *J. Digit Imaging* 12(1999) 12-22

Changizi V, Oghabian MA, Speller R, Sarkar S, Kheradmand AA, Application of Small Angle X-ray Scattering (SAXS) for Differentiation between Normal and Cancerous Breast Tissue, *Int. J. Med. Sci.* 2(2005) 118-121

Changizi V, Kheradmand AA, Oghabian MA, Application of small-angle X-ray scattering for differentiation among breast tumors, *Med. Phys.* 33(2008)

Cheng X, Mao JM, Bush R, Kopans DB, Moore RH, Chorlton M, Breast cancer detection by mapping haemoglobin concentration and oxygen saturation, *Applied Optics*, 42(2003) 6412-6421

Cherry SR, Multimodality *In Vivo* Imaging Systems: Twice the power or Double the Trouble?, *Annu. Rev. Biomed. Eng.* 8(2006) 35-62

Claus EB, Risch N, Thompson WD, Autosomal dominant inheritance of early-onset breast cancer. Implications for risk prediction, *Cancer* 73(3)(1994) 643-651

Coleman MP et al, Responding to the challenge of cancer in Europe, Ljubljana, *Institute of Public Health*, 2008 (Cross-ref: World Health Statistics 2008)

Coleman MP et al, Research commissioned by Cancer Research UK, 2007, London School of Hygiene and Tropical Medicine (LSHTM), 2010

Cook E, Analysis of EDXRD profiles for material identification, imaging and system control, Ph.D. Thesis, University College London, UK, 2008

Cook E, Fong R, Horrocks J, Wilkinson D, Speller R, Energy dispersive X-ray diffraction as a means to identify illicit materials: A preliminary optimization study, *Applied Radiation and Isotopes* 65(2007) 959-967

Corino GL, French PW, Diagnosis of breast cancer by X-ray diffraction of hair, *Int. J. Cancer*, 122(2008) 847–856

Desouky OS, Elshemy WM, Selim NS, Ashour AH, Analysis of low-angle X-ray scattering peaks from lyophilized biological samples, *Phys. Med. Biol.* 46 (8) (2001) 2099-2106

Evans SH, Bradley DA, Dance DR, Bateman JE, Jones CH, Measurement of small-angle photon scattering for some breast tissues and tissue substitute materials, *Phys. Med. Biol.* 36 (1991) 7-18

Evans DGR, Howell A, Hasnain SS, Grossmann JG, Science or black magic?, *J. Med. Genet.* 38(2001) e16, 2

Fass L, Imaging and cancer: A review, *Molecular Oncology* 2(2008) 115-152

Fernández M, Keyriläinen J, Serimaa R, Torkkeli M, Karjalinen-Lindsberg M-L, Tenhunen M, Thomlinson W, Urban V, Suortti P, Small-angle X-ray scattering studies of human breast tissue samples, *Phys. Med. Bio.*, 47(2002) 577-592

Fernández M, Suhonen H, Keyriläinen J, Bravin A, Fiedler S, Karjalainen-Lindsberg M-L, Leidenius M, von Smitten K, Suortti P, USAXS and SAXS from cancer-bearing breast tissue samples, *European Journal of Radiology* 68S(2008) S89-S94

Frappart L, Remy I, Lin HC, Bremond A, Raudrant D, Grousseau B, Vauzelle JL, Different types of microcalcifications observed in breast pathology, *Virchows Archive* 410(1987) 179-187

Friedenreich C, Review of anthropometric factors and breast cancer risk, *Eur. J. Cancer Prev.* 10(2001) 15-32

Fox GN, Breast cancer risk assessment tool, *The Journal of Family Practice* 49(2000)

Gail MH, Brinton LA, Byar DP, Corle DK, Green SB, Schairer C, Mulvihill JJ, Projecting individualized probabilities of developing breast cancer for white

females who are being examined annually. *J Natl Cancer Inst* 81(1989) 1879-1886

George SA, Barriers to breast cancer screening: an integrative review, *Health Care for Women International* 21(2000) 53-65

Geraki K, Farquharson M, Bradley D, X-ray fluorescence and energy dispersive X-ray diffraction of breast tissue, *Radn. Phys. Chem.* 71(2004) 969-970

Getty DJ, D'Orsi C, Pickett R, Newell M, Gundry K, Roberson S., Improved accuracy of lesion detection in breast cancer screening with stereoscopic digital mammography, *Radiological Society of North America (RSNA) Scientific Assembly and Annual Meeting Program* (2007) SSGO1-4

Getty DJ, D'Orsi CJ, Pickett RM, Stereoscopic Digital Mammography: Improved Accuracy of Lesion Detection in Breast Cancer Screening, *Digital Mammography, Lecture Notes in Computer Science* 5116(2008) 74-79

Griffiths JA, X-ray diffraction measurements for breast tissue analysis, Ph.D. Thesis, University College London, UK, 2005

Griffiths JA, Royle GJ, Robert D. Speller, Julie A. Horrocks, Alessandro Olivo, Silvia Pani, Renata Longo, Simon H. Spencer, Mark S. Robbins, Damian P. Clifford, Andrew M. Hanby, Diffraction Enhanced Breast Imaging: assessment of realistic system requirements to improve the diagnostic capabilities of mammography, *IEEE*, 2004

Griffiths JA, Royle GJ, Hanby AM, Horrocks JA, Bohndiek SE, Speller RD, Correlation of energy dispersive diffraction signatures and microCT of small breast tissue samples with pathological analysis, *Phys. Med. Biol.* 52 (2007) 6151-6164

Griffiths JA, Royle GJ, JA. Horrocks, Hanby AM, Pani S, Speller RD, Angular dispersive diffraction microCT of small breast tissue samples, *Radn. Phys. and Chem.* 77(2008) 373-380

Gunnell D, Okasha M, Davey Smith G, Oliver S, Sandhu J, Holly J, Height, leg length, and cancer risk: a systematic review, *Epidemiol. Rev.* 23(2001) 313– 42

Hackshaw AK, Paul EA Breast self-examination and death from breast cancer: a meta-analysis, *Brit. J. Cancer* 88(7) (2003) 1047 - 1053

Harding G, X-ray diffraction imaging – A multi-generational perspective, *Applied Radiation and Isotopes* 67(2009) 287-295

Harding G, Newton M, Kosanetzky J, Energy-dispersive X-ray diffraction tomography, *Phys. Med. Biol.* 35(1990) 33-41

Harding G, Schreiber B, Coherent X-ray scatter imaging and its applications in biomedical science and industry, *Radn. Phys. and Chem.* 56(1999) 229-245

Harris, EJ, Royle GJ, Speller RD, Griffiths JA, Kidane G, Hanby AM, Evaluation of a novel low light level (L3 vision) CCD technology for application to diffraction enhanced breast imaging, *Nuclear Imaging and Methods in Physics Research A* 513(2003) 27-31

Hasnah MO, Zhong Z, Oltulu O, et al, Diffraction enhanced imaging mechanisms in breast cancer specimens, *Med. Phys.* 29(2002) 2216–2221

Hendrick R.E., Breast MRI: Physics to Maximise Its Sensitivity and Specificity to Breast Cancer, *Medical Physics*, 31(2005) 1737-1737

Houssami N., L Irwig, C. Loy, Accuracy of combined breast imaging in young women, *The Breast*, 11(2002) 36-40

Hubbel JH, Overbo I, Relativistic atomic form factors and photon coherent scattering cross-sections, *J. Phys. Chem. Ref. Data* 8 (1979) 69

Hukins DL, X-ray diffraction by disordered and ordered systems, Butterworths, London (1983)

Huynh PT, Jarolimek AM, Daye S, The false-negative mammogram, *RadioGraphics* 18(1998) 1137-1154

ISD Statistical Publication Notice ISD Scotland Online, Accessed 2011

James VJ, Kearsley J., Irving, T., Amemiya Y. & Cookson D, Using hair to screen for breast cancer, *Nature* 398, 33–34 (1999)

James VJ, Reply to the letter of Rogers et al. entitled ‘Reproducibility of Cancer Diagnosis Using Hair’, *Int. J. Cancer* 118(2006) 1061–2

JCPDS – Joint Committee on Powder Diffraction Standards, a diffraction database (over 500,000 entries as of 2006) maintained by International Centre for Diffraction Data (ICDD)

Johns PC, Yaffe MJ, Coherent scatter in diagnostic radiology, *Med. Phys.* 10(1983)

Karellas A, Srinivasan Vedantham, Breast cancer imaging: A perspective for the next decade, *Med. Phys.* 35(2008), 4878-4897

Kelsey JL, A review of the epidemiology of human breast cancer, *Epidemiol Rev.* 1(1979) 74-109

Key TJ, Verkasalo PK, Banks E, Epidemiology of breast cancer (Review), *The Lancet Oncology* 2(2001) 133-140

Kidane G, Breast tissue characterization using low angle X-ray scattering, Ph.D. Thesis, University College London, UK, 2000

Kidane G, Speller RD, Royle GJ, Hanby AM, X-ray scatter signatures for normal and neoplastic breast tissues, *Phys. Med. Bio.* 44(1999) 1791-1802

Knoll GF, Radiation Detection and Measurement, 3rd edition, *Wiley and Sons* (2000)

Kolb TM, Lichy J, Newhouse JH, Comparison of the performance of screening mammography, physical examination, breast US and evaluation of factors that influence them: An analysis of 27,825 patient evaluations, *Radiology* 225(2002) 165-175

Lazarev P, Paukshto M Pelc N, Sakharova A, Human tissue X-ray diffraction: breast, brain and prostate, Proc. 22nd Annual *IEEE EMBS Conference* 4(2000) 3230-3233

Leborgne R, Diagnosis of tumors of the breast by simple roentgenography: calcifications in carcinomas, *Am. J. Roentgenol., Radium Ther. Nucl. Med.* 65(1)(1951) 1–11

Lewin JM, D’Orsi CJ, Hendrick RE, Moss LJ, Isaacs PK, Karellas A, Cutter GR, Clinical comparison of full-field digital mammography and screen-film mammography for detection of breast cancer, *Am. J. Roentgenol.* 179(2002) 671–677

Lewis RA, Rogers KD, Hall CJ, Towns-Andrews E, Slawson S, Evans A, Pinder SE, Ellis IO, Boggis CRM, Hufton AP, Dance DR, Breast cancer diagnosis using scattered X-rays, *J. Sync. Radn.* 7(2000) 348-352

Liberman M, Sampalis F, Mulder DS, Sampalis JS, Breast cancer diagnosis by scintimammography: a meta-analysis and review of the literature, *Breast Cancer Research and Treatment*, 80(2003) 115-126

Liu C, Yan X, Zhang X, Yang W, Shi D, Zhu P, Huang W, Peng W, Yuan Q, Evaluation of X-ray diffraction enhanced imaging in the diagnosis of breast cancer, *Phys. Med. Biol.* 52(2007) 419-427

Luggar RD, Horrocks JA, Speller RD, Lacey RJ, Determination of the geometric blurring of an energy dispersive X-ray diffraction (EDXRD) system and its use in the simulation of experimentally derived diffraction profiles, *Nuclear Instruments and Methods in Physics Research A* 383(1996) 610-618

Luggar RD, Horrocks JA, Speller RD, Lacey RJ, Low angle X-ray scatter for explosives Detection: a Geometry Optmization, *Appl. Radn. Isot.* 48(1997) 215-224

Malich A, Bohm T, Facius M, Kleinteich I, Fleck M, Sauner D, Anderson R, Kaiser WA, Elelctrical impedance scanning as a new imaging modality in breast cancer detection.- a short review of clinical value on breast application, limitations and perspectives, *Nuclear Instruments and Menthods in Physics Research A*, 497(2003) 75-81

Marten, H, Naes, T, Multivariate Calibration, *John Wiley*, New York (1991)

Merck Manual of Diagnosis and Therapy – Breast Disorders: Cancer, *Merck & Co., Inc.* (2003)

Northern Ireland Cancer Registry (NICR) Cancer Survival Online Statistics,
Accessed 2011

ONS - 2005-2009 Office for National Statistics (ONS), *Statistical Bulletin: Cancer survival in England* (2011) (Patients diagnosed 2005-2009 and followed up to 2010)

Pani S, Jones L, Griffiths J, Royle G, Horrocks J, Speller R, Breast tissue characterisation using energy-dispersive X-ray diffraction computed tomography, *Proc. European Conference on X-ray Spectrometry* (2006)

Pisano ED, Gatsonis C, Hendrick E, Yaffe M, Baum JK, Acharyya S, Conant EF, Fajardo LL, Bassett L, D'Orsi C, Jong R, Rebner M, Diagnostic performance of digital versus film mammography for breast-cancer screening, *N. Engl. J. Med.* 353(2005) 1773–1783

Pisano ED, Hendrick RE, Yaffe MJ, Baum JK, Acharyya S, Cormack JB, Hanna LA, Conant EF, Fajardo LL, Bassett LW, D'Orsi CJ, Jong RA, Rebner M, Tosteson AN, Gatsonis CA, Diagnostic accuracy of digital versus film mammography: Exploratory analysis of selected population subgroups in DMIST, *Radiology* 246(2008) 376–383

Poletti ME, Gonçalves OD, Mazzaro I, X-ray scattering from human breast tissues and breast-equivalent materials, *Phys. Med. Biol.* 47(2002) 47-63

Poulos A, McLean D, Rickard M and Heard R, Breast compression in mammography: How much is enough?, *Journal of Medical Imaging and Radiation Oncology* (formerly *Australasian Radiology*) 47(2003) 121–126

Polymer Science Learning Center (PSLC), USA, 2005

Pramanik M, Ku G, Li C, Wang LV, Design and evaluation of a novel breast cancer detection system combining both thermoacoustic (TA) and photoacoustic (PA) tomography, *Med. Phys.* 35(2008) 2218-2223

Reis LO, Dias FG, Castro MA, Ferreira U, Male breast cancer, *The Aging Male*, 14 (2011), 99-109

Rogers KD, Hall CJ, Hufton A, Wess TJ, Pinder SE, Siu K, Reproducibility of cancer diagnosis using hair, *Int. J. Cancer* 118(2006) 1060

Roncker CM, Erdmann CA, Land CE, Radiation and breast cancer: a review of current evidence, *Breast Cancer Res.* 7(2005) 21-32

Round AR, Wilkinson SJ, Hall CJ, Rogers KD, Glatter O, Wess T, Ellis IO, A preliminary study of breast cancer diagnosis using laboratory based small angle X-ray scattering, *Phys. Med. Biol.* 50(2005) 4159-4168

Royle GJ, Speller RD, Quantitative X-ray diffraction analysis of bone and marrow volumes in excised femoral head samples, *Phys. Med. Biol.* 40(1995) 1487-1498

Shapiro S, Strax P, Venet L, Periodic breast cancer screening in reducing mortality from breast cancer, JAMA, *J. Am. Med. Assoc.* 215(1971), 1777–1785

Sidhua S, Siu KK, Falzon G, Nazaretian S, Hart SA, Fox JG, Susil BJ, Lewis RA, X-ray scattering for classifying tissue types associated with breast disease, *Med. Phys.* 35(2008) 4660-4670

Smith FA, A primer in applied radiation physics, *World Scientific Publishing* (2000)

Smith-Warner SA, Spiegelman D, Yaun S-S, van den Brandt PA, Folsom AR, Goldbohm RA, Graham S, Holmberg L, Howe GR, Marshall JR, Miller AB, Potter JD, Speizer FE, Willett WC, Wolk A, Hunter DJ, Alcohol and Breast Cancer in Women: A Pooled Analysis of Cohort Studies, *JAMA* 279(1998) 535-540

Skaane P, Hofvind S, Skjennald A, Randomized trial of screen-film versus full-field digital mammography with soft-copy reading in population-based screening program: Follow-up and final results of Oslo, II study, *Radiology* 244(2007) 708–717

Speller R, Tissue Analysis Using X-ray Scattering, *X-ray Spectrum* 28(1999) 244-250

Spratt JS, Heuser L, Polk HC Jr., Growth rates of primary breast cancers, *Cancer* 43(1979) 1888-1894

Sutton M, Laaziri K, Koulkes WD, Response to ‘The traps and pitfalls inherent in the correlation of changes in the fibre diffraction pattern of hair with breast cancer’, *Phys. Med. Biol.* 48(2003) L11–L13

Tabar L, Vitak B, Chen HH, Yen MF, Duffy SW, Smith RA, Beyond randomized controlled trials: organized mammographic screening substantially reduces breast carcinoma mortality, *Cancer* 91(2001) 1724–1731

Theodorakou C and Farquharson MJ, Human soft tissue analysis using X-ray or gamma ray techniques, *Phys. Med, Biol.* 53(2008) R111-R149

Thomas DB, Whitehead J, Dorse C, Threatt BA, Gilbert Jr. FI, Present AJ and Carlile T, Mammographic Calcifications and Risk of Subsequent Breast Cancer, *J. Natl. Cancer Inst. (JNCI)* 85 (3) (1993), 230-235

Unscrambler v9.5 (2010), Camo inc., Norway, Multivariate analysis software

Varghese SS, Wilson DB, Penberthy LT, Smith WR, Examining the evidence for breast self-examination recommendations, *Clinical Governance: An International Journal* 11(2006) 225 – 233

Veronesi U, Paganelli G, Galimberti V, Luini A, Zurrada S, Robertson C, Sacchini V, Veronesi P, Orvieto E, De Cicco C, Intra M, Tosi G, Scarpa D, Sentinel-node biopsy to avoid axillary dissection in breast cancer with clinically negative lymphnodes, *Lancet* 349(1997) 1864-7

Warner E, Messersmith H, Causer P, Eisen A, Shumak R, Plewes D, Systematic Review: Using Magnetic Resonance Imaging to Screen Women at High Risk for Breast Cancer, *Annals of Internal Medicine* 148(2008) 671-679

Welsh Cancer Intelligence and Surveillance Unit (WCISU) Cancer Survival Trends in Wales 1985-2004 (2010) (Cases followed up to 31st December 2008)

WHO – Breast Cancer Mortality and Screening, *World Health Statistics* (2008) 21

XCOM – Photon Cross Sections Database, Berger MJ, Hubbell JH, Seltzer SM, Chang J, Coursey JS, Sukumar R, Zucker DS, Plot generated by Jarek Tuszyński, Virginia

XCOMP – Tungsten anode x-ray spectrum generating software, Nowotny R, Institut für Biomediz. Technik und Physik, University of Vienna